DIRECTION-DEPENDENT CONSTRICTION FLOW IN A POROELASTIC SOLID: A MODEL OF THE INTERVERTEBRAL DISC VALVE

by

DANA C. AYOTTE

B.Sc. Mechanical Engineering
Queen's University, Kingston, Canada (1993)

Submitted to the Department of Mechanical Engineering
in Partial Fulfillment of the Requirements for the Degree of

MASTER OF SCIENCE IN MECHANICAL ENGINEERING
at the
MASSACHUSETTS INSTITUTE OF TECHNOLOGY
December 1996
[February 1997]

Signature of Author_____
M.I.T. Department of Mechanical Engineering
December 10, 1996

Certified by_____
Dr. Slobodan Tepic
Lecturer, Department of Mechanical Engineering
Thesis Supervisor

Accepted by_____

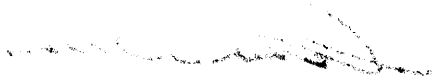

DIRECTION-DEPENDENT CONSTRICTION FLOW IN A POROELASTIC SOLID: A MODEL OF THE INTERVERTEBRAL DISC VALVE

by

DANA C. AYOTTE

Submitted to the M.I.T. Department of Mechanical Engineering
on January 17, 1996 in Partial Fulfillment of the Requirements for the
Degree of Masters of Science with Specification in Mechanical Engineering

ABSTRACT

Spinal disorders are a common medical problem, frequently involving degeneration or disruption of the intervertebral discs. A better understanding of the mechanical function of the normal, healthy disc is necessary to diagnose and effectively treat disc pathologies.

A comparison of the *in vivo* intradiscal pressure reached during daily loading and the reverse osmotic pressure during rest indicates the necessary existence of a valve mechanism to avoid disc dehydration or collapse under load. It is hypothesized that a mechanical valve is provided by the interaction of flow through the cartilage endplates and the marrow contact holes in the underlying bony endplates. As fluid flows out through these small holes, the resulting drag forces on the cartilage matrix compress it locally at the holes, thereby creating a high resistance. As fluid flows back in, the matrix expands and the resistance is lower. The resistance to fluid flow is, therefore, direction-dependent.

A morphological study using scanning electron microscopy of sheep and human bony endplates was carried out to investigate the structures which could provide the valve in the disc. A physical model of flow through a poroelastic solid and one underlying constriction hole was constructed. It clearly demonstrated the hypothesized direction-dependent resistance effect. A finite element (FE) model of the physical model was constructed and validated against the experimental data. The FE model was used to demonstrate the effects of an increase or decrease in the size and number of underlying constriction holes on the imbibition and exudation resistance, as well as the ratio of the two.

Thesis Supervisor: Slobodan Tepic, Sc.D.
Title: Lecturer, Massachusetts Institute of Technology, Department of Mechanical Engineering, and
Senior Research Scientist and Head of Biomechanical Engineering, AO Research Institute, Davos, Switzerland

BIOGRAPHICAL NOTE

The candidate holds a Bachelor of Science degree with first class honors in Mechanical Engineering from Queen's University, Kingston, Canada. After completion of this degree in April of 1993, the candidate worked at the AO Research Institute in Davos Switzerland for one year from June 1993 to June 1994. This job was an exchange placement through the International Association of Exchange Students for Technical Experience (IAESTE). The AO Institute is an orthopaedic research institute, specializing in all areas of research concerned with bone fracture fixation, from more basic research to applied hardware design and development. Under the supervision of Dr. S. Tepic at the AO Institute, Head Research Scientist in the AO Engineering Department and Lecturer at M.I.T., the candidate began graduate studies at M.I.T. in September of 1994. From September 1994 until May 1995 the candidate completed course work toward the S.M. degree and in June of 1995 returned to the AO Institute to complete the research toward this degree.

During the completion of the B.Sc. degree the candidate held summer research placements at both the University of Toronto department of Medical Biophysics, as well as at Queen's University department of Mechanical Engineering and Clinical Mechanics Group (associated with the Kingston General Hospital). The S.M. project work was presented at the 10th annual European Society of Biomechanics conference in Leuven, Belgium in August 1996.

ACKNOWLEDGMENTS

First and foremost I would like to thank my supervisor, Dr. Slobodan Tepic, for his seemingly endless number of incredible ideas and his eternal optimism, and for providing me with the inspiration not only to finish this project, but to continue to pursue a career in engineering research. I also owe many thanks to Dr. Keita Ito for putting up with my many questions, for his time spent in discussion, and also for his enthusiasm for this project which kept me going in times of doubt. I owe special thanks to Nick Bishop for sharing with me his vast knowledge of applied engineering through truly endless hours spent discussing many aspects of this project, as well as the time spent in reviewing and criticizing my thesis.

I would also like to thank Dr. Steve Bresina for his help at the AO Institute as well as for allowing me to use his office, without which I probably never would have finished writing this thesis. I would like to thank Steve Ferguson for helping me struggle through non-linear finite element modeling, and a special thanks to Geoff Richards for his help on the scanning electron microscope, but mostly for providing comic relief throughout my entire stay at the AO Institute.

To the following people, many thanks for providing me with the friendly assistance I needed at the AO Institute: Dr. Max Kaeaeb, Gethin Owen, Martin Stoddart, Claudia Guntensberger, Emir Schluepp, Deiter Wahl, Benni Dicht, Elena Rampoldi, Iris Keller, Patrick Michel, Elspbeth Wenzinger, Helga Klebl and the Tierstahl staff.

I also owe many thanks to the Newman Lab for providing me with office space while at M.I.T., and for taking me in as a member of their lab. I would also like to express my utmost appreciation to Annette Vissing-Joergensen, and all members of the M.I.T. women's hockey team and the M.I.T. women's rugby team (a special thanks to the Enforcer) for helping me keep my sanity while studying at M.I.T.

CONTENTS

CHAPTER
ONE

INTRODUCTION

1.1 BACKGROUND

1.1.1 STRUCTURAL ANATOMY OF THE SPINAL MOTION SEGMENT

The term "spinal motion segment" (SMS) refers to the repeated unit of the spine made up of the intervertebral disc contained on the cranial and caudal ends by the vertebral bodies. The vertebral bodies are united across the disc by the posterior and anterior longitudinal ligaments as shown in Figure 1.1.1. The disc can be separated into three parts; the nucleus pulposus, annulus fibrosus and the cartilage endplates. The cartilage endplates, which lie on the surface of the vertebrae underneath the nucleus and annulus, are composed of hyaline cartilage. This cartilage consists of a hydrated proteoglycan gel reinforced by collagen fibrils, and is similar to that of articular cartilage. However, one major difference between the cartilage of the disc and that of the joints is that the endplate cartilage is not directly connected to the subchondral bone of the vertebrae. Instead, the inner lamellae of the annulus merge directly into the cartilage endplates, and the outer lamellae are themselves directly connected to the bone through their collagen fibers. These structures are shown in Figure 1.1.2.

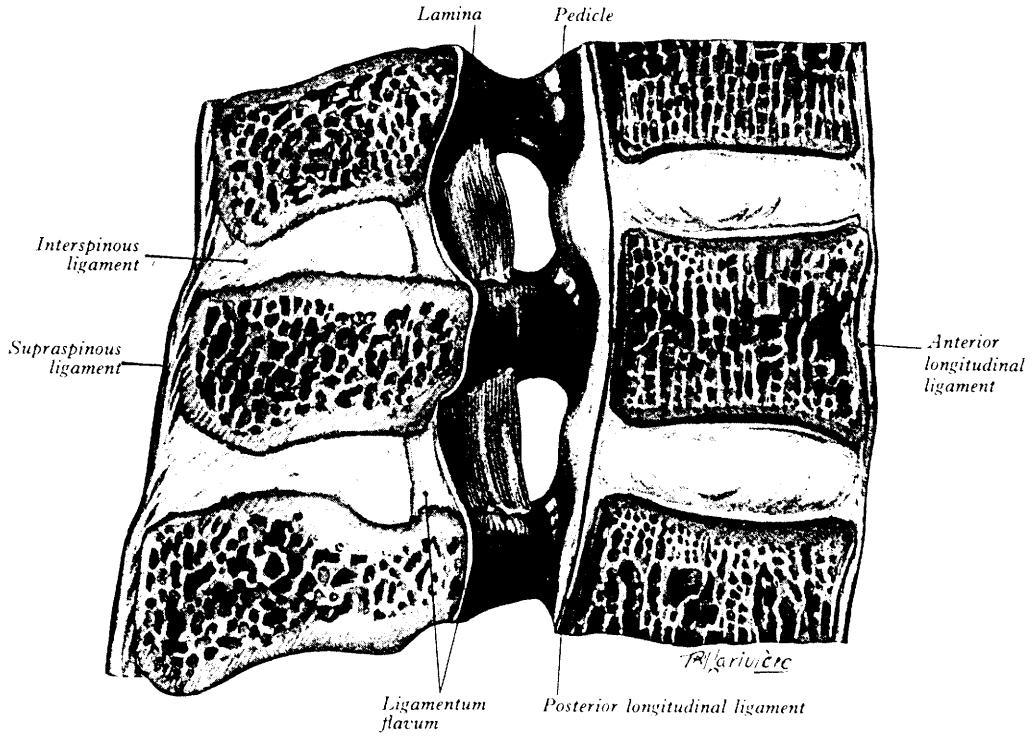

Figure 1.1.1 The vertebral bodies are united across the disc by the posterior and anterior longitudinal ligaments (from Gray's Anatomy [8]).

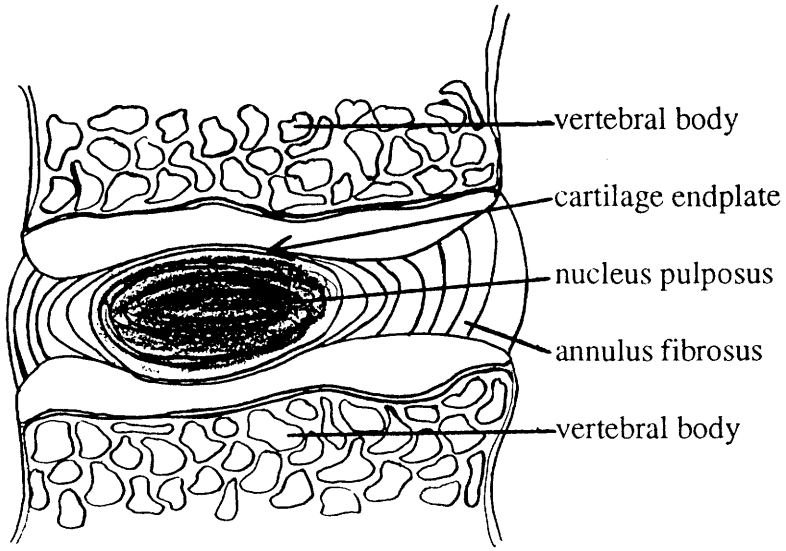

Figure 1.1.2 The endplate cartilage is not directly connected to the subchondral bone of the vertebrae. Instead, the inner lamellae of the annulus merge directly into the cartilage endplates, and the outer lamellae are themselves directly connected to the bone through their collagen fibers.

The proteoglycan gel of cartilage consists of macromolecules of proteoglycan and bound water. These macromolecules are made up of glycosaminoglycan chains (GAG) attached to a central protein core. The GAG chains consist of polymers of chondroitin sulfate and keratin sulfate which themselves contain bound acidic groups OSO_3^- and COO^-. This results in the high fixed charge density of the cartilage matrix and its consequent ability to attract and bind water [17]. The proteoglycan molecules are randomly entwined with the collagen fibrils and together these chains are dispersed in water as shown schematically in Figure 1.1.3.

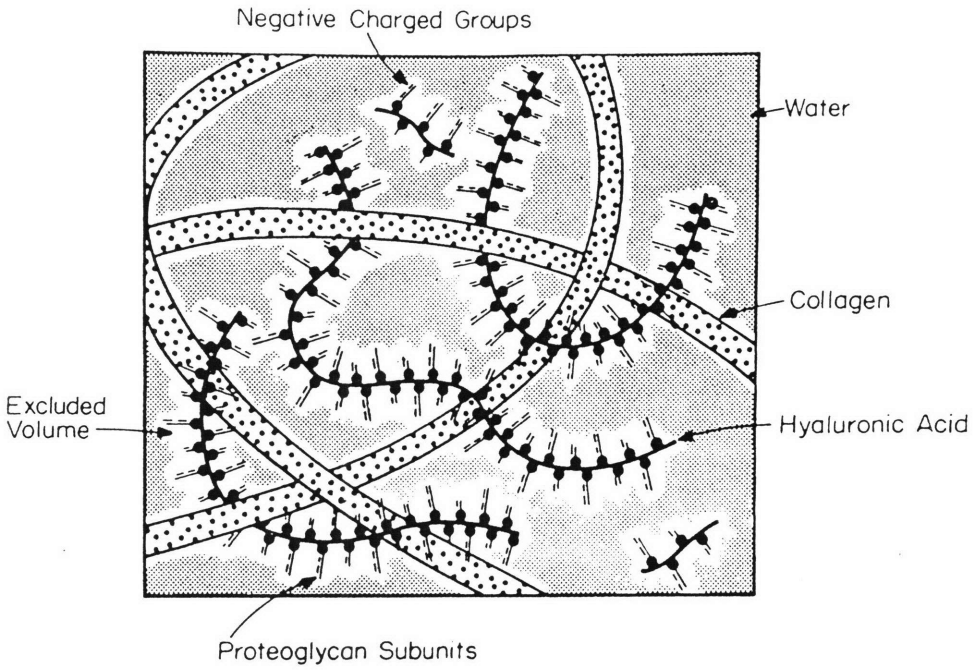

Figure 1.1.3 The proteoglycan molecules in cartilage are randomly entwined with the collagen fibrils and together these chains are dispersed in water (from Lai and Mow [14]).

The gel-like material of the nucleus pulposus forms the center of the disc, and is made up of proteoglycans, some collagen, and up to 80% water in the young disc. These constituents are the same as those in the cartilage, but in different proportions; the nucleus is composed mainly of proteoglycans and water while the cartilage is predominantly collagenous. Thus, the fixed charge density of the nucleus is much higher than that of the cartilage and it is the nucleus which causes most of the osmotic "swelling pressure" [36] in the disc. The nucleus is contained by the surrounding annulus fibrosus, which is composed of approximately twelve concentric lamellae, which are themselves made up of collagen fibers.

Directly beneath the disc is a layer of cortical bone often referred to as the bony endplate. This endplate forms part of a cortical shell encasing the trabecular bone which makes up the main body of the vertebrae, as shown in Figure 1.1.1.

1.1.2 FUNCTION OF THE SPINAL MOTION SEGMENT

The gel-like material of the nucleus pulposus is contained by the layers of fibrocartilage of the annulus. In the healthy disc the nucleus pulposus acts as a fluid-filled sac, therefore any load applied to the SMS is distributed throughout the nucleus as a hydrostatic pressure [19,20,22] which is radially balanced by hoop tension in the annulus. In this way the applied load is supported mainly by fluid stresses and in part by stresses in the solid structures of the disc [19]. The fluid stresses are partly countered by the osmotic pressure of the proteoglycans [36]. However, the fluid stresses are significantly higher [22] resulting in a pressure gradient which forces the fluid out of the disc, causing a volume decrease and consequent overall height loss in the spine. No clear quantitative evidence exists for the dominant path of fluid flow, however, there are indications that this path is through the cartilage endplates [5]. During rest, the nucleus swells due to fluid imbibition caused by the osmotic driving force of the negatively charged GAG chains of the proteoglycans.

The collagen network in the cartilage is tightly woven due to the considerable cross-linking of the collagen, and indeed it must be so in order to control swelling and prevent PG loss, particularly in the articulating joints. However, the packing of collagen in the nucleus of the disc need not be so tight since the disc always sustains some compressive load due to muscle forces, even during rest [17]. Thus, it is the swelling of the nucleus and loss of fluid from the nucleus itself which are mainly responsible for the diurnal changes in height, as opposed to the swelling of and loss of fluid from the cartilage. The fluid flows into and out of the nucleus, through the cartilage endplates.

1.1.3 MOTIVATION

Pressure in the nucleus of the intervertebral disc has been measured *in vivo* under varying postures and loads. According to data collected by Nachemson [22], an average daily intradiscal pressure, taken as an average of pressure measurements for sitting, standing and walking, is approximately 9 bar, while for other postures with and without load lifting by the subject the pressure reached values as high as 30 bar. These daily intradiscal pressures cause fluid to be lost from the disc. Adams and Hutton [1] found an overall fluid loss in cadaveric

lumbar motion segments of 11% after four hours of creep loading under cadaver body weight. As fluid is lost from the disc the osmotic pressure of the disc tissue increases due to an increase in concentration of the hydrophilic proteoglycans (PG). This increasing PG concentration limits, to some extent, the fluid loss from the disc, however, fluid pressure equilibrium is probably never reached in the course of a day [35,36].

During rest the fluid is drawn back into the disc under the osmotic driving force and the amount of swelling is limited by annular tension and the compressive forces of the relaxed muscles and ligaments. As fluid is gained in the disc, the PG concentration decreases consequently decreasing the driving force for fluid flow. The daily duration of spinal loading can be taken as approximately 16 hours and that of rest approximately 8 hours, and the daily average pressure driving fluid out of the disc is significantly higher than the average osmotic force drawing it back in. Thus, some direction-dependent mechanism must exist to ensure that all the fluid exuded during loading is imbibed during rest. That is, there must be a valve phenomenon in the disc providing higher resistance to exudation flow than to imbibition flow.

1.2 PREVIOUS RESEARCH

1.2.1 BIOMECHANICS OF THE SPINAL MOTION SEGMENT

• Creep Tests

The rate of creep under axial compressive loads of human spinal motion segments has been observed in *in vitro* experiments to be slower than the rate of their subsequent relaxation (i.e. free extension of the segment after the application of the compressive creep load). Markholf and Morris [15] found that the original height of the segments was recovered during relaxation in a shorter time period than that of the prior creep load duration. The higher rate of extension indicates that recovery of the disc *in vivo* after a period of loading occurs more quickly than deformation under compressive loads. Their experiment implies that flow imbibition, which contributes to swelling of the disc during recovery, sees less resistance than exudation during loading, although from this experiment the flow effects could not be separated from any structural effects, i.e. elastic resilience of the annular tissue. However, direction dependent resistance in the disc seems to be necessary in order to bring the disc back to its full water content during rest if fluid is lost continuously over the course of the day.

In the same study, creep experiments were performed on the SMS with: i) an applied annular defect, ii) discectomy (removal of the nucleus), and iii) complete removal of the nucleus and supporting bone (i.e. only a ring consisting of the annulus and underlying bone remained). In all cases the first creep loading cycle after tissue removal showed severely decreased stiffness but a similar creep response compared with the intact disc. By the third loading cycle the creep response, in all cases, approached that of the intact disc. In the case of the annular defect, this result was explained by the "self-sealing" behavior of the nuclear material, which tended to fill the defect during the first loading cycle and return the disc to a near-normal mechanical state. In the cases of the discectomy and total removal of the nucleus and supporting bone, they conclude from these results that the annulus is the primary load bearing structure of the disc.

A similar conclusion was made by Koeller *et al.* [12] who performed compressive creep tests on human lumbar discs for 6 hours duration. They found that creep and recovery were also possible in the SMS with "desiccated" discs (i.e. completely dehydrated), that is, without loss or absorption of fluid, and therefore concluded that it is the annulus which is responsible for

creep in the intervertebral disc. In particular, they claim that disc recovery is due to the energy stored in the annular fibers during loading.

These conclusions are in direct contrast with several studies which have investigated the intradiscal pressure and fluid flow during loading. For example, Nachemson [21] found that the pressure in the disc varied approximately linearly with applied load, and proposed that the high hydrostatic pressures measured in healthy discs indicate that it is the fluid which supports the load, thus relieving the annulus fibrosus of vertical stresses (however, such pressures would necessitate tensile reaction loading on the annular fibers, and thus, the creep behavior of the disc would be determined in part by the tensile properties of the annulus). Andersson and Schultz [2] studied the effects of fluid injection into the nucleus on the response of human cadaveric lumbar SMS to various loading conditions and found that the state of hydration of the nucleus greatly affects the mechanical behavior. They showed substantial differences in the load response and intradiscal pressure between discs which, prior to testing, retained injected fluid and those which did not, indicating that the hydration of the SMS is an important determinant of its mechanical behavior.

McNally and Adams [19] measured the stress distribution in cadaveric discs during various loading configurations. They measured both the vertical and horizontal components of stress across the entire disc and found that in healthy discs the nucleus behaves as a fluid exhibiting a constant hydrostatic pressure under compressive loading. The compressive stress was found to drop off dramatically through the outer annulus indicating that this tissue sustains predominantly tensile stresses. A critical observation made with respect to the distribution of the reaction load between the fluid and solid structures was that after the application of an equivalent diurnal creep load (3 hours at 1200 N) the vertical compressive stresses in the posterior annulus were found to increase, while the hydrostatic pressure in the nucleus often decreased considerably. This observation would indicate that the fluid in the disc initially supports most of the applied load but as the disc loses fluid the load is gradually transferred to the solid structures in the disc. This eventually results in a significant amount of stress-shielding by the posterior annulus and the apophyseal joints. In this way, the fluid flow behavior controls the creep response of the motion segment.

Long term creep testing of cadaveric motion segments have shown that even after several hours of loading the spine segment continues to deform [1]. While some of this deformation is due to the viscoelastic behavior of the solid phase of the disc, it is estimated that approximately two thirds to three quarters of the overall deformation is due to fluid loss [1].

It has also been suggested that the viscoelastic effect due to deformation of the collagen fibers in the disc is responsible for the initial short-term deformation of the motion segments, while it is the fluid loss from the disc which accounts for the long-term deformation [3]. Urban states that it is the rearrangement the collagen network and the bulk movement of disc matrix which accounts for the initial deformation, and that a "substantial fraction" of long term creep is due to fluid flow [36].

- **Flow Behavior**

Cassidy *et al.* [5] performed uniaxial compressive tests on canine intervertebral discs. They measured the water content of the discs before and after 30 minute creep loading periods by comparing the weight of disc tissue samples before and after freeze drying. They found, at 20% overall strain, a 12% loss of fluid from the nucleus. One noteworthy observation was that after creep loading, no condensed water was seen on the outside of the annulus, however, fluid was found on the surfaces of the loading platens, which had most likely been exuded from the cut ends of the vertebrae. This suggests that the main path for fluid flow out of the disc is through the cartilage endplates into the underlying bone, as opposed to through the annulus which has been previously suggested. They also proposed that the viscoelastic behavior of the disc under compressive loading is due to the transport of water out of the disc. This hypothesis is supported by their experimental data for volumetric changes in the disc during stress relaxation and the good correlation with direct measurements of disc water content during compression.

In a further study Cassidy *et al.* [6] developed a mathematical water transport model for the intervertebral disc creep response assuming flow through the endplates only. Three models were studied; constant hydrostatic pressure, strain-dependent hydrostatic pressure which considers a linear increase in osmotic pressure with decreasing hydration, and strain- and time-dependent hydrostatic pressure which takes account of the time-dependent "retractile" forces exerted by the collagen fibers of the annulus lamellae. The results were validated against experimental results from canine SMS creep tests, and it was found that the strain-dependent osmotic pressure model adequately described the experimental creep response. This result demonstrates the important mechanical role of the change in osmotic pressure with disc water content.

In the studies of Cassidy *et al.* fluid flow back into the disc during recovery was not modeled. This is the case in several investigations which focus only on the fluid flow behavior out of the disc under compressive loading [1,2,12,15,21]. However, a comparison of the flow in

and out of the disc is critical in fully understanding the behavior of the spinal motion segment during daily loading.

- **Age- and Disease-Related Changes**

A study by Koeller *et al.* [13] investigated the changes in "creep" behavior with age. Human SMS were dynamically loaded for 5 minutes (950 ± 540 N at 1 Hz to simulate walking), resulting in a decrease in both the total deformation and the "viscoelastic state" (decreased time constant) for specimen ages from the middle of the third decade to the beginning of the sixth, at which point the viscoelastic state began to increase again. An interesting correlation was found between this age period (third to sixth decade), during which the disc is considered to behave most efficiently, and the incidence of back pain. Through an attempt to correlate the decreased viscoelastic state with water content it was found that these factors often actually run inversely, that is, a high water content is found in discs with decreased viscoelastic behavior. These findings offer interesting insight into the hypothesis of valve pathology (see Section 1.3.1). The decrease in viscoelasticity coupled with an increased water content of the disc could be explained by blockage of the holes in the bony endplate due to calcification of the cartilage endplate or remodeling of the vertebral bone at an age when the discs are still well hydrated. The further increase in viscoelasticity after the fifth decade could be due to changes in the mechanical behavior caused by dehydration of the disc and/or loss of proteoglycans.

Smeathers and Joanes [26] also found that older more degenerated discs had greater hysteresis in their force-displacement behavior. This could be explained by the loss of proteoglycan in older discs observed by Urban and Bergel [29] which would increase the rate of fluid loss during loading and decrease the rate of fluid uptake during swelling. In a study by Kazarian [10] human SMS with degenerated discs were found to creep faster, reach equilibrium sooner and often experience greater deflection than healthy discs after 1.5 to 2 hours of creep loading. These characteristics could be explained by a complete lack of fluid flow due to dehydration. Furthermore, total recovery of the disc after creep was never observed in any SMS, degenerated or healthy. This may be due to the fact that the specimens were kept in a humidity chamber but were not immersed in saline, thus, the volume of fluid lost during creep possibly could not be recovered during swelling. This observation gives further evidence for the pivotal role of fluid flow in the diurnal creep behavior of the disc. If it were the annulus alone which controls creep, and particularly recovery, these discs should have experienced near-full recovery even in the absence of fluid flow.

An interesting finding by Keller *et al.* [11] shows a relationship between bone mineral content (BMC) of the vertebral bodies and the creep behavior of the disc. They found that the viscous response of the disc increased (the motion segment became more viscous) with bone mineral content. If this increase in BMC is indicative of an increase in density of the bone due to calcification of the cartilage endplates or remodeling of the bony endplate, this finding offers further evidence for the presence of the hypothesized valves in the disc. As the holes in the bony endplates closed the resistance to flow out of the disc would rise, causing more viscous behavior of the disc under creep loading. At the very least this study suggests an interdependency between intervertebral disc mechanics and vertebral body properties.

1.2.2 SWELLING PRESSURE AND THE DIURNAL FLUID FLOW CYCLE

Several studies have focused on the swelling pressure behavior of the intervertebral disc. Urban *et al.* [33] define the net swelling pressure ($\mathbf{P_a}$) as the applied external pressure required to balance the difference between the osmotic pressure of the proteoglycans (π) and the tensile forces exerted by the collagen network ($\mathbf{P_c}$). That is, $P_a = \pi - P_c$. During rest, fluid is imbibed under the swelling pressure driving force until $\pi = P_c$ and $P_a = 0$. In the healthy human intervertebral disc the resting osmotic pressure (i.e. osmotic pressure of fully hydrated discs) has been found to be in the range of 0.3 to 3.5 bar depending on the fixed charge density of the disc tissue[34].

The swelling pressure changes with hydration due to changes in the proteoglycan concentration in the disc [34]. If, at a given disc hydration, a load is applied to the disc which is higher than the corresponding swelling pressure at that hydration, fluid is exuded from the disc. This loss of fluid increases the PG concentration and therefore the osmotic pressure, π, and relieves the tension in the collagen fibers, thus reducing $\mathbf{P_c}$ to zero. With increasing π the swelling pressure increases and in this way the fluid loss from the disc during loading is limited. The flow would eventually stop when the applied pressure balanced the swelling pressure, however, Urban and McMullin [36] suggest that osmotic equilibrium may never be reached during the course of the day. If this is the case, fluid is lost continuously over the entire course of daily loading. Therefore, an additional mechanism is necessary in order to allow the same volume of fluid lost during loading to be imbibed into the disc during rest under a relatively weaker driving force (osmosis alone) and over a relatively shorter period of time. Certainly the effect of the osmotic driving force is not enough, since not only is it a weaker driving force than the hydrostatic pressure during

loading, but it decreases during imbibition as fluid is gained and GAG concentration decreases.

For example, Adams and Hutton [1] measured the overall fluid loss in the disc during four hours of creep loading at body weight and found it to be 11% (final hydration 3.0 - 3.5 g H_20 / g dry wt.). According to data collected by Urban *et al.* [36] this loss corresponds to a swelling pressure of only 1 - 3 bar depending on the location in the spine. McNally and Adams [19] found that healthy (non-degenerated) discs under a 500 N load reached intradiscal pressures of 5 - 6 bar, while Nachemson [22] found daily *in vivo* intradiscal pressures reached an average of approximately 9 bar. Thus, it is highly unlikely that osmotic pressure alone could balance such normal daily intradiscal pressures, but it is clear that osmosis, to some extent, limits fluid losses during loading.

Urban and Maroudas [28] have measured the change in hydraulic permeability of the annulus and the nucleus with fluid content. It was observed that this permeability changes with the fluid content of the tissue such that it increases with increasing fluid content and decreases as fluid is lost from the disc as shown in Figure 1.2.1. They offer this phenomenon as an explanation for a faster rate of disc swelling during rest than that of exudation under load which would allow all the fluid lost during approximately sixteen hours of loading to be recovered in eight hours of rest. However, this non-linear relationship between hydraulic permeability and water content would not result in any *overall directional effects* in permeability. During both exudation and imbibition the same curve describes the permeability at any given hydration. In fact, the only directional effect there may be is that due to the relatively shorter period of swelling which acts to oppose the necessary valve effect: since the permeability at the outset of swelling is lowest, less fluid would be gained during swelling than that which was lost in the same time period during loading.

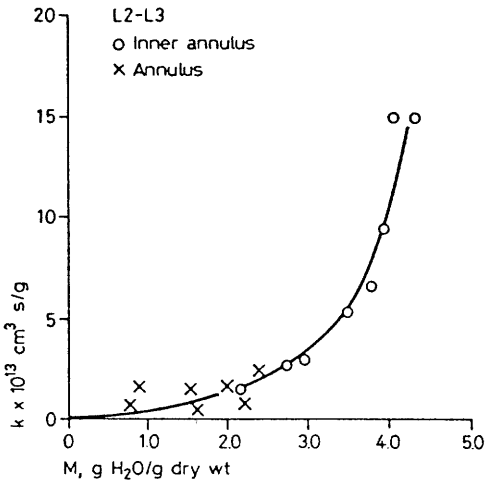

Figure 1.2.1 The change in hydraulic permeability of the annulus and the nucleus with tissue fluid content as measured by Maroudas and Urban [18]. The permeability was found to increase with increasing fluid content and decrease as fluid is lost from the disc.

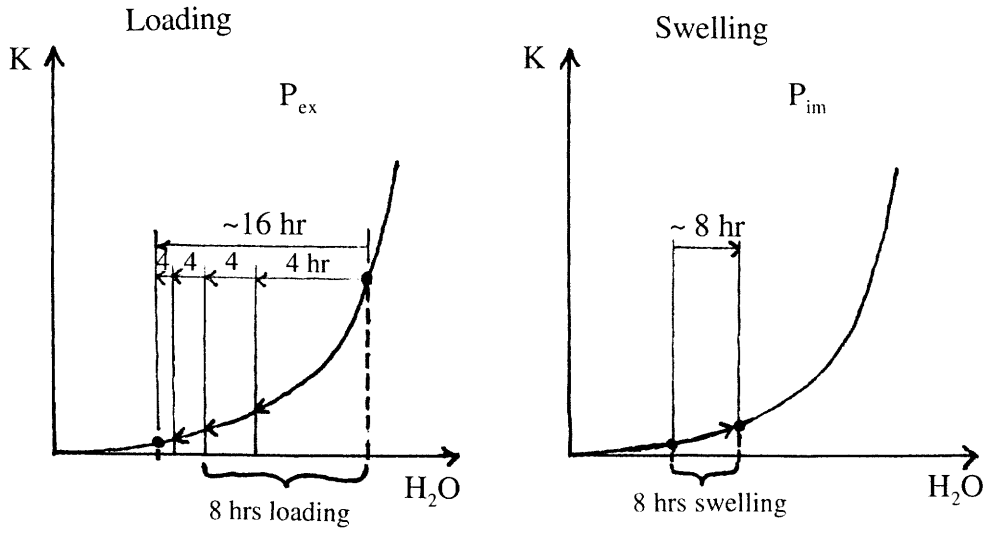

Figure 1.2.2 During both exudation and imbibition the same curve describes the permeability at any given hydration. In fact, the only directional effect there may be is that due to the relatively shorter period of swelling which acts to oppose the necessary valve effect: since the permeability at the outset of swelling is lowest, less fluid would be gained during swelling than that which was lost in the same time period during loading.

Urban and McMullin experimentally determined a relationship between tissue hydration of individual disc slices and swelling pressure [33]. The data indicates that the swelling pressure in the disc could balance loads at least as high as 7 or 8 bar which are in the range of *in vivo* intradiscal pressures measured under some loading conditions [22]. However, these swelling pressures were reached at very low tissue hydration levels of approximately 1 - 2 g H_2O / g dry wt. which correspond to a loss of fluid in the disc of approximately 50 -70 % (given an original overall average hydration of discs of 3.5 - 4.0 g H_2O / g dry wt. [1]; Urban and Maroudas saw ~ 4.5 in a 27 yr. old disc [32]) which is much higher than the overall disc fluid loss measured by Adams and Hutton at an average of only 11% under 4 hours of compressive creep loading at body weight [1]. Fluid losses in disc tissue slices under the application of a compressive load would be limited by both the increase in osmotic pressure as well as the decrease in hydraulic permeability with decreasing fluid content. However, given that the fluid losses were abnormally high under the loads applied to the tissue slices, which were in the range of fluid stresses found in the disc during creep loading (maximum 7 to 8 bar [19]), it could be inferred that *some additional physical mechanism must exist in the intact disc which limits these losses.*

1.2.3 DISC NUTRITION - CONTRIBUTION OF BULK FLOW

The intervertebral disc is an avascular structure, therefore the exchange of nutrients must take place through bulk flow of interstitial fluid or diffusion of solutes from the blood supply surrounding the disc. Since this project centers on the exchange of fluid in the disc, and its control mechanisms, it is important to determine whether bulk flow contributes to nutrient exchange in the disc, and particularly whether disruption of the flow results in the disruption of the nutrient supply to the disc, possibly resulting in disc degeneration. Several investigations have focused on the nutrient supply and exchange pathways of the intervertebral disc, and some have attempted to answer the question as to whether or not bulk flow plays an important role in disc nutrition or if the disc is sufficiently supplied by diffusion alone.

Brodin [4] showed through the injection of a fluorescent stain into rabbit ear veins that the blood supply to the disc surrounds the annulus and reaches the cartilaginous end plates. This would certainly indicate that some nutrient exchange, by whatever method, must take place through the end plates. A study by Nachemson *et al.* [23] showed that both the annulus fibrosus and the cartilage end plate to be permeable to diffusion, but could not make any conclusion about a dominant route. It was also discovered that all impermeable specimens of

cartilage end plate were lacking the "contacts" between the marrow of the trabeculae and the cartilage end plate which had been histologically observed in permeable specimens. These contacts or holes (see Chapter 2 Morphology) may provide a route for diffusion and, as we hypothesize, for bulk flow which may enhance diffusion.

Urban *et al.* [30] studied the diffusion of both the sulfate ion (a negatively charged ion) and methyl glucose (an uncharged solute), in the canine intervertebral disc. They found that diffusion appeared to be the main mechanism by which these small solutes are transported into the disc, since theoretical calculations neglecting bulk flow matched well with experimental data. In another study Urban *et al.* [27] found that for small anions such as sulfate, the amount of diffusion through the annulus was twice that through the endplate, since its negative charge results in its exclusion from the negatively charged nucleus, and therefore allows little diffusion through the endplate. They concluded that for small uncharged solutes such as glucose the endplate and annular route contribute equally, while for small cations the endplate route dominates. However, it was also found that the relative importance of the two routes depended on the amount of blood vessel contact observed between the marrow and cartilage end plate, which varies from person to person due to calcification of the endplate cartilage.

Holm *et al.* [9] studied the diffusion of oxygen, an uncharged solute, in the disc and concluded that the major route for nutrient supply is via the endplates, and that diffusion is the major mechanism supplying metabolites to the disc. Ogata and Whiteside [24] found that disruption of the end plate route caused a greater decrease in hydrogen washout than did the disruption of the annulus route, and thus also concluded that the main pathway for diffusion is through the cartilage endplate.

In another study Urban *et al.* [31] investigated the effect of exercise on nutrient transport in order to determine the contribution of bulk flow. They showed that in dogs, the transport of radioactively labeled sulfate was not enhanced in those animals which exercised compared with those which were anaesthetized. The dogs jogged continuously for one to six hours after injection of the labeled sulfate. Theoretical sulfate concentration curves calculated for diffusion transport alone matched well with the experimental data both in dogs which had been exercised and those which had not. Therefore they concluded that bulk flow had little effect on the total amount of solute transported into the disc. However, it is important to note that if the endplate is in fact the dominant route for bulk flow in the disc, and the sulfate ion is excluded from this route due to its negative charge, clearly any contribution of bulk flow to

nutrient transport will not be demonstrated in this experiment. The effects of exercise on the transport of *positively charged* or *uncharged* solutes would give a better indication of the contribution of bulk flow, as would subjecting the dogs to a more realistic daily loading cycle, i.e. to compare dogs which were anaesthetized with those which had undergone a normal daily cycle of constant loading.

It has been suggested that while diffusion alone contributes to the transfer of small solutes such as glucose, oxygen and sulfate, bulk flow may be necessary for the exchange of larger, less diffusible molecules such as hormones and enzymes [31]. Maroudas [16] found that for serum albumin, a large solute with a diffusion coefficient about ten times lower than that of glucose, there was an approximate two-fold increase in the rate of penetration into the disc with cyclic compression. Furthermore she found that there was also a two- to ten-fold increase in the equilibrium uptake of serum albumin with cyclic compressive loading and also with a constant static load.

It has also been suggested that diffusion is necessarily enhanced by bulk flow since the distances for diffusion in the disc are so large (in some cases 6 to 8 mm from the blood vessels). Holm *et al.* [9] found that as fluid is expressed from the disc, the total volume decreases, and consequently the distance for diffusion also decreases resulting in an increased rate of nutrient transport.

Many studies have shown that diffusion is the dominant means of transport of small solutes to the intervertebral disc, and this fact has been generally accepted. However, some studies have also demonstrated that bulk flow may indeed be critical in the transport of larger molecules. Further studies on the effects of fluid flow under diurnal creep loads on large solute transport are necessary. While the valve phenomenon in the disc is important for the mechanical behavior of the spine, it may also play a role in the nutrition of the disc. However, it seems that blockage of the endplate route, which could be explained by valve pathologies, severely decreases the nutrient supply to the disc whether through a combination of bulk flow and diffusion, or diffusion alone.

1.3 PROJECT OVERVIEW

1.3.1 HYPOTHESIS

The resistance to flow out of the intervertebral disc must be higher than the resistance to flow into the disc in order to limit the fluid loss and to ensure that all the fluid exuded during the course of the day is imbibed during rest. The physiologic valve provided by the change in hydraulic permeability with disc hydration as discussed in Section 1.2.2 does not provide any direction-dependent resistance in the disc.

The hyaline cartilage of the endplate can be modeled as a poroelastic or "biphasic" material in that it consists of a "porous" matrix of collagen and proteoglycan saturated with fluid [14]. This cartilage lies on the surface of the bony endplate of the vertebrae. Small holes or "marrow contacts" have been observed in the bony endplate providing channels from the cartilage to the trabecular bone of the vertebral bodies [24,30]. These channels appear to provide openings for the vascular buds which have been observed protruding up to the cartilage from the source vessels in the vertebral trabeculae and which provide nutrients for the disc [7,25]. Under the pressures sustained by the nucleus during daily loading it is hypothesized that these channels also provide a path for fluid flow. Under the driving force of the fluid pressure the fluid is forced out of the disc through the cartilage endplates and into the vertebral bodies (exudation), and these small holes act to constrict the flow. During swelling the fluid flows back into the disc through these holes (imbibition) as shown in the schematic diagram of Figure 1.3.1.

The flow constrictions as are provided by the "marrow contacts" result in high fluid velocity at the holes. Furthermore, flow through cartilage, or through any poroelastic material, causes drag forces on the matrix which are proportional to velocity. As shown schematically in Figure 1.3.2 such drag forces cause the cartilage matrix to either consolidate or expand, thereby opening or closing the pores in the matrix and correspondingly increasing or decreasing the resistance to flow [14].

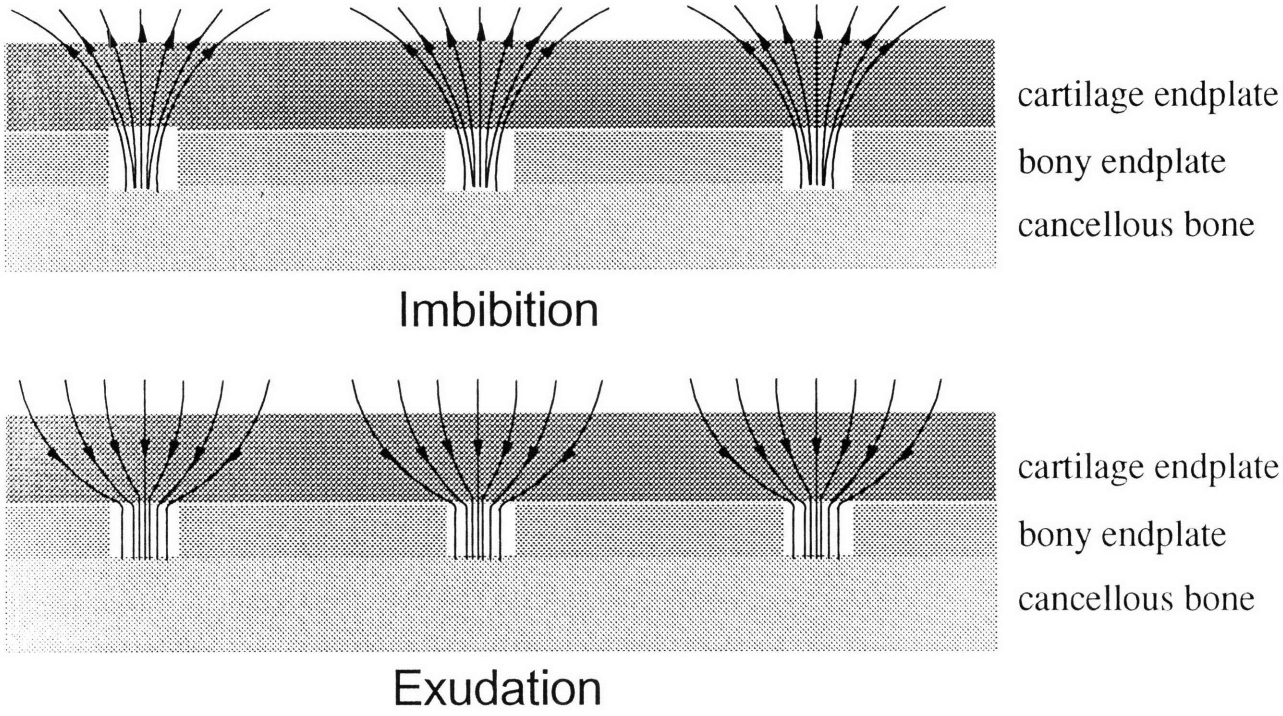

Figure 1.3.1 It is hypothesized that during daily spine loading the channels of the marrow contacts provide a path for fluid flow in the disc. Under the driving force of the fluid pressure the fluid is forced out of the disc through the cartilage endplates and into the vertebral bodies (exudation), and these small holes act to constrict the flow. During swelling the fluid flows back into the disc through these holes (imbibition).

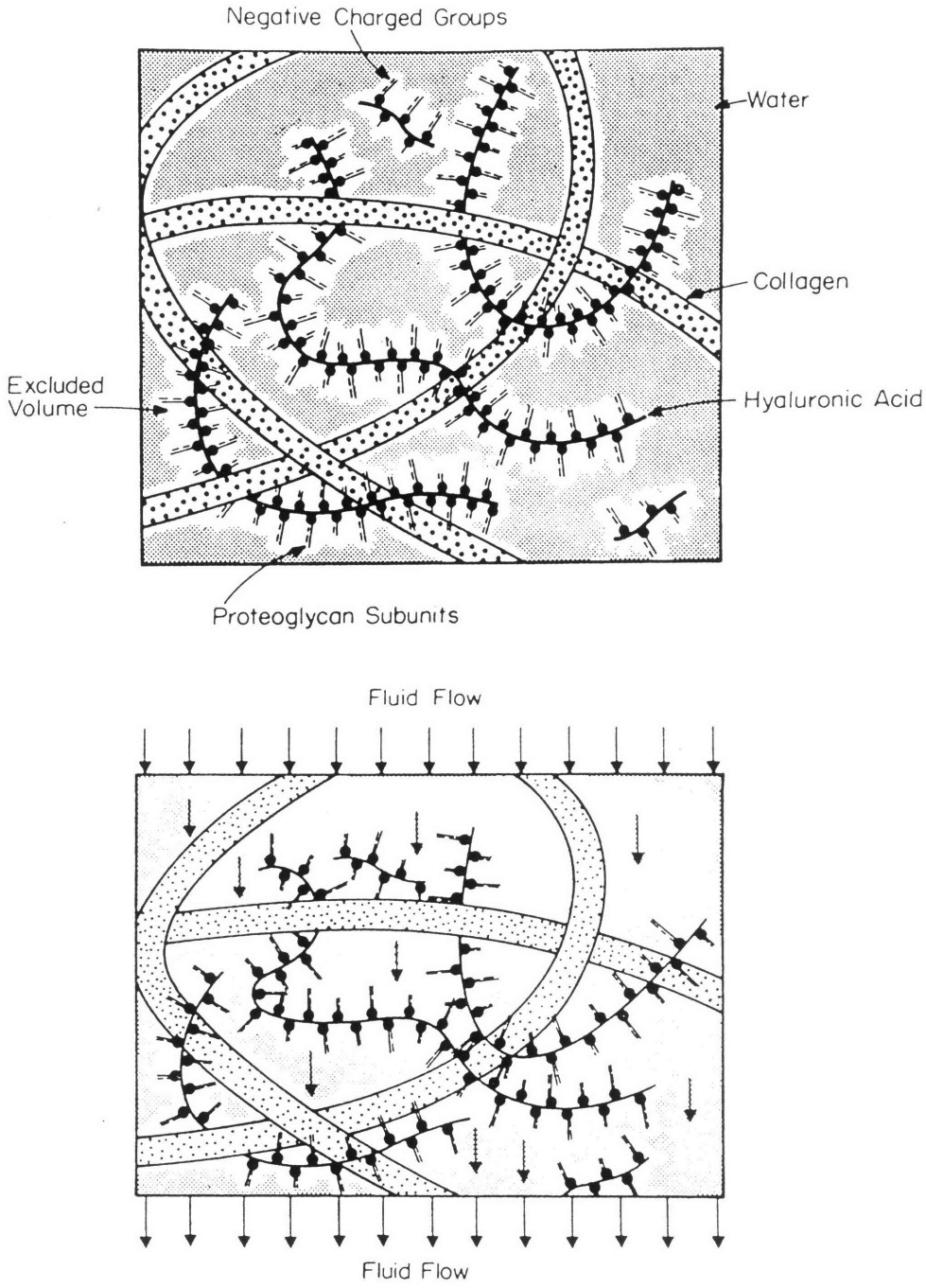

Figure 1.3.2 Flow through cartilage, or through any poroelastic material, causes drag forces on the matrix which are proportional to the fluid velocity. These drag forces cause the cartilage matrix to either consolidate or expand, thereby opening or closing the pores in the matrix and correspondingly increasing or decreasing the resistance to flow (sketch from Lai and Mow [14]).

This combination of the strain dependent permeability of the poroelastic cartilage and the underlying constriction holes of the bony endplate could supply the direction dependent resistance, or "almost one-way valve" which is necessary to maintain healthy disc hydration. As fluid is exuded from the disc the endplate cartilage matrix is compressed locally at the hole and the resistance is high. As fluid is imbibed into the disc, the cartilage matrix expands and the resistance is low. Without these holes, i.e. for the hypothetical case where the cartilage is supported on one side by an ideal zero-resistance support, there would be some drag-induced compression and expansion resulting in direction-dependent resistance. However, the ratio of resistance out to resistance in with an ideal support would be much lower and would probably not be sufficient to account for the ratio of the exudation driving force vs. the imbibition driving force (future models and experiments will compare the resistance ratio with and without constriction holes).

The swelling pressure effect of the proteoglycans in the disc and the relationship between water content and hydraulic permeability of the disc certainly contribute to the mechanical creep behavior by limiting the amount of fluid lost from the disc during loading. However, it is hypothesized that the necessary **direction dependence** of the resistance is provided by the mechanical "valve" of the cartilage endplate and constriction holes, and that this valve results in a sufficient exudation / imbibition resistance ratio, ensuring that all the fluid lost from the disc during loading is gained during rest.

1.3.2 OBJECTIVES

The aim of this project was to demonstrate the valve phenomenon provided by flow through a poroelastic solid and underlying constriction hole, to present arguments for the necessary existence of such a valve in the intervertebral disc, and to find evidence for the presence of the valve in the body.

1.3.3 SUMMARY

A physical model was designed and tested to demonstrate the valve phenomenon provided by the combination of flow through a poroelastic solid with strain-dependent permeability and stiffness and an underlying constriction hole. A finite element model was then validated against the experimental data from the physical model tests. This finite element model allowed the determination of the effect of various changes in model parameters, e.g. the "draining area" of the constriction hole (cross-sectional area of the volume of fluid draining into the hole) and applied pressure, on the valve behavior, and its validation will allow

modification in the future in order to represent the *in vivo* situation. From this *in vivo* model the effects of valve pathology and surgical intervention will be demonstrated (change in size and number of holes). Morphological studies were performed in order to determine the characteristics of the structures composing the valve in the body.

1.3.4 RELEVANCE

In light of the necessary mechanical valve provided by the cartilage endplate and constriction holes in the underlying cortical bone, the number and distribution of holes become important parameters in the maintenance of a healthy disc. Calcification of the cartilage endplate is a common problem which is often unrelated to age. A decrease in the size of the constriction holes and eventually the total number of holes due to calcification of the cartilage endplates would cause the velocity of fluid through the remaining holes to rise, resulting in a greater exudation resistance. If the exudation resistance became too high, the normal daily fluid loss from the disc would be decreased.

Such a disruption of the normal daily fluid flow could result in various problems in the disc. For example, a lack of nutrient supply to the disc, either through a decrease in diffusion due to a less permeable endplate or due to the reduced supply of larger solutes carried by the bulk flow, could lead to disc degeneration. In addition, assuming that the exudation of fluid from the disc normally results in a decreasing hydrostatic pressure over the course of daily loading [19], such a flow disruption would subject the tissues to abnormally sustained fluid stresses in the disc which could possibly result in various disc problems such as disc hernia, Schmorl's nodes or back pain.

The clinical application is therefore to open up holes in the bony endplate through the calcified cartilage layer in order to return the flow to its normal diurnal pattern and to relieve the disc pressure. This could be done using laser "drilling" with specially designed tools to allow holes of approximately 50 to 100 μm to be opened up in the bone. Diagnosis could be performed using magnetic resonance imaging of the disc at regular intervals throughout the day. If the disc water content remained high over the course of a day, this would indicate a flow disruption most likely due to hole blockage. Diagnosis could also be performed by monitoring the diurnal changes in intradiscal pressure. If these changes were abnormally small, this could indicate a flow disruption.

References

[1] Adams, M.A. and W.C. Hutton. The Effect of Posture on the Fluid Content of Lumbar Intervertebral Discs. *Spine,* **8**(6):p.665-71, 1983.

[2] Andersson, G.B.J. and A.B. Schultz. Effects of Fluid Injection on Mechanical Properties of Intervertebral Discs. *J Biomech,* **12**:p.453-8, 1979.

[3] Broberg, K.B. Slow Deformation of Intervertebral Discs. *J Biomech,* **26**(4/5):p.501-12, 1993.

[4] Brodin, H. Paths of Nutrition in Articular Cartilage and Intervertebral Discs. *Acta Orthop Scand,* **24**(3):p.177-83, 1954.

[5] Cassidy, J.J., A. Hiltner and E. Baer. The response of the hierarchical structure of the intervertebral disc to uniaxial compression. *J Mat Med,* **1**:p.69-80, 1990.

[6] Cassidy, J.J., M.S. Silverstein, A. Hiltner, *et al.,* A water transport model for the creep response of the intervertebral disc. *J Mat Med,* **1**:p.81-9, 1990.

[7] Crock, H.V. and M. Goldwasser. Anatomic Studies of the Circulation in the Region of the Vertebral End-Plate in Adult Greyhound Dogs. *Spine,* **9**(7):p.702-6, 1984.

[8] Gray, H. Gray's Anatomy. R. Warwick and P.L. Williams, eds., 35th ed. Edinburgh, Longman, 1973,

[9] Holm, S., A. Maroudas, J.P.G. Urban, *et al.,* Nutrition of the Intervertebral Disc: Solute Transport and Metabolism. *Conn Tiss Res,* **8**:p.101-19, 1981.

[10] Kazarian, L.E. Creep Characteristics of the Human Spinal Column. *Orthop Clin of N America,* **16**:p.3-18, 1975.

[11] Keller, T.S., D.M. Spengler and T.H. Hansson. Mechanical Behavior of the Human Lumbar Spine. I. Creep Analysis During Static Compressive Loading. *J Orthop Res,* **5**:p.467-78, 1987.

[12] Koeller, W., F. Funke and F. Hartmann. Biomechanical Behavior of Human Intervertebral Discs Subjected to Long Lasting Axial Loading. *Biorheology,* **21**:p.675-86, 1984.

[13] Koeller, W., S. Muehlhaus, W. Meier, *et al.,* Biomechanical Properties of Human Intervertebral Discs Subjected to Axial Dynamic Compresion - Influence of Age and Degeneration. *J Biomech,* **19**(10):p.807-16, 1986.

[14] Lai, W.M. and V.C. Mow. Drag-Induced Compression of Articular Cartilage During a Permeation Experiment. *Biorheology,* **17**:p.111-23, 1980.

[15] Markholf, K.L. and J.M. Morris. The Structural Components of the Intervertebral Disc. *JBJS,* **56-A**(4):p.675-87, 1974.

[16] Maroudas, A. The Joints and Synovial Fluid. In *Physical Chemistry of Articular Cartilage and the Intervertebral Disc.* Ch.6, L. Sokoloff, London, Academic Press, 1980, p.239-91.

[17] Maroudas, A. Tissue Nutrition and Viability. In *Mechanisms of Fluid Transport in Cartilaginous Tissues.* Ch.3, A.R. Hargens, New York, Springer-Verlag, 1986, p.47-71.

[18] Maroudas, A. and J.P.G. Urban. Studies in Joint Diseases. In *Swelling Pressures of Cartilaginous Tissues.* Ch.3, A. Maroudas and E.J. Holborow, London, Pitman Medical Publishers, 1980, p.87-116.

[19] McNally, D.S. and M. Adams. Internal Intervertebral Disc Mechanics as Revealed by Stress Profilometry. *Spine,* **17**(1):p.66-73, 1992.

[20] Nachemson, A. Lumbar Intradiscal Pressure; Experimental studies on post-mortem material. Copenhagen, Acta Orthop Scand Supplement, 1960,

[21] Nachemson, A. Some Mechanical Properties of the Lumbar Intervertebral Discs. *Bull Hosp Jt Dis,* **23**:p.130-43, 1962.

[22] Nachemson, A. and G. Elfstroem. Intravital Dynamic Pressure Measurements in Lumbar Discs. Stockholm, The Almqvist and Wiksell Periodical Co. 1970, p.14.

[23] Nachemson, A., T. Lewin, A. Maroudas, *et al.,* In Vitro Diffusion of Dye Through the End-Plates and the Annulus Fibrosus of Human Lumbar Inter-vertebral Discs. *Acta Orthop Scand,* **41**:p.589-607, 1970.

[24] Ogata, K. and L.A. Whiteside. Nutritional Pathways of the Intervertebral Disc, An Experimental Study Using Hydrogen Washout Technique. *Spine,* **6**(3):p.211-6, 1981.

[25] Oki, S., Y. Matsuda, T. Itoh, *et al.,* Scanning Electron Microscopic Observations of the Vascular Structure of Vertebral End-Plates in Rabbits. *J Orthop Res,* **12**:p.447-9, 1994.

[26] Smeathers, J.E. and D.N. Joanes. Dynamic Compressive Properties of Human Lumbar Intervertebral Joints: A Comparison Between Fresh and Thawed Specimens. *J Biomech,* **21**(5):p.425-33, 1988.

[27] Urban, J., S. Holm and A. Maroudas. Diffusion of Small Solutes into the Intervertebral Disc: An *In Vivo* Study. *Biorheology,* **15**:p.203-23, 1978.

[28] Urban, J.P.G. Factors Influencing the Fluid Content of Intervertebral Discs. *Adv Microcirc,* **13**:p.160-70, 1987.

[29] Urban, J.P.G. and D.H. Bergel. Effect of Age on the Fluid of the Intervertebral Disc. *Society for Back Pain Research Conference Proceedings,* **The Ageing Spine** 1987.

[30] Urban, J.P.G., S. Holm, A. Maroudas, *et al.,* Nutrition of the Intervertebral Disc, An *In Vivo* Study of Solute Transport. *Clin Orthop and Rel Res,* **129**:p.101-14, 1977.

[31] Urban, J.P.G., S. Holm, A. Maroudas, *et al.,* Nutrition of the Intervertebral Disc, Effect of Fluid Flow on Solute Transport. *Clin Orthop and Rel Res,* **170**:p.296-302, 1982.

[32] Urban, J.P.G. and A. Maroudas. The Measurement of Fixed Charge Density in the Intervertebral Disc. *Biochim et Biophys Acta,* **586**:p.166-78, 1979.

[33] Urban, J.P.G. and A. Maroudas. Swelling of the Intervertebral Disc *In Vitro. Conn Tiss Res,* **9**:p.1-10, 1981.

[34] Urban, J.P.G., A. Maroudas, M.T. Bayliss, *et al.,* Swelling Pressures of Proteoglycans at the Concentrations Found in Cartilaginous Tissues. *Biorheology,* **16**:p.447-64, 1979.

[35] Urban, J.P.G. and J.F. McMullin. Swelling Pressure of the Intervertebral Disc: Influence of Proteoglycan and Collagen Contents. *Biorheology,* **22**:p.145-57, 1985.

[36] Urban, J.P.G. and J.F. McMullin. Swelling Pressure of the Lumbar Intervertebral Discs: Influence of Age, Spinal Level, Composition and Degeneration. *Spine,* **13**(2):p.179-87, 1988.

,

CHAPTER
TWO

MORPHOLOGY

2.1 INTRODUCTION

A morphological study of the surface of the bony endplate of the sheep and human vertebrae was carried out in order to demonstrate the presence of constriction holes, and to quantify their characteristic parameters. These parameters then allowed an estimation of the flow properties in the disc such as the velocity and volume flow rate and were later used in modeling the valve mechanism.

2.1.1 BACKGROUND

The cartilage endplate of the intervertebral disc consists of hyaline cartilage, similar to that of articular cartilage. This cartilage lies over the surface of the vertebral body underneath the nucleus pulposus as shown schematically in Figure 2.1.1. At the outer periphery of the disc the annular lamellae merge directly into the subchondral bone of the vertebrae [6]. The underlying bony endplate is composed of cortical bone which forms part of the cortical shell of the vertebral bodies, as shown in Figure 2.1.2. This endplate is perforated by many small holes which provide channels from the cancellous bone of the vertebral bodies to the cartilage endplate. These channels have been observed in vascularity studies since they

house the blood vessels which supply nutrients to the avascular disc [2,13]. While these holes may provide openings for the vascular buds where the exchange of nutrients takes place, it is probable that they also provide channels for fluid flow into and out of the disc. It is hypothesized that the combined behavior of flow through the cartilage endplate and these underlying constriction holes in the bony endplate provides the necessary valve phenomenon in the intervertebral disc.

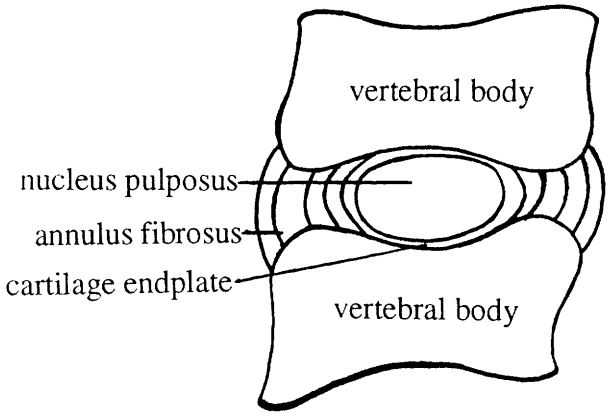

Figure 2.1.1 Schematic diagram of the spinal motion segment showing the location of the nucleus pulposus, annulus fibrosus and cartilage endplate.

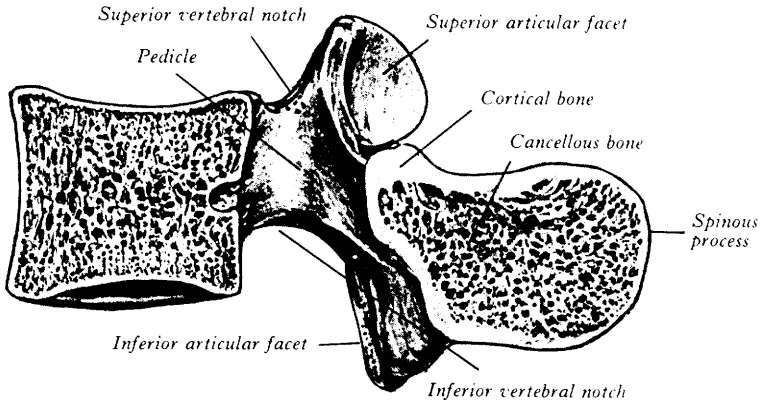

Figure 2.1.2 Medial sagittal section through a lumbar vertebra showing the bony endplate forming part of the cortical shell of the vertebra. (from Gray's Anatomy [17]).

2.1.2 PREVIOUS RESEARCH

Vascular Anatomy and Morphology of the Disc and Endplate

In several studies "marrow contacts" have been observed in the intervertebral disc. These contacts form channels through the bony endplate from the trabecular bone of the vertebral bodies to the cartilage endplates as shown in Figure 2.1.4. In a study of the diffusion of glucose in the disc Maroudas *et al.* [9] investigated the vertebral marrow vessels and quantified the contacts between the marrow spaces and the disc tissue. They correlated the number of contacts found with the level of diffusion of solute into the disc. They also found that the proportion of the bone-cartilage interface occupied by marrow spaces was higher in the central region under the nucleus than in the periphery under the annulus. The vessels were found to frequently penetrate the bony endplate to lie in or abut on the cartilage endplate.

In a study of the diffusion pathways in the discs of adult dogs Ogata and Whiteside [12] noticed that the bone-cartilage interface was perforated by many small "holes" which corresponded to these same marrow contacts as found by Maroudas *et al.* [9], and that these holes contained vascular buds which projected into the cartilage endplate. Crock and Goldwasser [2] injected the vertebral veins of adult greyhound dogs with a mixture of Japanese ink and barium sulfate and demonstrated the capillary system at the disc bone interface clearly. A continuous and dense capillary bed was found at the nucleus - bone interface and became more sparse in the peripheral regions underlying the annulus. The buds were found to drain into both a transverse collecting vein system running parallel to the bony endplate as well as directly into the veins of the marrow spaces as shown in Figure 2.1.3. Figure 2.1.4 shows the detail of the capillary bed found at the cartilage/bone interface.

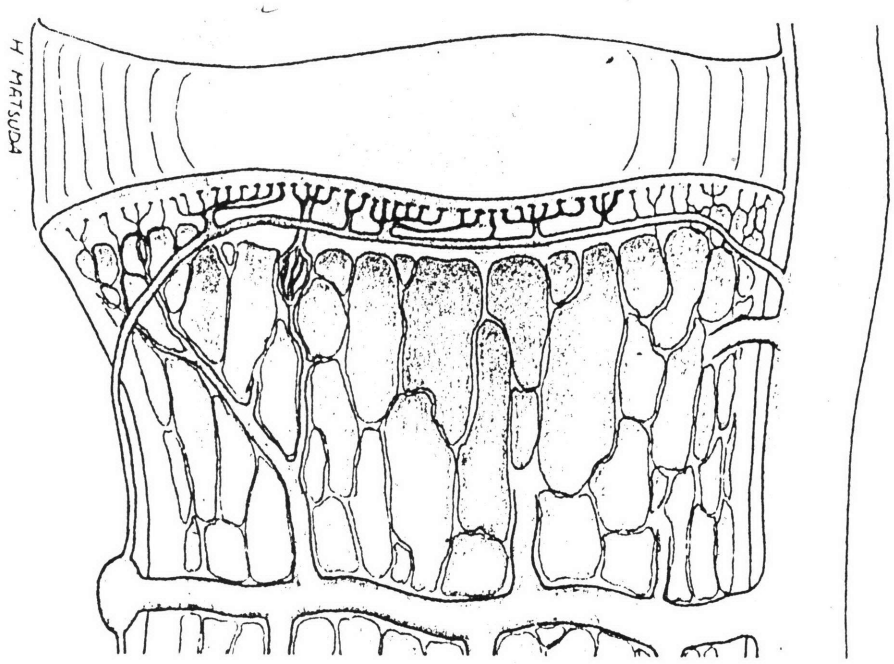

Figure 2.1.3 Sketch of the capillary system in the vertebral body showing the detailed anatomy of the capillary bed at the cartilage/bone interface (Crock and Goldwasser [2]).

Figure 2.1.4 The capillary bed at the cartilage/bone interface in the intervertebral disc (Hukins *et al.* [6]).

Simon *et al.* [14] also observed in both human and rhesus spinal motion segments large "pores" or passages in the endplate, through which fluid flow would be possible. Oki *et al.* [13] observed the vascular structure of the vertebral end plates in rabbits using scanning electron microscopy. They isolated the blood vessels using a vascular corrosion cast and observed the vessels extending from the deep subchondral bone up to the vertebral end plate. Taylor and Twomey [15] write that the blood vessels found at the cartilage endplate in the human gradually disappear during growth and are gone by the age of approximately twenty-five, and that in the adult few blood vessels perforate the bony endplate. However, Crock *et al.* [3] claim that a clearly defined capillary bed remains within the cartilage endplate in adult dogs, but that changes during growth do occur in the venous drainage system with the appearance of a horizontal subarticular collecting vein system.

The vascular supply is important in the nutrition of the disc as a location of solute exchange through diffusion [11]. While these vessels certainly play an important physiologic role in disc nutrition, it is hypothesized that fluid flow takes place through these small "holes" or marrow contacts in which the vessels lie. These holes would therefore play an important role in the mechanical behavior of the fluid flow into and out of the disc. The contribution of bulk flow to disc nutrition has been studied to some extent and this flow seems to contribute to the exchange of larger solutes in the disc [8,16].

2.2 MATERIALS AND METHODS

2.2.1 SCANNING ELECTRON MICROSCOPY OF THE SHEEP BONY ENDPLATE

The intact cortical surfaces of the bony endplate of adult, female, sheep lumbar vertebrae (L2, L3 and L4), both frozen (-20°C for 4 months) and fresh, were observed with a scanning electron microscope (HITACHI 4100 Field Emission Scanning Electron Microscope) in order to determine the size, number and distribution of marrow contact holes. All samples were first macerated in a 1% papain solution and the frozen sample (Sheep Sample A) was bleached in a 2% hydrogen peroxide solution. Cracks were observed in the surface of this sample with SEM and were thought to be due to freezing or to hydrogen peroxide bleaching. Therefore, vertebrae from a freshly excised spine were also studied, one sample bleached in hydrogen peroxide (Sheep Sample B) and one unbleached sample (Sheep Sample C). These samples were mounted and sputter coated with 8 nm gold and were observed with the scanning electron (SE) microscope at accelerating voltages of 10.0 kV to 15.0 kV, according to the depth of image desired. All images were found using secondary electron imaging.

The bony endplates of two vertebrae from the freshly excised spine were also studied in cross-section. Both samples (Sheep Sample D and Sheep Sample E, taken from the L3 and L4 vertebrae respectively) were macerated and bleached as above, set in methacrylate resin, and sectioned cross-sectionally, anterior-posteriorly, in 100 μm slices. The samples were mounted and sputter coated, and in this case a back-scattered electron technique was used, which distinguished the density of the resin from the density of bone, in order to observe the marrow contact channels (which were filled with resin) in the bony endplate.

2.2.2 SCANNING ELECTRON MICROSCOPY OF THE HUMAN BONY ENDPLATE

A similar process as that of the sheep spine samples was carried out with the intact cortical surfaces of the bony endplates of frozen adult human lumbar vertebrae (L3). The vertebrae studied were taken from two different specimens (Human Sample A: male, 78 years old; Human Sample B: male, 52 years old). Both samples were macerated in papain, bleached in hydrogen peroxide and dehydrated. They were mounted and sputter coated with 8 nm gold and were observed with the SE microscope at accelerating voltages of 3.0 kV to 6.0 kV. All images were found using secondary electron imaging.

2.2.3 IMAGE ANALYSIS

The images of the surface of the bony endplate found using SEM were analyzed with an image analysis and measurement package (PC-Image, Foster Findlay) in order to quantify the average size and number of holes in both the sheep samples and human samples, and to find the distribution of hole size in the bony endplates. The system was first calibrated according to the magnification of the SEM images, which were imported directly into the computer from the microscope. The images were then digitized and upper and lower contrast threshold limits were set. An attempt was made to remove noise by visual threshold adjustment, however, it proved difficult to remove all noise without sacrificing some of the valid hole area. Thus, as much noise was removed as possible through threshold adjustment and the rest was eliminated by choosing a minimum hole size and discarding any data below this minimum.

2.3 RESULTS AND DISCUSSION

2.3.1 SCANNING ELECTRON MICROSCOPY OF THE SHEEP BONY ENDPLATE

Scanning electron images of the frozen sheep sample are shown in Figure 2.3.1. The cracks observed in the surface appeared to initiate from the holes and were thought to be due to the freezing process or possibly to bleaching with hydrogen peroxide. The "funnel" shape of the holes, i.e. smaller openings through the bottom of larger holes as in Figure 2.3.1.c, could possibly allow space for the vascular buds to sit, but it is not clear whether this phenomenon is natural or an artifact due to sample preparation. Another possibility is that some calcification of the cartilage endplate has taken place and this calcified layer is in fact lying on top of the original surface of the bony endplate in which the smaller holes exist. High magnification images as in Figure 2.3.1.c revealed clearly that the holes channel into the trabecular bone of the vertebral bodies.

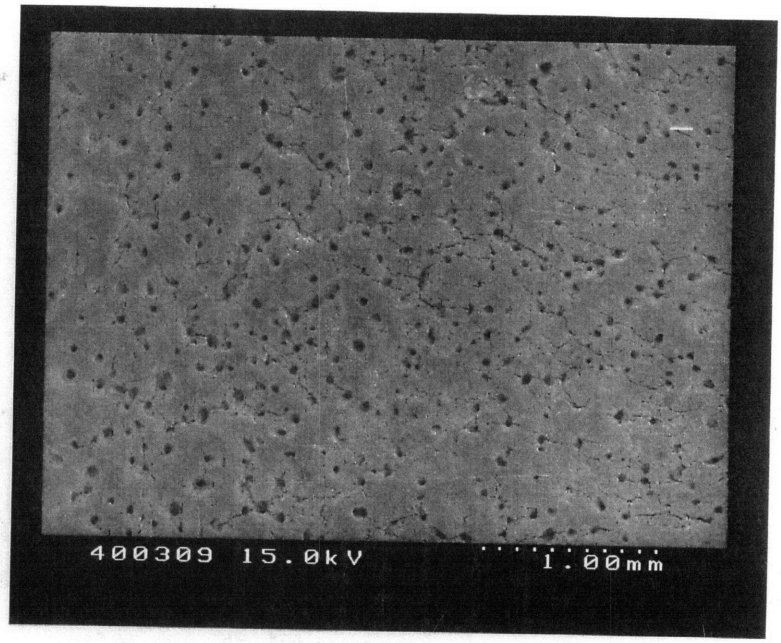

a

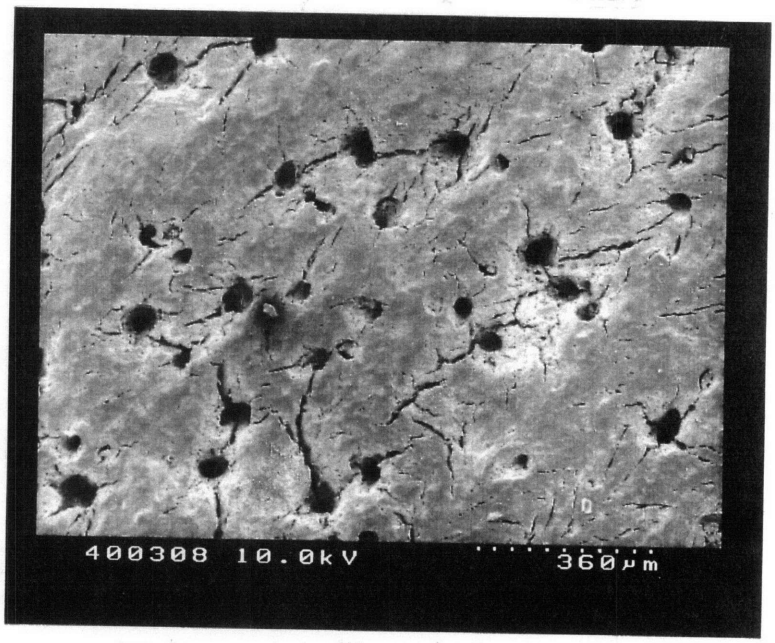

b

Figure 2.3.1 Scanning electron micrographs of the bony endplate surface of Sheep Sample A at various magnifications: a) 20X, b) 60X.

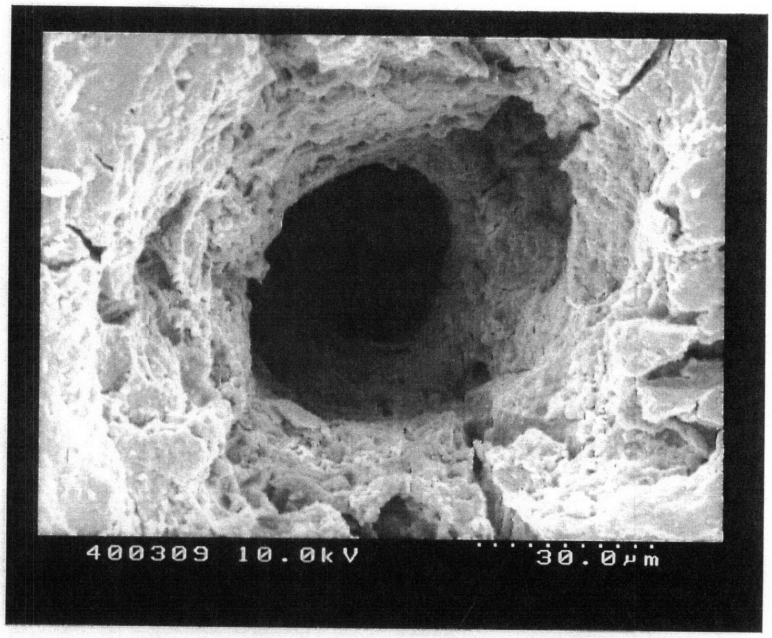

c

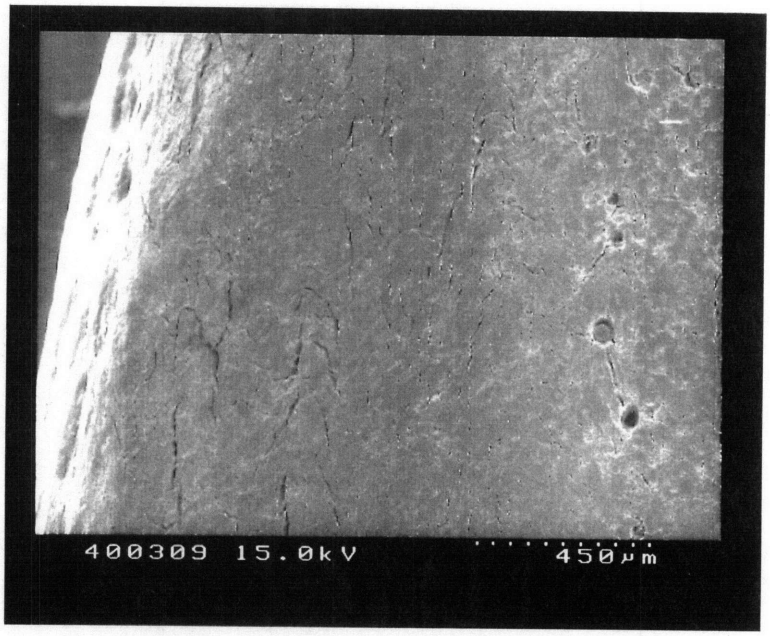

d

Figure 2.3.1 Cont'd. Scanning electron micrographs of the bony endplate surface of Sheep Sample A at various magnifications: c) 750X. Image d) is taken in the peripheral zone; magnification 50X.

Observation of the images by eye revealed the average size of the small underlying holes to be approximately 30 μm in diameter, while that of the larger top surface holes to be approximately 60 μm in diameter. The distribution of the holes appeared quite random, and no holes were observed around the periphery as shown in Figure 2.3.1.d.

Images of the fresh sheep samples, as shown in Figure 2.3.2 and 2.3.3, revealed by eye approximately the same average size of holes and distribution of holes as in the frozen sample. Cracks propagating from the holes were again found in the samples both with and without hydrogen peroxide bleaching. Thus, freezing and bleaching could both be ruled out as the cause of cracking. It is possible that the collagen fibers of the cartilage endplate are pre-stressed in tension and when this tension is released during the denaturing process the bone may crack [personal communication with N. Bishop]. Again, no holes were observed at the periphery of the surface as shown in Figure 2.3.4.

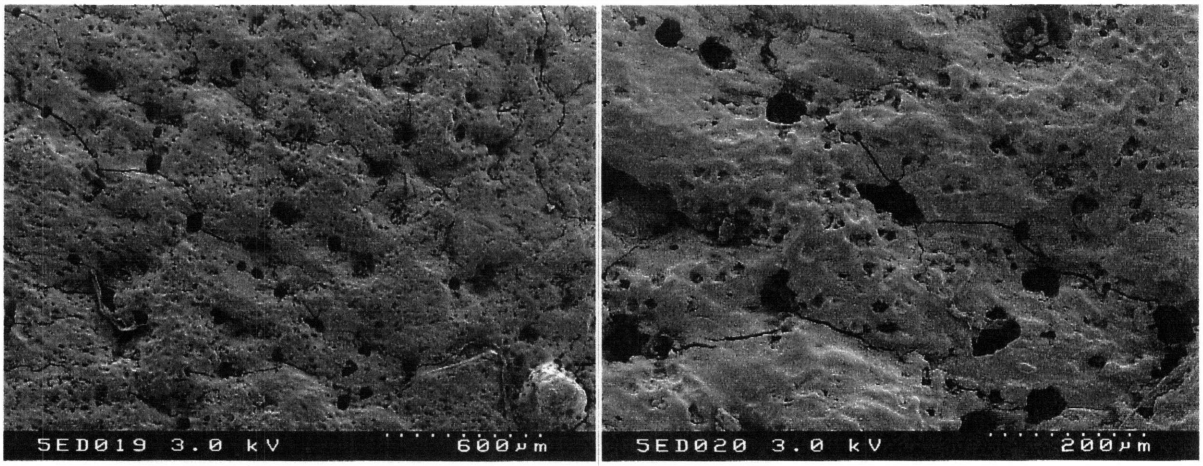

a b

Figure 2.3.2 Scanning electron micrographs of the bony endplate surface of Sheep Sample B. Magnification a) 30X, b) 90X.

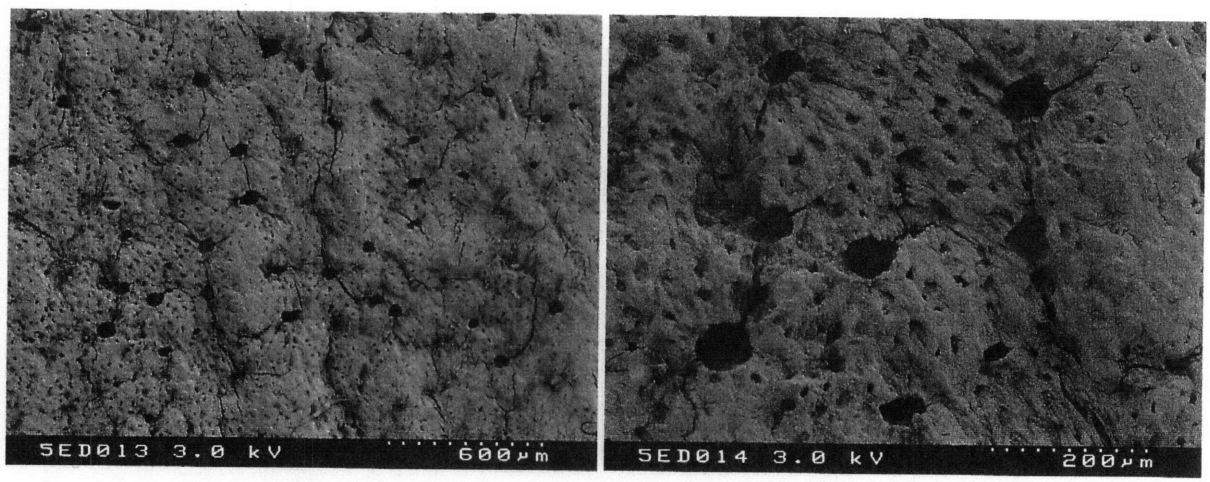

Figure 2.3.3 Scanning electron micrographs of the bony endplate surface of Sheep Sample C. Magnification a) 30X, b) 90X.

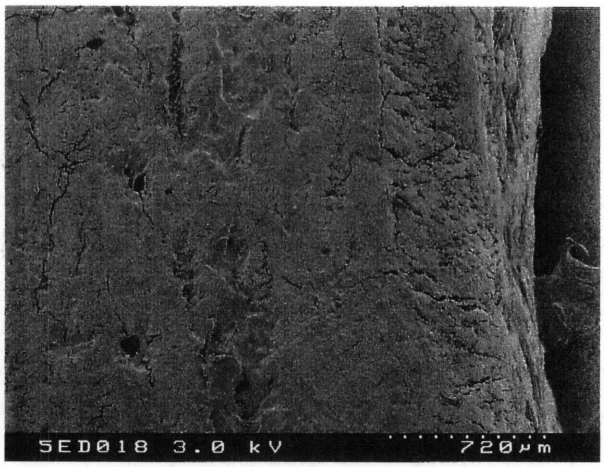

Figure 2.3.4 Scanning electron micrograph of the peripheral zone of the bony endplate surface of Sheep Sample B. Magnification 26X.

Many smaller holes of diameters approximately one fifth to one tenth of the main holes were distributed over the surface of the fresh sheep samples, as shown in Figures 2.3.2 and 2.3.3. A higher magnification image (Figure 2.3.5) revealed that these holes did not penetrate through the bony endplate to the trabeculae; rather they appeared rather to form "pock-marks" in the surface. These smaller holes were not observed in the frozen sample of Figure 2.3.1, and are possibly due to some degenerative process such as osteoporosis, since the fresh

samples were taken from the spine of an eleven year old sheep. However, this effect was not observed in the osteoporotic human samples, as discussed below.

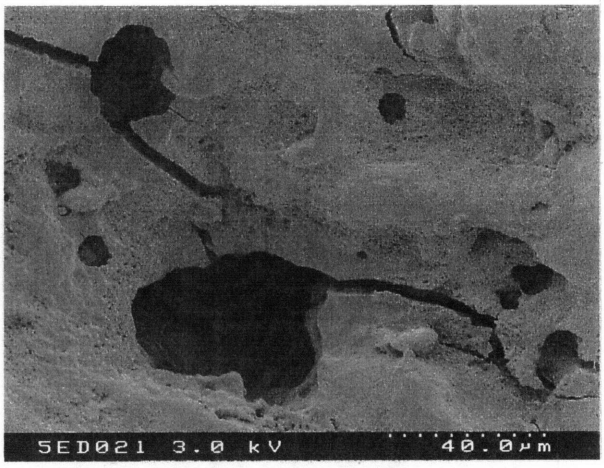

Figure 2.3.5 Scanning electron micrograph showing a close-up view of the small "pock-marks" found in the surface of the bony endplate of Sheep Sample B. These small holes did not appear to channel into the trabecular bone of the vertebra.

The cross-section images of Sheep Samples D and E are shown in Figures 2.3.6 and 2.3.7. These images show clearly the channeling of the marrow contacts into the trabeculae of the vertebral bodies from the surface of the bony endplate. In Figure 2.3.7.b the channel has probably been cut off by histological sectioning. From these images the "pock-marks" in the surface can be observed in cross section, and it appears that they do not channel through to the trabeculae.

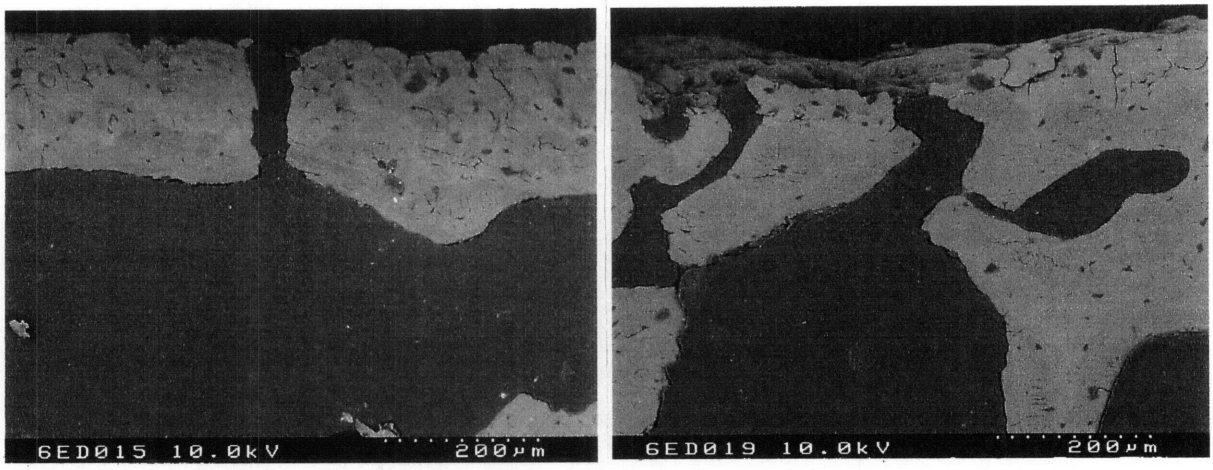

Figure 2.3.6 Scanning electron micrographs of the cross-section of the bony endplate and underlying trabeculae at two locations on Sheep Sample D.

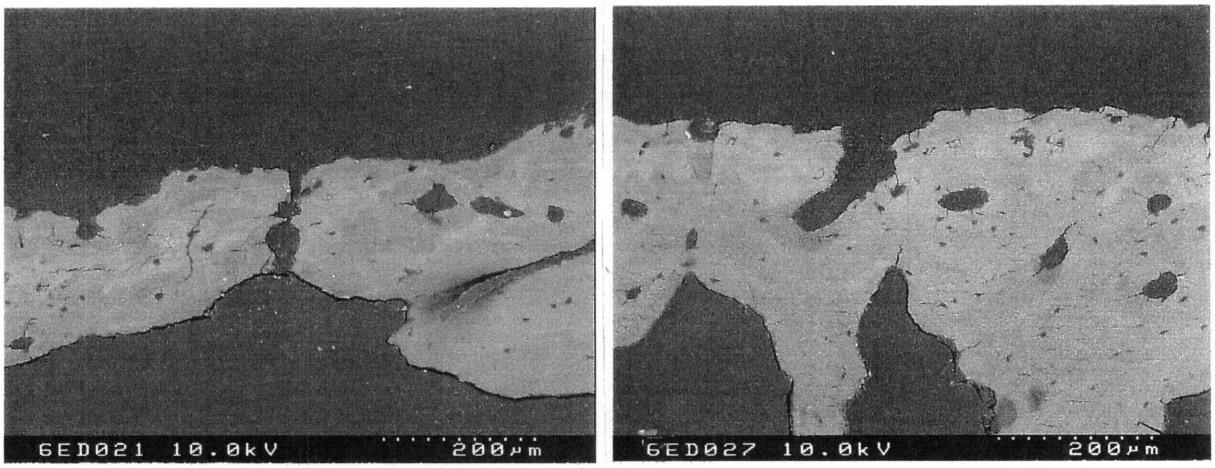

Figure 2.3.7 Scanning electron micrographs of the cross-section of the bony endplate and underlying trabeculae at two locations on Sheep Sample E.

2.3.2 SCANNING ELECTRON MICROSCOPY OF THE HUMAN BONY ENDPLATE

Somewhat larger holes than those of the sheep vertebrae were observed in the human vertebral surface. Observation by eye revealed holes of an average diameter of approximately 100 µm as shown in Figures 2.3.8 and 2.3.9. There appeared to be a larger distribution of hole size in the human endplate than in the sheep; from 50 µm to 200 µm in diameter. The distribution of holes again appeared random and there were very few holes in the peripheral regions.

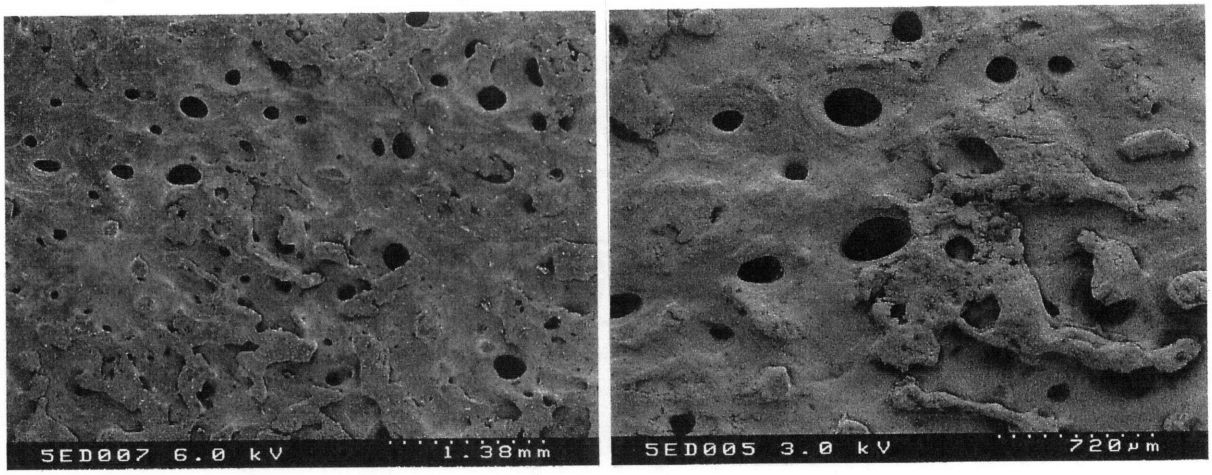

a b

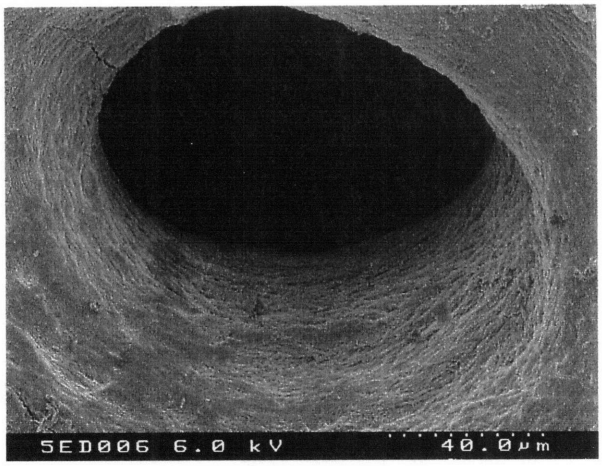

c

Figure 2.3.8 Scanning electron micrographs of the bony endplate surface of Human Sample A. Magnification a) 13X, b) 26X and c) 460X.

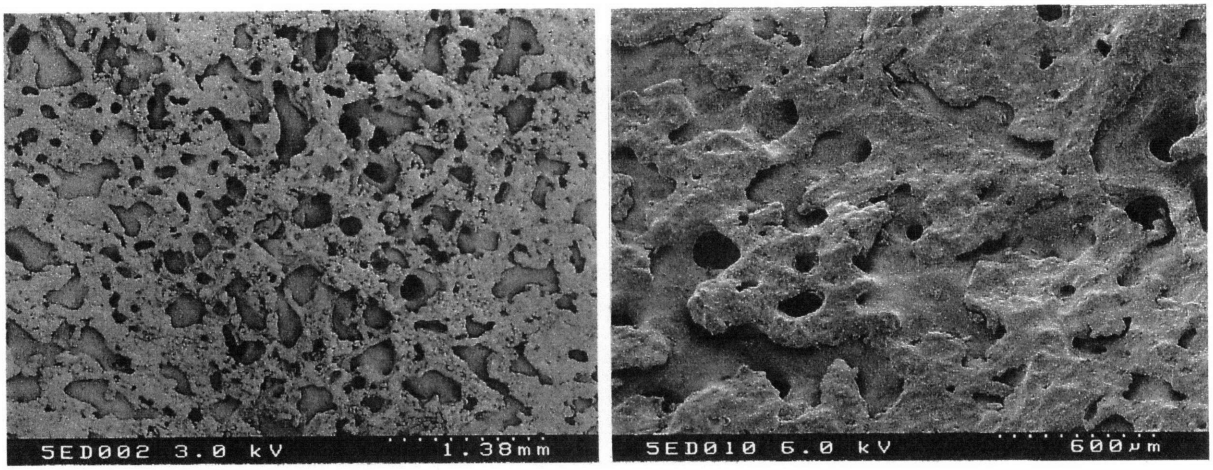

a b

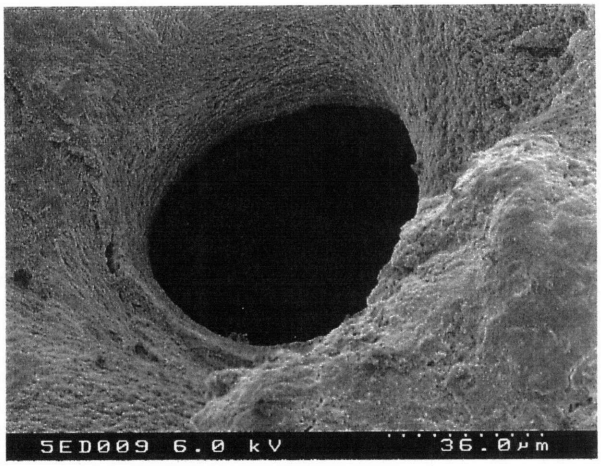

c

Figure 2.3.9 Scanning electron micrographs of the bony endplate surface of Human Sample B. Magnification a) 13X, b) 26X and c) 460X.

In both specimens an interesting observation was the presence of a deposit on the surface of the bone. This deposit could be calcified cartilage and can be seen in some places to be lying over the holes, particularly in the specimen of Figure 2.3.9, but also to some extent in Figure 2.3.8. These images demonstrate how cartilage calcification could effectively decrease the size, and eventually the total number of constriction holes in the bony endplate. This observation has important clinical implications since it demonstrates a possible disc pathology directly related to the valve phenomenon. As the holes close resistance to flow would increase, resulting in the disruption of the daily fluid exchange in the disc. This

disruption could lead to abnormal stresses in the disc tissues or an insufficient nutrient supply due to the bulk flow disruption directly or to a decreased level of diffusion as the bony endplate becomes less and less permeable. The effect of a decrease in the number of holes is demonstrated for the physical model using finite elements in Chapter 4.

In both human spine samples severe degeneration and dehydration of the discs was observed. In addition, the bone of the vertebrae was observed by eye to be highly osteoporotic, and large osteophytes were found on several vertebrae. These were the only human samples available at the time and although, due to the age of the donors and degenerative state of the tissue, the bony endplates observed do not represent those of normal healthy spine, the observations made provide important information about the possible effects of degeneration of the disc and/or bone on the valve phenomenon. Morphological studies of young, healthy spine are also necessary and will be carried out in the future.

2.3.3 IMAGE ANALYSIS

The distribution of hole sizes found by image analysis of the SEM pictures are shown in Figures 2.3.10 through 2.3.14. When analyzing the images the gray-scale threshold was adjusted to eliminate any noise due to shadow induced by irregularities in the surface. However, it proved difficult to remove all noise in this way, and in all samples except Sheep Sample A, a relatively high frequency was found for the smallest hole radii, as shown in the histograms of Figures 2.3.11 to 2.3.14. In each case therefore, a minimum radius cut-off point was chosen according to the histograms (the high frequency of small radii holes were neglected in each case) and according to the smallest observable hole in the images.

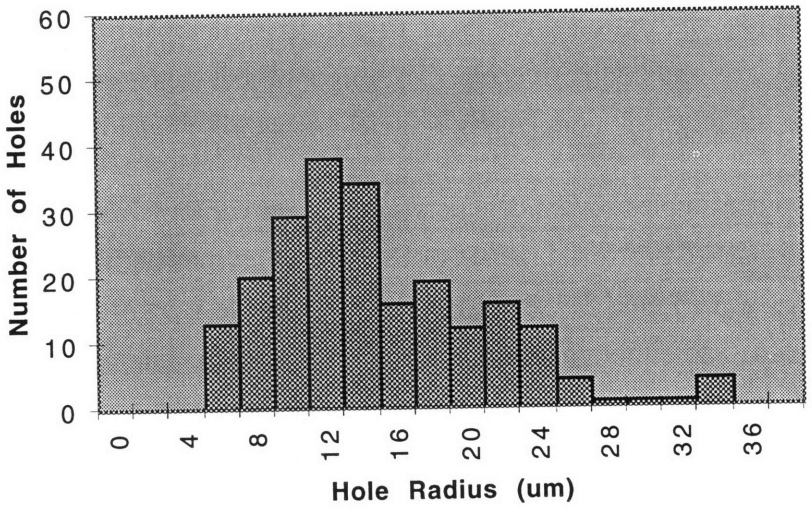

Figure 2.3.10. Sheep Sample A. The total area of the bone analyzed was 6.12 mm^2 (this is approximately two times greater than that of Sheep Samples B or C; thus the greater total number of holes counted).

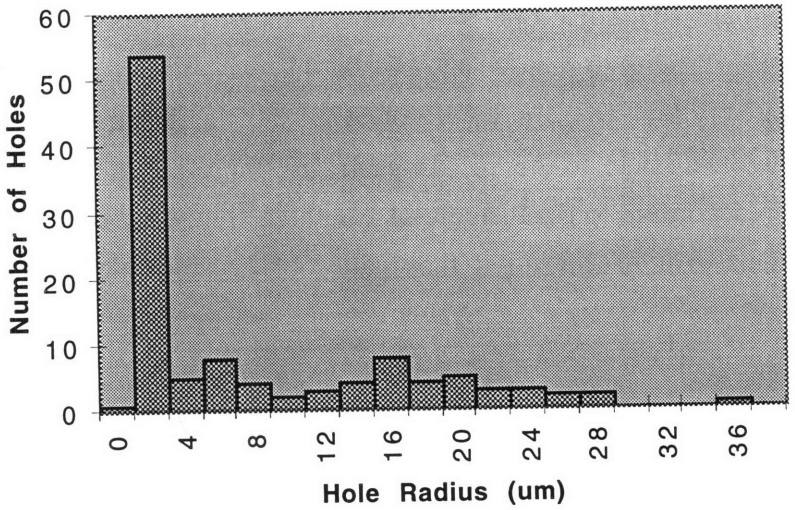

Figure 2.3.11. Sheep Sample B. The total area of the bone analyzed was 2.91 mm^2.

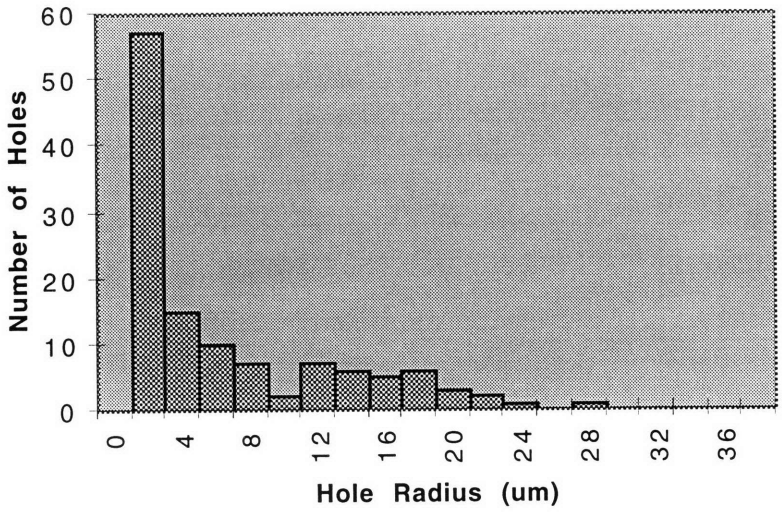

Figure 2.3.12. Sheep Sample C. The total area of bone analyzed was 2.88 mm^2.

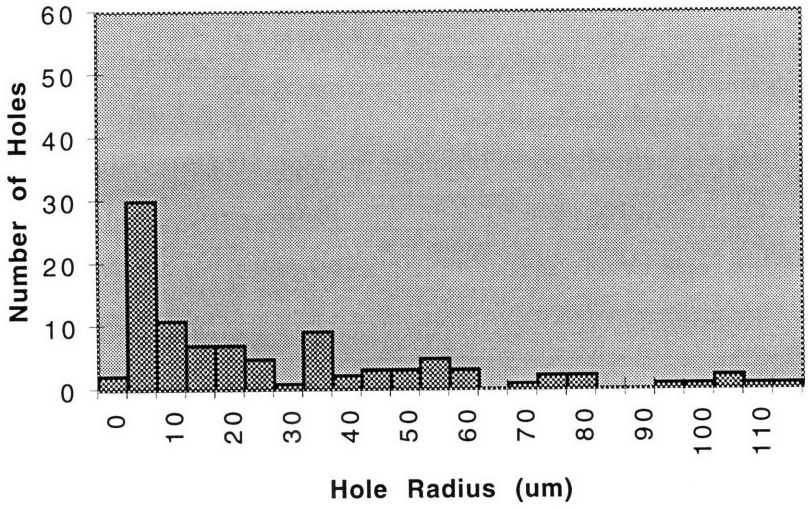

Figure 2.3.13. Human Sample A. The total area of bone analyzed was 15.1 mm^2.

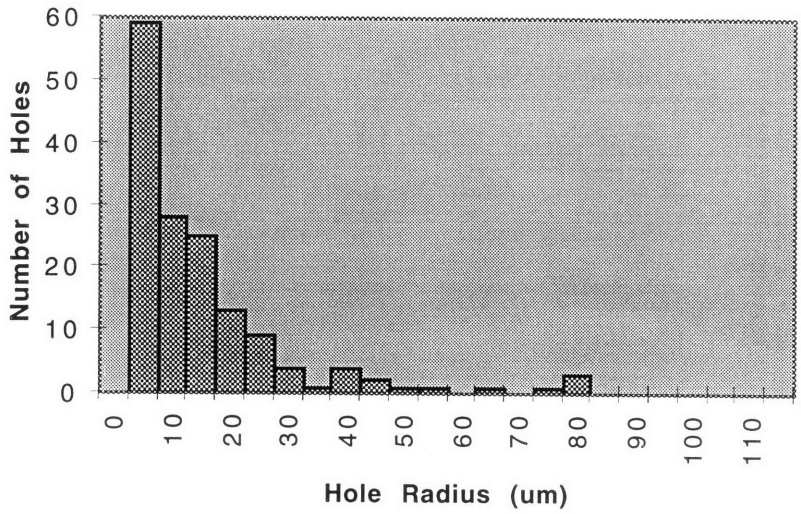

Figure 2.3.14. Human Sample B. The total area of bone analyzed was 15.3 mm^2.

The distributions of the hole sizes in all cases except Sheep Sample A were positively skewed. Thus, values of the median, range (min., max.), and the first and third quartiles are presented as opposed to those of the mean and standard deviation (used for normal distributions). Table 2.3.1 lists these values for the hole radii as well as the total percent hole area to surface area for all samples studied. The minimum cut-off hole radius is also listed. The total real number of constriction holes in the intervertebral disc was estimated for an average bony endplate surface area of 300 mm^2 in the sheep and 700 mm^2 in the human [personal measurements] and using the median radius value for the holes.

Sample	Median hole radius (μm)	Percent total hole area of surface area (%)	Cut-off radius (μm)	Max. radius (μm)	First Quartile (Q1)	Third Quartile (Q3)	Total real no. of holes in bony endplate
Sheep A	14.7	3.3	-----	35.1	11.8	19.5	14600
Sheep B	16.5	1.8	4.0	36.3	9.3	20.6	6310
Sheep C	10.9	1.4	4.0	29.3	6.2	17.1	11250
Human A	36.0	3.7	10.0	116.0	18.2	57.6	6360
Human B	18.6	1.8	10.0	84.5	14.2	26.9	11230

Table 2.3.1 Values found from image analysis of SEM images.

The histograms in Figures 2.3.10 to 2.3.14 show that a much larger distribution in hole size was found in the human samples than in the sheep samples. According to the data in Table 2.3.1 the median hole size in the human samples was approximately 1.5 to 3.5 times that found in the sheep samples. Furthermore, the maximum hole radii found in the human samples were two to four times greater than those found in the sheep.

The percentage total hole area of the total surface area for the sheep and human samples were similar. Sheep A and Human A were comparable at 3.3% and 3.7%, while Sheep B and C, and Human B were alike at 1.8%, 1.4%, and 1.8% respectively. Sheep samples B and C were from the same sheep which had been sacrificed due to old age, while a deposit of calcified cartilage was observed on the surface of Human sample B (see Figure 2.3.9). This would explain the relatively low hole area percentage of Human sample B when compared with Human sample A (in which less deposit was observed), and could also explain the relatively low hole area percentage found in Sheep samples B and C. That is, while no clearly defined deposit was observed in these sheep samples (see Figures 2.3.2 and 2.3.3) it is possible that the entire surface had been covered by the calcified cartilage endplate, thus reducing the total number of holes and therefore the hole area percentage.

While Human sample B was found to have a smaller median radius and a lower hole area percentage, the number of holes per unit area was higher than in Human sample A. This may have been caused by the calcification of the cartilage endplate which could have resulted in the splitting of the holes into two or more smaller holes, thus decreasing the size, but in fact increasing the total number of holes.

Sheep samples B and C proved to have similar hole area percentages (1.8% and 1.4% respectively), which could be expected since the samples came from the same sheep. However, the median radius of the holes in sample C was slightly smaller than that in sample B; therefore, sample C had a greater total number of holes in the bony endplate. This indicates that the size and number of holes may depend on the location of the vertebrae in the spine, but that the hole area percentage of the surface area is maintained at some value throughout the spine. In fact, as demonstrated with the finite element model in Chapter 4, it is the hole area percentage which controls the behavior of the valve mechanism (as opposed to the size or number of holes specifically). Thus, this parameter may be critical in maintaining healthy disc function.

One other parameter which would affect the valve behavior is that of the distribution of holes, i.e., the distance between the holes. While this was not analyzed using the image analysis package, observation by eye of Figures of Figures 2.3.1 - 2.3.9 revealed a fairly random distribution of the holes, with the distance between them in both the sheep samples and the human samples varying from one hole diameter to 5 or 6 hole diameters.

The large variation in the size of the holes observed in all samples and reflected in the wide and flat distribution in the histograms may be an indication of the constant remodeling of the bony endplate. The holes observed may be in a state of change in which new holes are opening up, smaller holes are getting bigger, and the larger ones are becoming smaller and eventually closing up. Such remodeling may be necessary in the maintenance of the cartilage endplate, since the fluid would not always be flowing through the same areas of cartilage.

2.3.4 *IN VIVO* PARAMETER ESTIMATION

From the median hole size and total number of holes found in the human bony endplate the permeability, flow rate and velocity at each hole can be roughly estimated (neglecting, for simplicity, the dependence of flow rate on the number of holes). If the average radius of the human lumbar intervertebral disc is approximately 2.0 cm and the average height

approximately 0.8 cm the volume is therefore 10 cm^3 [personal measurements of cadaver tissue]. The volume of the nucleus, if it constitutes approximately 20 % of the disc [personal measurements], is therefore 2.0 cm^3. If 80 % of the nucleus by weight in the young disc is water [5], and the disc loses 12 % of its water during daily loading [1] then

$V_{fluid\ loss}=V_{nucleus}\cdot$ fraction nucleus fluid content $\cdot$ fraction daily fluid loss $= 2.0 \cdot 0.80 \cdot 0.12 = 0.19\ cm^3$.

If a 16 hour period of loading is assumed, the average flow rate out of the disc during daily loading is

$Q_{total} = 0.19 \times 10^{-6}\ m^3/day \div 16\ hours/day \div 60\ min./hour \div 60\ sec./min. = 3.3 \times 10^{-12}\ m^3/s.$

If there are an average of approximately 6000 holes in the human endplate, the flow rate at each hole can be approximated by dividing the total flow rate by the number of holes, assuming all holes are the same size with an average radius of 40 μm:

$Q_{hole} = Q_{total} / 6000 = 3.3 \times 10^{-12} / 6000 = \mathbf{5.5 \times 10^{-16}\ m^3/s}$

and the velocity through each hole is

$u = Q_{hole}/A_{hole} = 5.5 \times 10^{-16} / (\pi\ (40 \times 10^{-6})^2\ ) = \mathbf{1.1 \times 10^{-7}\ m/s.}$

The permeability (K) can be found at each hole from a rearrangement of Darcy's Law

$Q = A \cdot K \cdot \Delta P / h \quad \Rightarrow \quad \mathbf{K = Q_{hole} / \Delta P \cdot h / A}$

where A is the cross-sectional area of cartilage above one hole through which the fluid flows, and neglecting the conical draining volume above the hole (i.e. assuming fluid drains through the entire cylindrical volume above the hole) A can be calculated from

$A = A_{endplate} / \text{no. of holes} = (\pi \cdot 0.025^2) / 6000 = 3.3 \times 10^{-7}\ m^2$

and, if h is the thickness of the cartilage layer which has been measured in dogs to be approximately 80 μm [4]

$h / A = 80 \times 10^{-6} / 3.3 \times 10^{-7} = 242\ m^{-1}.$

Assuming an average daily pressure (ΔP) in the disc of 10 bar [10]:

$K = Q_{hole} / \Delta P \cdot h / A = (5.5 \times 10^{-16} / 10 \times 10^{5}) \cdot 242 =$ **1.3 E-19 m^3s/kg**.

This value, while only a rough estimate, is approximately 1000 times less than the average permeability measured through the thickness of articular cartilage by Maroudas *et al.* [7] at zero applied strain (3.0×10^{-16} m^3s/kg). The low permeability value calculated here could indicate the possible effect of additional resistance provided by the cartilage endplate due to flow through the constriction holes in the bony endplate.

2.4 CONCLUSION

The surface of the bony endplate underlying the cartilage endplate in the disc of sheep and human vertebrae was studied using scanning electron microscopy. The existence of holes in the bony endplate was demonstrated, and the average size of holes, distribution of hole size, total hole area percentage of the surface area and total number of holes in the endplate could be estimated for both the sheep and human samples. A comparison of two human samples with two different degrees of cartilage calcification showed that the more calcified sample had a reduced average hole radius, a reduced hole area percentage of the total surface area, and a greater total number of holes. Too few samples were analyzed to make any statistically sound conclusions about the parameters or the effects of cartilage calcification, however, the SEM images and the image analysis data provide initial estimates and give an indication of the effects of calcification of the cartilage endplate on these parameters.

The measured parameters allowed an estimation of *in vivo* values such as fluid velocity and local permeability at the holes. The calculated estimate of permeability was found to be 1000 times less than the permeability of articular cartilage at zero applied strain measured by Maroudas *et al.* [7]. This additional resistance may be provided by the valve phenomenon in the disc.

The existence of the holes in the bony endplate, and particularly the cross-sectional images showing the channels from the surface to the trabeculae, provides evidence for a fluid flow path in the disc, and therefore provides evidence for the hypothesized valve mechanism. However, proof of this flow path and a demonstration of the valve mechanism in the body are still necessary and will be the subject of a future study. Further studies with younger human samples will be carried out and compared with the older osteoporotic specimens. The hole parameters measured will be used in a future finite element model of the *in vivo* situation in order to demonstrate the valve phenomenon in the body.

References

[1] Adams, M.A. and W.C. Hutton. The Effect of Posture on the Fluid Content of Lumbar Intervertebral Discs. *Spine,* **8**(6):p.665-71, 1983.

[2] Crock, H.V. and M. Goldwasser. Anatomic Studies of the Circulation in the Region of the Vertebral End-Plate in Adult Greyhound Dogs. *Spine,* **9**(7):p.702-6, 1984.

[3] Crock, H.V., M. Goldwasser and H. Yoshizawa. The Biology of the Intervertebral Disc. In *Vascular Anatomy Related to the Intervertebral Disc.* Ch.4, P. Ghosh, Florida, CRC Press, Inc. 1988, p.109-33.

[4] Holm, S., A. Maroudas, J.P.G. Urban, *et al.,* Nutrition of the Intervertebral Disc: Solute Transport and Metabolism. *Conn Tiss Res,* **8**:p.101-19, 1981.

[5] Hukins, D.W.L. The Biology of the Intervertebral Disc. In *Disc Structure and Function.* Ch.1, P. Ghosh, Florida, CRC Press, Inc. 1988, p.1-35.

[6] Hukins, D.W.L., J.R. Taylor, L.T. Twomey, et al., The Biology of the Intervertebral Disc. P. Ghosh, ed., Boca Raton, Florida, CRC Press, 1985.

[7] Maroudas, A. Permeability of Articular Cartilage. *Nature,* **219**:p.1260-1, 1968.

[8] Maroudas, A. The Joints and Synovial Fluid. In *Physical Chemistry of Articular Cartilage and the Intervertebral Disc.* Ch.6, L. Sokoloff, London, Academic Press, 1980, p.239-91.

[9] Maroudas, A., R. Stockwell, A. Nachemson, *et al.,* Factors involved in the nutrition of the human lumbar inttervertebral disc: cellularity and diffusion of glucose *in vitro. J. Anat.,* **120**(1):p.113-30, 1975.

[10] Nachemson, A. and G. Elfstroem. Intravital Dynamic Pressure Measurements in Lumbar Discs. Stockholm, The Almqvist and Wiksell Periodical Co. 1970, p.14.

[11] Nachemson, A., T. Lewin, A. Maroudas, *et al.,* In Vitro Diffusion of Dye Through the End-Plates and the Annulus Fibrosus of Human Lumbar Inter-vertebral Discs. *Acta Orthop Scand,* **41**:p.589-607, 1970.

[12] Ogata, K. and L.A. Whiteside. Nutritional Pathways of the Intervertebral Disc, An Experimental Study Using Hydrogen Washout Technique. *Spine,* **6**(3):p.211-6, 1981.

[13] Oki, S., Y. Matsuda, T. Itoh, *et al.,* Scanning Electron Microscopic Observations of the Vascular Structure of Vertebral End-Plates in Rabbits. *J Orthop Res,* **12**:p.447-9, 1994.

[14] Simon, B.R., J.S.S. Wu, M.W. Carlton, *et al.,* Structural Models for Human Spinal Motion Segments Based on a Poroelastic View of the Intervertebral Disc. *J Biomech Eng,* **107**:p.327-34, 1985.

[15] Taylor, J.R. and L.T. Twomey. The Biology of the Intervertebral Disc. In *The Development of the Human Intervertebral Disc.* Ch.2, P. Ghosh, Florida, CRC Press, Inc. 1988, p.39-82.

[16] Urban, J.P.G., S. Holm, A. Maroudas, *et al.,* Nutrition of the Intervertebral Disc, Effect of Fluid Flow on Solute Transport. *Clin Orthop and Rel Res,* **170**:p.296-302, 1982.

[17] Warwick, R. and Williams, P.L. ed. *Gray's Anatomy*, 35th edition. Longman Publishing Co., 1973.

CHAPTER
THREE

PHYSICAL MODEL

3.1 INTRODUCTION

A simple physical model was designed in order to demonstrate the valve phenomenon provided by the direction-dependent resistance of flow through a poroelastic solid with one underlying constriction hole. The properties of the materials used, as well as the geometry, were chosen to represent the *in vivo* valve in the intervertebral disc provided by the cartilage endplate and one underlying hole in the bony endplate. The tissue of the nucleus pulposus and annulus fibrosus were not included in the model. The presence of the nucleus certainly affects the flow behavior due to its osmotic swelling effects and its contribution to overall flow resistance, however, as discussed in Chapter 1, these factors probably do not play a significant role in the direction-dependent phenomenon. Furthermore, any contribution of these tissues was neglected in order to keep the model simple, but was taken into account in the analysis of the results.

In this model, the *in vivo* valve was represented by the flow of a viscous fluid through the "pores" of a deformable, elastic, porous, solid skeleton. In 1941 Biot [1] first formulated a linear theory for the deformation of a porous elastic solid saturated with a viscous fluid, assuming an isotropic medium. His theory was later extended to include anisotropic properties of the solid phase [8]. In this model the cartilage endplate was represented by a

poroelastic material with strain-dependent permeability and stiffness (see Figure 3.1.1). The results could then be used to propose that such a mechanism is necessary in the disc in order to maintain healthy disc hydration, and to use the model results to validate a corresponding finite element model.

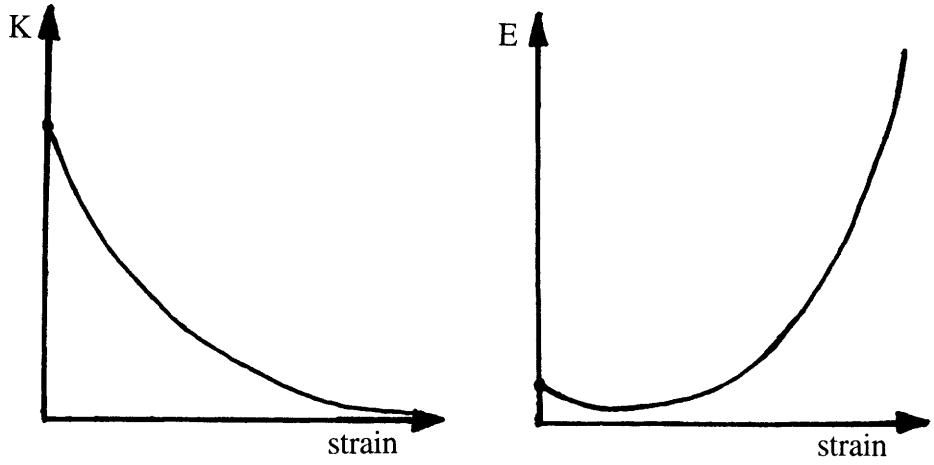

Figure 3.1.1 The general non-linear relationship between permeability (K) and compressive strain, and stiffness (E) and compressive strain.

3.2 MATERIALS AND METHODS

The cartilage endplate of the intervertebral disc was represented in the physical model by open-cell polyurethane foam. This material was chosen because it could be treated as a poroelastic solid, i.e., the flow could be defined by Darcy's Law [4] and the non-linear stress-strain behavior was representative of that of cartilage. The fluid medium was chosen according to its viscosity; glycerin was sufficiently viscous (Siegfried Handel AG, 98% glycerin, viscosity 0.7 $N \cdot s/m^2$) to allow accurate measurements of the flow rate by eye, and it was found that it had no structurally deteriorating effect on the polyurethane. The bony endplate was represented by an underlying aluminum plate, with one central constriction hole. The entire model was contained in a glass cylinder sealed with silicon rings against upper and lower plates. Only one underlying hole was modeled in order to simplify the analysis. The original experimental setup is shown in Figure 3.2.1.

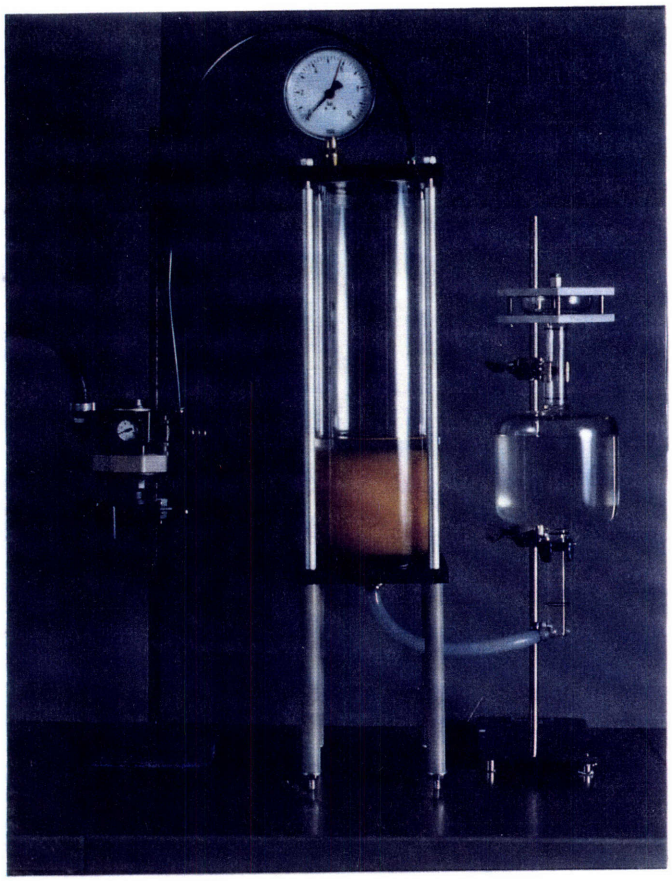

Figure 3.2.1 Original constriction flow experimental setup. The pressure regulator (far left) was used to control the pressure in the glass cylinder (center) for exudation flow. The fluid was forced through the foam and into the reservoir (far right). For imbibition flow, the reservoir was pressurized and the fluid was forced back into the cylinder.

3.2.1 PRESSURE GAGE CALIBRATION

Low pressure measurements in the range of 0.04 bar to 0.36 bar were made using a mercury manometer (KUNZ and Co.). Higher pressure measurements were made using a Bourdon gage (WIKA 0 - 10 bar range manometer). The Bourdon gage was first calibrated against the mercury manometer over a range of pressures from 0.2 to 0.4 bar and was found to have a constant offset. This offset was taken into account in all measurements and calculations.

3.2.2 VISCOSITY MEASUREMENT

When exposed to air, glycerin tends to absorb water, which decreases its viscosity. Samples of glycerin were taken from the experimental model after several days of testing in order to measure and compare the viscosity to that of fresh, unexposed glycerin using a viscometer

(SCHOTT Ubbelohde Viscometer, Type CT42, Capillary No. IV). The difference between the two values was found to be negligible and the viscosity of fresh glycerin was assumed in all calculations.

3.2.3 MATERIAL PROPERTY MEASUREMENT

The variation of permeability with strain and stiffness with strain were determined for the model material.

- **Permeability vs. Strain**

The experimental setup for the permeability test is shown in Figure 3.2.2. In order to determine the absolute permeability of the given volume of polyethylene, i.e. without a constriction hole, a porous support and loading platen were designed which allowed unconstricted flow of the glycerin through the foam with negligible resistance while applying various confined compressive strains. The foam was supported on each end by an open wire mesh structure of the type used for fan ventilation inlet covers. This mesh was then supported at both ends by the draining plates. Both the wire mesh plates and the draining plates and their assembly are shown in Figure 3.2.3. One of the draining plates was attached to the Instron loading piston and was used to control the applied compressive strain.

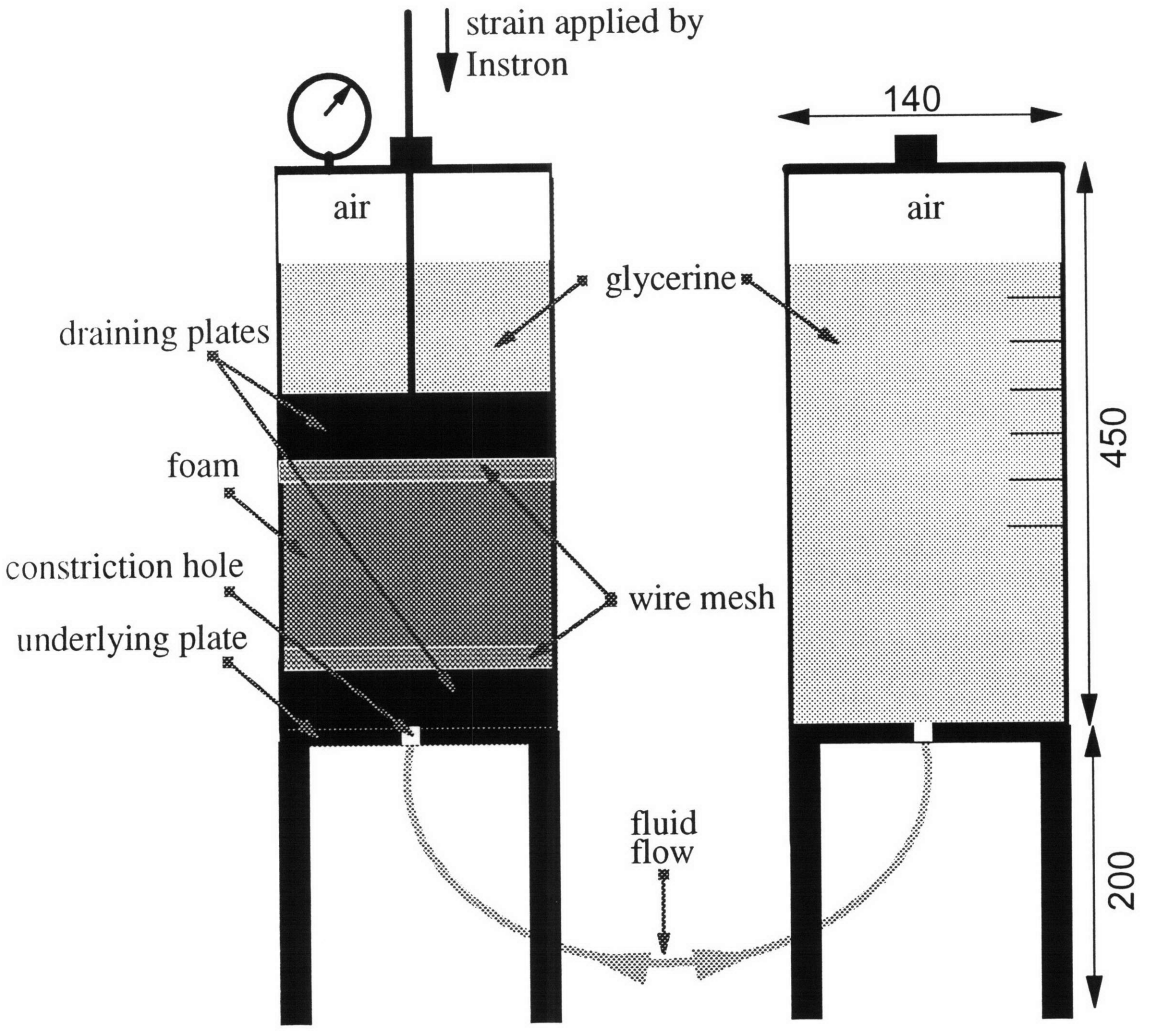

Figure 3.2.2 Cross-sectional schematic diagram of permeability test setup. All dimensions in mm.

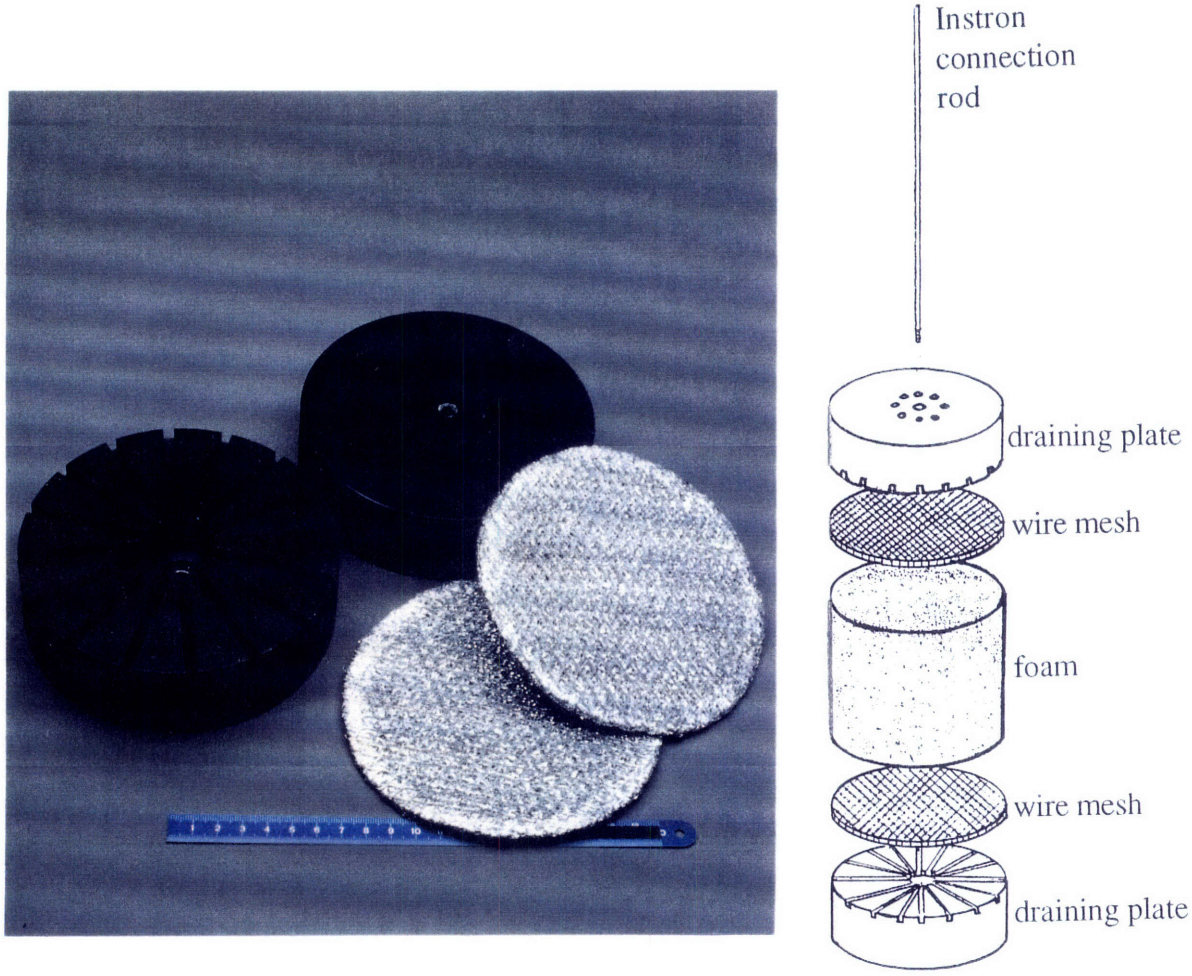

Figure 3.2.3 Wire mesh plates and draining plates used in the permeability test. The complete experimental setup can be seen in Figure 3.2.2.

When filling the cylinder with glycerin and saturating the foam, air became trapped in the pores of the foam. Thus, after filling, a vacuum was pulled through the top of the cylinder until the flow of bubbles out of the foam ceased.

Compressive strains were applied to the saturated foam using the Instron mechanical testing machine (Model 4302). It was initially planned to measure the permeability at strains from 0% to 95%, however, it was found that at lower applied strains (up to 30%) the drag forces on the matrix due to the flow resulted in compressive strains which were higher than those applied with the platen. In addition, the foam became too stiff at a compressive strain of 85% to allow any further loading, for fear of damaging the foam or glass cylinder. Thus, permeability was measured at compressive strains of 30% to 85% in increments of 5%. Flow rates were measured at each strain under applied pressures of 0.2 to 2.0 bar in increments of

0.2 bar (up to 2.0 bar where possible when the drag forces did not become too high, resulting in matrix compression). Any additional strain due to the fluid drag on the matrix was measured and accounted for in the net strain observed at the upper surface of the foam (i.e. the displacement of the foam from the upper loading platen). The constant resistance of the wire mesh, draining plates and tubing ($\mathbf{R_{sys}}$, the correction factor for the resistance of the entire system without foam) was also measured at pressures of 0.5 to 2.0 bar. This correction factor was applied to all resistance measurements. An attempt was made to use water in place of glycerin in order to determine the permeability at strains below 30%. However, the system resistance (R_{sys}) was found to be approximately 95% of the total resistances measured and the values were therefore inaccurate.

Once flow equilibrium had been attained after the application of a step in strain (when the applied force reached equilibrium), the cylinder was pressurized. Steady state flow rates were measured by eye and stop-watch (CASIO Trisports hand-held stop-watch, 0.1 sec resolution), initially with the use of a "backward hour-glass" reservoir as shown in the photograph of Figure 3.2.1. This reservoir was designed to allow more accurate measurements of volume flow in the upper and lower graduated cylinders, while at the same time allowing a sufficient total volume of fluid flow to ensure flow rate measurements were made at steady state. It was discovered, however, that the total volume flux was too low (approximately 1.5 L) and that steady state was not in fact being reached. Thus, the reservoir was changed to a simple cylinder as in the final configuration shown in Figure 3.2.2 which allowed a total volume flux of 4.5 L. Volume flow rate was determined by timing a 5 mm vertical displacement of the fluid surface at the end of the imbibition or exudation cycle, corresponding to a fluid volume of 77 ml. Measurements were taken for flow out only, although a few flow measurements both in and out were initially taken and compared to ensure symmetry of the system. After each flow measurement an attempt was made, by forcing the fluid in and out several times, to bring the foam back into complete contact with the upper and lower platens in order to return it to its equilibrium position.

From the measured flow rate, Q, and applied pressure P the overall permeability could be determined from the simplified Darcy's Law:

$$K = \frac{Q}{\Delta P} \tag{3.1}$$

From this value the "absolute permeability", $\mathbf{K_\infty}$ [4], a material parameter of a poroelastic solid with a given porosity and pore size, can be calculated from Darcy's Law:

$$u = -\frac{K_\infty}{\mu} \cdot \frac{dp}{dx} \tag{3.2}$$

and if the velocity gradient is assumed constant in the axial direction (and therefore the pressure gradient) such that $\frac{dp}{dx} = \frac{\Delta P}{h}$, Darcy's Law can be rearranged to give:

$$\boxed{K_\infty = K \cdot \frac{h}{A} \cdot \frac{\mu}{\rho}} \tag{3.3}$$

where h ≡ height of the foam cylinder; A≡ area of foam cylinder; μ and ρ ≡ viscosity and density of the fluid respectively.

- **Stiffness vs. Strain**

The variation in the uniaxial confined stiffness vs. applied strain was determined for the saturated foam from a compression test performed on the Instron mechanical testing machine. Displacement was applied in steps of 5% strain from 5 to 85 % and the force at equilibrium (when fluid flow had ceased) was recorded at each strain. The foam was supported at the bottom by a rigid impermeable plate, and the load was applied with the same mesh and draining plate combination as that used in the permeability test. From the equilibrium force vs. applied displacement the stress vs. strain curve could be determined as well as the variation in equilibrium stiffness with strain.

3.2.4 CONSTRICTION FLOW EXPERIMENT

This experiment was the main objective of the physical model. The aim was to measure the absolute exudation and imbibition resistances of the constriction flow model as well as to demonstrate the direction-dependent resistance of the constriction flow valve (i.e. the ratio of exudation resistance to imbibition resistance) and to measure the change in these parameters with increasing applied pressure.

Flow rates through the constriction hole into and out of the foam were measured at pressures ranging from 0.03 bar to 2.5 bar. Three measurements were taken at each pressure for both imbibition and exudation. The flow rate was measured using the large cylinder reservoir as shown in Figure 3.2.4. As in the permeability experiment the flow rates were measured by eye and stop-watch for a 5 mm displacement of the fluid surface corresponding to a volume

were corrected by this offset value (this offset was also taken into account in the permeability test).

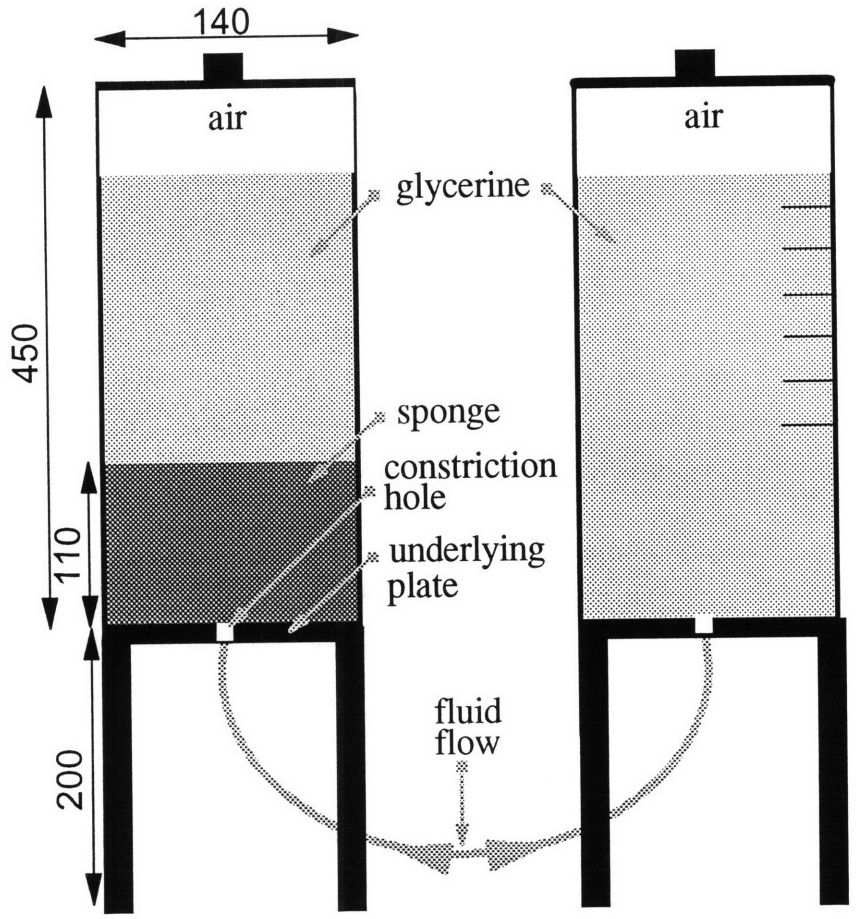

Figure 3.2.4 Constriction flow experimental setup.

Pressures ranging from 0.03 to 0.35 bar were measured using a mercury manometer and controlled using a low pressure regulator (FESTO, Type LRN -1/4-F-B, 0 - 0.7 bar range). Pressures ranging from 0.35 to 2.5 bar were measured using a Bourdon manometer and controlled using a high pressure regulator (CKD R 4000, range 0.5 - 8.5 bar). The pressures measured with this gage were corrected according to the offset found in the gage calibration test. Whenever the cylinder was refilled with glycerin it was evacuated to remove trapped air from the foam. The system resistance ($\mathbf{R_{sys}}$, the total resistance of the system without the foam) was measured at varying pressures from 0.5 to 2.0 bar and all resistance measurements were corrected by this value.

3.3 RESULTS

3.3.1 PRESSURE GAGE CALIBRATION AND CORRECTION FACTORS

Table 3.3.1 lists the correction factors found for both the mercury manometer and the high pressure gage.

	Pressure Head Offset (bar)	Gage Calibration Offset (bar)	**Total Correction Factor (bar)**
Mercury Manometer	-0.0084	------	-0.0084
High Pressure Gage	-0.0084	+0.05	+0.0416

Table 3.3.1 Pressure Gage Calibration and Correction Factors

3.3.2 VISCOSITY MEASUREMENT

The average of twelve measurements of the dynamic viscosity of fresh, unexposed glycerin was found to be 565.10 E-06 m^2/s at 25°C which is equal to a viscosity of 0.712 kg/s·m at the measured density of 1263 kg/m^3. This was compared to the viscosity of the experimental sample, which had been exposed to the air for several days, with a value of 550.49 E-06 m^2/s or 0.694 kg/s·m; a decrease of only approximately 2.5 % due to atmospheric water absorption. The viscosity was therefore assumed to be constant at an average value of 0.70 kg/s·m, although some small amount of water absorption over time may have caused small fluctuations in this value.

3.3.3 MATERIAL PROPERTY MEASUREMENT

- **Permeability vs. Strain**

The curve of permeability (K) vs. applied strain obtained from the unconstricted permeability test is shown in Figure 3.3.1. The value of K was calculated from the simplified Darcy's Law:

$$K = \frac{Q}{\Delta P} \cdot \frac{h}{A} \qquad (3.4)$$

This value of permeability is most commonly used when discussing the permeability of cartilage (as opposed to the absolute permeability calculated in Equation 3.3). It is independent of the applied pressure, however, some internal local consolidation of the matrix caused a slight decrease in permeability with increasing applied pressure. This problem has also been encountered when attempting to measure the permeability of cartilage [5].

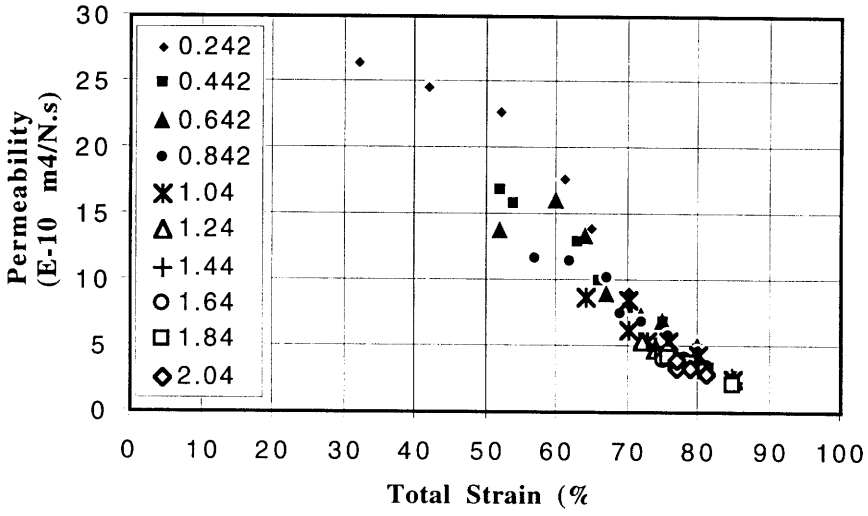

Figure 3.3.1 Change in permeability with strain. Legend is applied pressure (bar).

- **Stiffness vs. Strain**

The compressive stress-strain curve determined from the equilibrium force-displacement test can be seen in Figure 3.3.2. The slope of this curve is the uniaxial compressive stiffness **L.** An initial stiffness was observed at small strains after which the curve reached a plateau which continued up to a strain of approximately 70%. At strains beyond 70% the stiffness rose steeply.

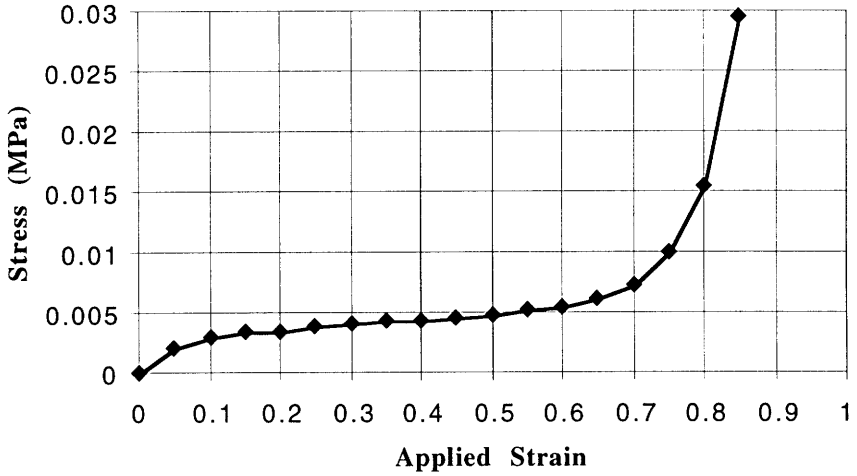

Figure 3.3.2 Stress vs. strain of model material

3.3.4 CONSTRICTION FLOW EXPERIMENT

In Figure 3.3.3 the variation in both R_{im} and R_{ex} are plotted vs. applied pressure ($\mathbf{P_{app}}$), and in Figure 3.3.4 R_{im} is plotted vs. R_{ex} to demonstrate the behavior of this ratio with increasing applied pressure. The raw data is listed in the Appendix in Table A.1.1. Here, the values of resistance were calculated from the simplified Darcy's Law as in Equation (3.1), i.e.,

$$R = \frac{1}{K} = \frac{\Delta P}{Q}. \tag{3.5}$$

At the lowest applied pressure of 0.03 bar the values of R_{im} and R_{ex} were observed to be approximately the same, while at the maximum applied pressure of 2.5 bar the ratio reached a value of approximately 20. While at the maximum applied pressure the imbibition resistance appeared to be approaching a low asymptotic value, the exudation resistance was rising steadily and it would be reasonable to assume that it would continue to rise at applied pressures well beyond the maximum applied in this experiment.

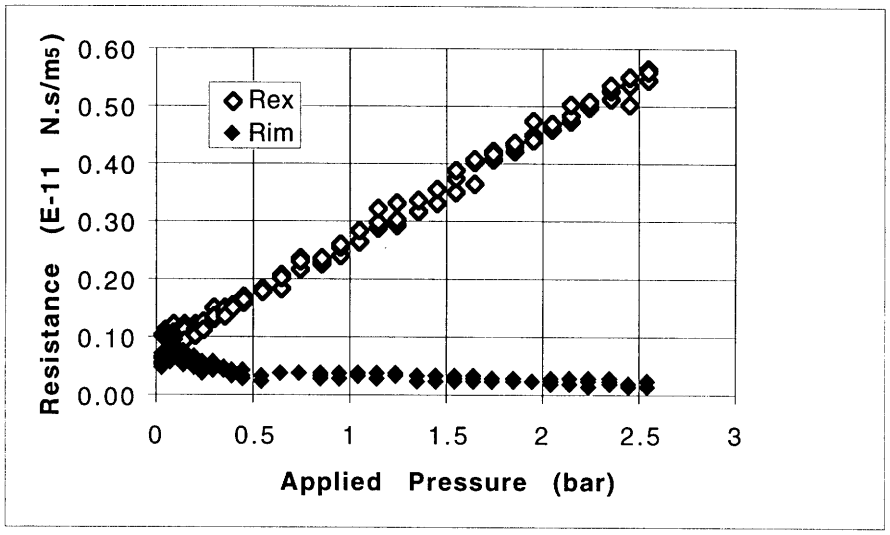

Figure 3.3.3 Change in the exudation resistance (R_{ex}) and the imbibition resistance (R_{ex}) of the constriction flow model with applied pressure.

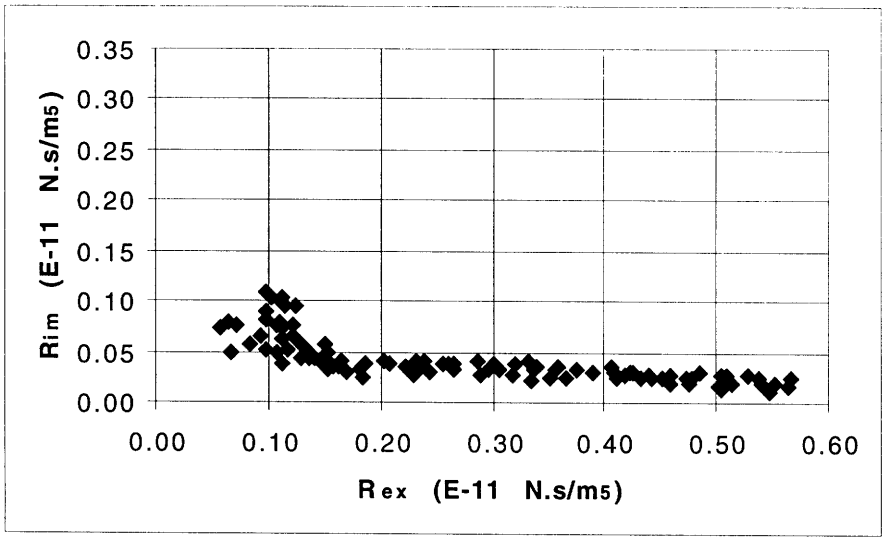

Figure 3.3.4 Scatter plot of imbibition resistance (R_{im}) vs. exudation resistance (R_{ex}) with increasing applied pressure, from 0.03 bar to 2.5 bar.

3.4 DISCUSSION

3.4.1 MATERIAL PROPERTIES

• Permeability vs. Strain

The variation of permeability with strain of the polyurethane is comparable to the behavior of the "intrinsic" permeability determined by Lai and Mow [5] for articular cartilage. They measured the permeability of articular cartilage vs. strain at various applied pressures and found that the matrix was consolidating due to fluid drag forces. Thus, the actual strain in the cartilage was higher than the applied strain. Furthermore, these drag-induced strains changed with depth in the cartilage layer due to its non-uniform permeability. They defined the intrinsic permeability function as the a function for the limiting case at which the applied pressure tends to zero, i.e. where there are no strains in the matrix due to drag forces and the actual strain is the applied uniform strain. Such drag-induced strains in our physical model dominated at applied strains of less than 30%, and we could therefore determine the permeability function only for applied strains greater than 30%. However, since the permeability of the polyurethane foam could be assumed uniform (due to its uniform structure), and given the similar behavior of the data obtained experimentally and the data for the intrinsic permeability of articular cartilage found by Lai and Mow (shown in Figure 3.4.1), our curve could be quite reasonably extrapolated to zero strain. This extrapolated curve was used in the finite element model.

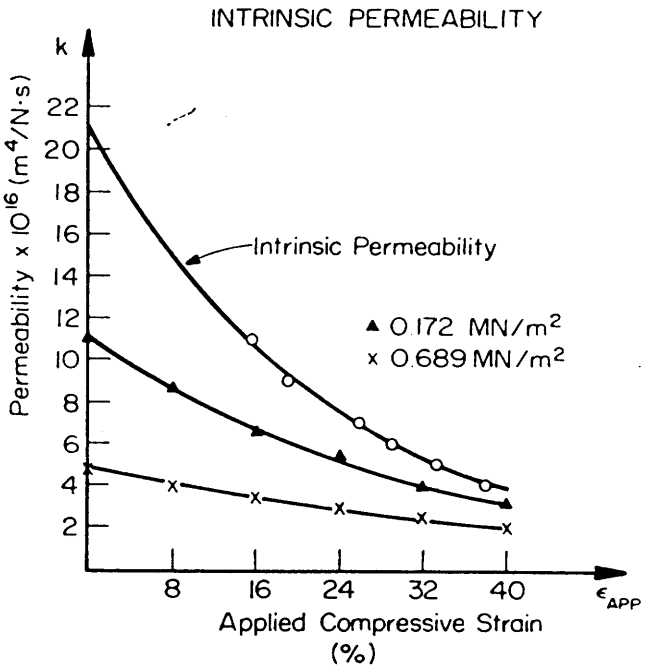

Figure 3.4.1 The variation in permeability of articular cartilage with compressive strain at two applied pressures. The "intrinsic permeability" is found for the limiting case of $P_{applied} \rightarrow 0$ (Lai and Mow [5]).

While the permeability of a poroelastic solid, as for cartilage, is independent of pressure, some decrease in the polyurethane permeability with increasing applied pressure was found experimentally, even when no drag-induced compression could be observed at the top surface of the foam (i.e. when the foam remained in contact with the upper platen). This could be attributed to some internal, local, drag-induced consolidation of the foam as in the case of cartilage found by Lai and Mow. However, since the permeability of the poroelastic foam is approximately uniform, this local consolidation effect was assumed to be small. Therefore the average permeability curve found experimentally was taken as that of the "intrinsic" permeability, and any non-negligible drag-induced strain in the foam was taken into account through observation of the surface displacement (i.e. when the foam separated from the upper platen).

- **Stiffness vs. Strain**

The compressive stress-strain curve of the saturated poroelastic foam followed a similar pattern to the stress-strain behavior of articular cartilage. In the case of a foam, the initial stiffness measured is that of the pore walls as they bend under compressive load. The subsequent plateau in the curve occurs as the pore walls buckle and the pores collapse, and

finally the material consolidates and the stiffness rises steeply [4]. This behavior is representative of that of articular cartilage in which no clearly defined, repeating-unit pores exist, but in which the behavior is determined by the collagen fibrils. These fibrils resist the load initially due to their intrinsic stiffness, then buckle, and finally the matrix consolidation results in a steep rise in stiffness.

- **Combined Effect of Permeability and Stiffness**

The combined effect of the permeability and stiffness of the endplate cartilage and their dependence on strain are critical factors in the healthy function of the intervertebral disc valve. These parameters are related by

$$D = L \cdot K \tag{3.6}$$

where D ≡ diffusion coefficient, L ≡ uniaxial compressive stiffness and K ≡ matrix permeability. The diffusion coefficient can be found from the fundamental time constant of cartilage since

$$D = \frac{4h^2}{\pi^2 \tau} \tag{3.7}$$

where h ≡ height or thickness of the solid and τ ≡ the fundamental time constant. Both L and K depend non-linearly on strain, as observed in the model. Therefore, it was hypothesized that the number and size of the constriction holes would be critical valve parameters since they would determine the local strain of the matrix at the hole. These parameters could be altered in the intervertebral discs by calcification of the cartilage endplate or by some other disturbance which would result in blockage of the bony endplate holes.

Assuming that the draining areas of the bony endplate holes in the nucleus overlap, a **decrease in the number of holes** would result in an increase in the draining area of each hole, as shown in Figure 3.4.2. This draining area is probably limited and at some minimum number of holes (some limiting distance between the holes) the draining areas would no longer overlap (as in the bottom diagram of Figure 3.4.2). Any further decrease in the number of holes would then have no effect on the flow behavior. However, we hypothesize that before this minimum is reached, an increase in the draining area of each hole would result in an increase in the local matrix consolidation, and a resulting increase in the local

exudation resistance. The ratio of exudation resistance to imbibition resistance was also expected to rise with a decrease in the number of holes.

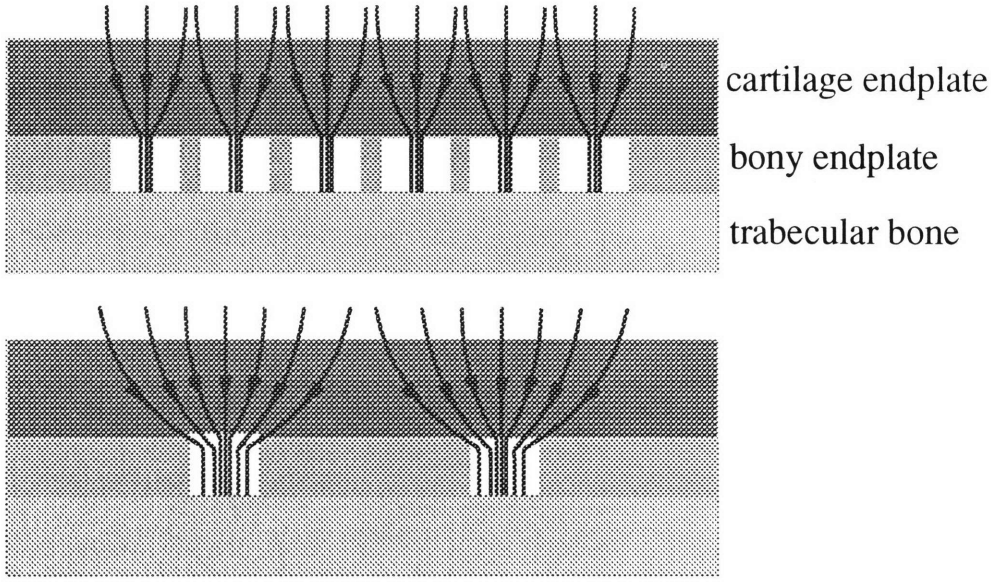

Figure 3.4.2 Given that the draining areas of the constriction holes overlap to begin with, a decrease in the number of holes would result in an increase in the draining area of each hole.

Calcification of the cartilage endplate would result not only in a decrease in the number of holes, but would first result in a **decrease in the size of the holes** as they gradually became covered. Regardless of the initial draining area overlap, a decrease in hole diameter would mean that the fluid would be forced through smaller holes resulting in an increase in the exudation resistance as well as the resistance ratio, as in the case of a decrease in the number of holes.

These effects were demonstrated with the finite element model in Chapter 4 (i.e. the change in absolute resistances and the resistance ratio with a change in the size of the holes as well as the number of holes). However, from the results of the physical model it was hypothesized that *both a decrease in size and a decrease in number* of bony endplate holes would result in an increase in exudation resistance and an increase in the ratio of exudation resistance to imbibition resistance.

The normal daily function of the disc valve requires a specific balance between the matrix stiffness and permeability, which depend on the properties of the cartilage itself (L and K at zero strain and their change with strain) and on the size and number of underlying

constriction holes. During exudation of fluid from the disc, if the stiffness of the cartilage endplate and/or its permeability are too high, the time constant will be low (i.e. a fast response to step load) and the diffusion coefficient will be too high resulting in a high loss of fluid. If the stiffness and/or the permeability are too low, the cartilage will collapse under the fluid drag forces and excessive consolidation of the matrix will disrupt the normal fluid flow. In this case the time constant would be high since fluid would be lost very slowly from the disc as it continued to creep under load. Thus, in the body there exists a healthy range of the diffusion coefficient (D) for normal daily disc function. This value could be disrupted by various changes in the disc structures, in particular by the calcification of the cartilage endplate which would result eventually in a decrease in the total number of constriction holes. In addition, tissue properties could be changed by disc degeneration, disc dehydration, or other disc pathologies.

3.4.2 CONSTRICTION FLOW

The most critical valve parameter to be determined for the physical model was the ratio of exudation resistance to imbibition resistance and its change with applied pressure. The model data shows that at low pressures (0.03 - 0.05 bar) R_{im} and R_{ex} were approximately equal, since the velocity through the hole was so low that any increase during exudation and consequent increase in strain at the hole were negligible. However, as the applied pressure and resulting velocity increased, R_{ex} rose while R_{im} fell such that at an applied pressure of 2.5 bar the ratio of $\frac{Rex}{Rim}$ had reached a value of approximately 20.

These results demonstrate that the mechanical valve, which could be provided in the disc by the cartilage endplate and holes in the underlying cortical bone, supplies an fast response to loading, i.e. the resistance is high initially as well as throughout the entire period of loading. This makes it a more efficient valve than one proposed by Urban *et al.* [11] in which the permeability of the disc tissues decrease with decreasing water content. With such a physiological valve the total fluid loss during loading would be higher since the resistance is initially low and increases only as fluid is lost from the disc. Furthermore, the resistance of the mechanical valve depends on the pressure in the disc. At higher pressures the exudation resistance is higher, and in this way the valve compensates for higher loads on the spine, thus ensuring a limited fluid loss even in extreme loading cases.

A maximum value of R_{ex} was never reached at pressures applied in the model, rather it appeared that it would continue to rise steeply at higher applied pressures. R_{im}, however,

was observed to approach a minimum asymptotic value which indicated that some maximum tensile strain of the matrix was being reached. Thus, if such a maximum strain exists in the cartilage endplate it is likely that beyond such a point the compression of the matrix during exudation would dominate the valve behavior. A decrease in the number of holes in the bony endplate beyond this point would therefore increase R_{ex} but may have a limited effect on R_{im}.

3.4.3 SOURCES OF ERROR

General sources of error arose from the pressure readings due to the resolution of the scale on the gages and fluctuations of the source pressure with time. Sources of error also arose from the volume flow measurement due to the reduced accuracy of the large cylinder reservoir readings, reaction time with the stopwatch and the inaccuracy due to measurements by eye and the presence of the meniscus on the fluid surface. An attempt was always made to return the foam to its equilibrium position (zero strain) before any subsequent measurements were made, however, any local inconsistencies in strain within the foam could not be observed and may have contributed to measurement error.

The offset correction ($\mathbf{R_{sys}}$) found for the permeability test setup without the foam which was applied to all measured values contributed significantly to inaccuracy, particularly at low applied strains. At 85% applied strain the offset made up approximately 30% of the total resistance measured, while at 30% applied strain it made up approximately 95% of the total measured value. Another contribution to measurement error in the permeability test was the difficulty in returning the foam back to an equilibrium position before subsequent measurements were taken. Due to the friction between the foam and the glass wall of the cylinder the foam would often stick in a slightly over-extended or under-extended position even after several cycles of forcing fluid back and forth through the foam. This problem indicated that local strains may have existed in the foam which could not be observed from at the top surface. However, any effects due to these local strains were assumed negligible.

Often it was found that over the course of a day's experiments the flow rate at any given pressure would increase. It seems unlikely that the foam would remain in an expanded state after an imbibition run under the drag forces of a subsequent exudation run. Perhaps this phenomenon was due to some local expansion at the hole or to local air bubbles being gradually pushed aside with each run. Another possibility is that variations in the room temperature increased or decreased the viscosity of the glycerin slightly.

3.5 CONCLUSION

The direction dependent resistance of constriction flow through a poroelastic solid was successfully demonstrated by the physical model. Previous studies have indicated that a direction-dependent phenomenon must exist in the intervertebral disc in order to maintain healthy function and hydration. Since cartilage can be modeled as a poroelastic material and assuming that fluid flows into and out of the disc through the endplate cartilage and through the underlying holes in the bony endplate it is hypothesized that such a mechanical valve mechanism as that demonstrated by the physical model also exists in the disc. Some question remains concerning the path of fluid flow in the disc. No quantitative studies have been published to demonstrate the dominant flow path, although some have found evidence that the main path is through the endplate [3]. Future *in vitro* and *in vivo* experiments will be necessary to determine the dominant route and to prove that the valve mechanism exists in the body.

The change in flow behavior with the size and number of holes could not be demonstrated with this model, however, it was hypothesized that a decrease in the size or number of holes would increase the draining area of each hole, resulting in a rise in exudation resistance and an increase in the resistance ratio (exudation resistance to imbibition resistance). The distribution of holes must also be important, since the draining area of any given hole would depend on its proximity to other holes. These effects were demonstrated using a finite element model in Chapter 4, and the effects of such changes *in vivo* will be demonstrated with a future finite element model as well as with *in vitro* experiments.

The physical model did not take into account the osmotic swelling effects of the disc tissue nor the change in hydraulic permeability of the nucleus with disc fluid content, both of which have been suggested to contribute to the direction-dependent effects of the flow in the disc [9-11]. However, these mechanisms do not provide any overall direction-dependent effects, and some additional mechanism appears to be necessary. This model has demonstrated that the necessary mechanism could be provided by the structures which are known to exist in the disc, and the aim of the physical model was to demonstrate the valve phenomenon provided by the cartilage endplate and bony endplate alone. The finite element model presented in Chapter 4 represents the physical model and therefore also neglected osmotic swelling and changes in hydraulic permeability. However, future FE models of the *in vivo* situation could

include such effects in order to determine more completely the behavior of the disc under daily loading.

References

[1] Biot, M.A. General Theory of Three Dimensional Consolidation. *J Appl Phys,* **12**:p.155-64, 1941.

[2] Broberg, K.B. Slow Deformation of Intervertebral Discs. *J Biomech,* **26**(4/5):p.501-12, 1993.

[3] Cassidy, J.J., A. Hiltner and E. Baer. The response of the hierarchical structure of the intervertebral disc to uniaxial compression. *J Mat Med,* **1**:p.69-80, 1990.

[4] Gibson, L.J. and M.F. Ashby. Cellular Solids; Structure and Properties. New York, Pergamon Press, 1988,

[5] Lai, W.M. and V.C. Mow. Drag-Induced Compression of Articular Cartilage During a Permeation Experiment. *Biorheology,* **17**:p.111-23, 1980.

[6] Mak, A.F. The Apparent Viscoelastic Behavior of Articular Cartilage - The Contributions From the Intrinsic Matrix Viscoelasticity and Interstitial Fluid Flows. *J Biomech Eng,* **108**:p.123-30, 1986.

[7] Mow, V.C., S.C. Kuei, W.M. Lai, *et al.,* Biphasic Creep and Stress Relaxation of Articular Cartilage in Compression: Theory and Experiments. *J Biomech Eng,* **102**:p.73-84, 1980.

[8] Ogata, K. and L.A. Whiteside. Nutritional Pathways of the Intervertebral Disc, An Experimental Study Using Hydrogen Washout Technique. *Spine,* **6**(3):p.211-6, 1981.

[9] Urban, J.P.G. Factors Influencing the Fluid Content of Intervertebral Discs. *Adv Microcirc,* **13**:p.160-70, 1987.

[10] Urban, J.P.G. and A. Maroudas. Swelling of the Intervertebral Disc *In Vitro. Conn Tiss Res,* **9**:p.1-10, 1981.

[11] Urban, J.P.G. and J.F. McMullin. Swelling Pressure of the Lumbar Intervertebral Discs: Influence of Age, Spinal Level, Composition and Degeneration. *Spine,* **13**(2):p.179-87, 1988.

CHAPTER
FOUR

FINITE ELEMENT MODEL

4.1 INTRODUCTION

Several studies have used finite element analysis to model the behavior of the entire spinal motion segment under various loading conditions [7,18]. Many of these studies model the nucleus of the intervertebral disc as an enclosed "fluid filled" space with a given bulk modulus [17,18,22] or as an incompressible solid [4,6,8] and do not model the fluid flow into and out of the disc. One study by Shirazi-Adl [17] modeled the effects of changes in the fluid content of the disc on the biomechanics of the spinal motion segment but flow into and out of the disc was not modeled. Hakim and King [7] modeled the disc with boundary elements (one degree-of-freedom elements acting as springs at the nodes with given axial, shear and torsional resistances), while Mizrahi *et al.* [13] modeled only the vertebral body in order to study the effects of osteoporosis on the stresses in the bone under various loading conditions. Some studies include geometric and material non-linearities while others assume linear properties. A study by Kulak *et al.* [8] incorporated a non-linear elastic constitutive law for the annulus fibrosis. These studies provide useful information about the instantaneous stresses in motion segments under various physiological loads, however, in order to study the long-term creep effects of daily loading and to determine the flow behavior under these loads, fluid flow must be incorporated into the model.

Other finite element models of the spinal motion segment are those which incorporate fluid flow into and out of the disc. Simon *et al.* [21] studied the fluid flow patterns out of the disc during creep loading in rhesus spinal motion segments. They modeled the intervertebral disc, endplate and vertebral cancellous bone with poroelastic elements, allowed flow through both the cartilage endplate and the annulus, and assigned them the same permeability. The underlying bony endplate was modeled as a stiff, porous structure. The aim of the study was to compare the flow behavior of an "open top" model, in order to represent the usual *in vitro* situation in which the motion segment is excised through the vertebral bodies, and a "closed top" model, in order to represent the *in vivo* situation. The material properties were found by adjusting the open top model until the results matched experimental data. These material properties were then applied to the closed top model and the results compared.

The results of this study showed very different load response behavior during creep in the open top vs. the closed top model. Transient effects were reduced dramatically in the closed top model, in which displacement equilibrium was reached within minutes, as opposed to the open top model in which equilibrium was not reached within the two hour simulation period. However, it is most probable that *in vivo*, fluid flow equilibrium is never reached during the course of the day [23,24]. Thus, it would seem that the closed top model, with a totally impervious vertebral cortical shell is too extreme and does not represent the *in vivo* situation well. Most *in vitro* tests are performed with the trabeculae of the cancellous bone of the vertebrae packed with marrow and with the excised ends pressed against loading platens. Such an experimental set up should therefore give a reasonable representation of the *in vivo* situation, and indeed, such *in vitro* creep studies have shown that under creep for up to four hours equilibrium is never reached [1].

The closed top model resulted in high pressure in the poroelastic cancellous bone of the vertebrae, which caused *imbibition* of fluid into the disc across the cartilage endplates during compressive creep loading at $t \rightarrow \infty$ while fluid was exuded out through the annulus. In the *in vivo* situation the existence of the vascular foramina in the cortical shell may relieve the pressure in the bone, thus resulting in a more likely situation of *exudation* of fluid across the endplates during compressive creep driven by the intradiscal pressure.

In the open top finite element model, fluid was observed to flow out of the disc through the cartilage endplates but *into* the disc through the *annulus* during creep at $t \rightarrow \infty$. Consideration of the pressure gradient during compressive loading indicates that, given that the pressure outside the disc is effectively zero and that a "hydrostatic" pressure or fluid stress exists in

the disc [12,15,16], fluid would certainly be driven *out* through the annulus, assuming that it is permeable. However, as stated in this study, the actual response most likely lies somewhere between the open and closed top cases.

In another study Simon *et al.* [20] modeled the human spinal motion segment based on a linear, isotropic, poroelastic material law for the intervertebral disc (IVD) and considered the cartilaginous endplate as part of the IVD. Again values of stiffness and permeability for the disc were adjusted until the results of the creep response matched the experimental data. It is important to note that in this model, the fluid was found to flow *out of the disc through both the annulus and the cartilage endplate* under creep loading at $t \rightarrow \infty$. This is the most likely *in vivo* response as argued above given the pressure gradients across the annulus and cartilage endplates due to the hydrostatic pressure in the disc. Furthermore, the flow patterns found in this study are similar to the flow behavior suggested by Adams and Hutton in an *in vitro* creep study [1].

No explanation is offered for the differences in flow patterns in the rhesus model and the human model developed by Simon *et al.* [20,21]. However, in the human study the vertebral body was modeled as an elastic material while the rhesus study modeled the cancellous bone of the vertebrae as a poroelastic material. The use of poroelastic elements for the vertebrae in the rhesus model could account for the flow into the disc across the cartilage endplates during compressive creep due to pressurization of the pores of the vertebral elements. Whether the human model was "open top" or "closed top" is not discussed. However, flow was allowed from the nucleus to the vertebral bodies through the cartilage endplates. The permeability of the disc material (disc, annulus and endplate) was slightly higher in the human model and flow was not permitted through the region of the cartilage endplate underlying the annulus, all of which may have contributed to the differing flow patterns.

A study by Matyjewski [11] provides a FE model of the SMS which combines poroelastic materials with a geometrically non-linear analysis. The tissue of the disc was modeled as a poroelastic material, while elastic elements were used for the bone. Anisotropic material properties were used for the annulus fibrosus. The stress profile of the model results match closely with the *in vitro* results of McNally and Adams [12]. The fluid flow results were not reported in this publication.

More recent finite element studies of the creep behavior of SMS take into account the swelling effects of the proteoglycan in the disc tissue. In an initial study, Simon and Gaballa [19] investigated a linear, uncoupled, small strain formulation in order to determine the role

which tissue swelling plays in the mechanical behavior of the rhesus SMS. A poroelastic-ionic finite element model was used in which both the disc and cancellous bone were modeled as poroelastic solids. Flow was permitted through both the endplates and the annulus of the disc. A uniform NaCl concentration level was assumed in the entire IVD and swelling effects were compared for two cases: "free swelling" in which the IVD was subjected to swelling loads with a uniform decrease in NaCl concentration and no external loads, and a "confined swelling" case in which the SMS displacement was confined in the axial direction such that swelling resulted in stress and pressure build-up in the disc.

It is suggested in this study that the actual *in vivo* case would lie somewhere between the "free" and "confined" swelling extremes; perhaps this response could be determined by simply applying known resting muscles forces to the SMS and observing the resulting stress and pressure in the disc during swelling. For the constrained swelling model the maximum decrease in NaCl concentration (assumed equilibrium point) resulted in a nuclear pressure of 0.6 bar, which is comparable to the measured osmotic resting pressure in the disc [10]. It was stated in the study that the resulting stress state in the disc was considerably different from that found in other studies with external compressive loads alone. It was therefore concluded that ionic swelling effects play a large role in the mechanical behavior of the SMS and that their inclusion in FE models may significantly affect the results.

Laible *et al.* [9] incorporated swelling effects into a 3D poroelastic model of a SMS with linear, isotropic material laws. The vertebrae were very simply modeled and acted as rigid bodies. Flow was allowed out of the nucleus through the cartilage endplates as in the previously discussed "open top" model. The effects of swelling were incorporated through a modification of the constitutive law and the initial stresses in the disc. The number of fixed charges was assumed constant and the distribution of ions in the disc assumed uniform. In this way, the osmotic pressure in the disc depended only on the initial state and on the change in water content during loading (i.e. the change in fixed charge density). A non-linear relationship between the swelling pressure and the change in water content was defined. The model was used to simulate a five hour swelling / five hour creep loading cycle in the geometrically simplified SMS. The results showed that the fluid stress and solid stress together balance the applied load, but that the fluid stress supports most of the load (~80%) and at equilibrium is balanced by the swelling pressure. They emphasize that it is the swelling pressure which reduces the amount of fluid loss such that the solid structures in the disc never sustain large loads. That is, the fluid always supports a significant proportion of the load.

This model appears to provide a simple and elegant description of the daily mechanical cycle of the SMS. The possible effects of swelling pressure on the mechanical behavior of the disc are clearly demonstrated in the decreased fluid loss, decreased vertical height loss, and differences in the flow patterns and stress distribution in the disc when compared with the behavior without swelling effects. However, the stress vs. time results of the model show the disc reaching flow equilibrium in under two hours (i.e. swelling pressure balances fluid stress), although the vertical displacement continues to increase for up to twelve hours which is attributed to annular bulging. This is not the case in *in vitro* experiments in which the displacement, approximately two thirds of which is due to fluid loss [1], does not approach equilibrium after four hours of creep loading [1], and it is probably not the case *in vivo* in which flow equilibrium is most likely never reached during the course of a day [23,24].

While these studies offer useful information concerning the overall mechanical and flow behavior of spinal motion segments, our goal was to model a much more specific area of the disc in detail, which could eventually be incorporated into a larger model. The model presented here is a finite element study of the physical model presented in Chapter 3. The FE model could therefore be validated against the experimental data from the physical model and will be modified in future to represent the *in vivo* situation.

4.2 MATERIALS AND METHODS

Figure 4.2.1 shows the two-dimensional axisymmetric mesh discretization (Model 1) of the physical model. This model was created with the commercially available finite element program ANSYS (Swanson Analysis Systems Inc., Houston, USA, version 5.1). Since poroelastic elements were not available with this version, a paired model was created consisting of a flow model and a structural model. The foam was modeled with a mesh made up of 256 elements and 301 nodes. The glass cylinder and underlying aluminum plate of the physical model were realized through the use of boundary conditions. Contact elements were not used in order to simplify the model and reduce the solution time.

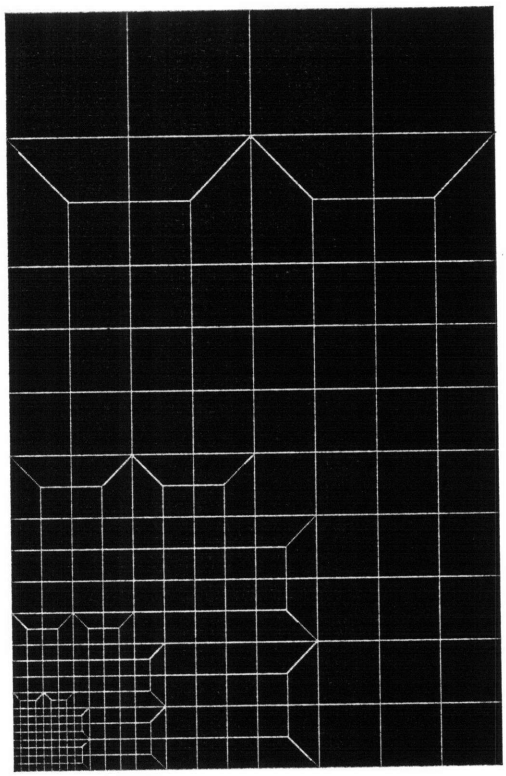

Figure 4.2.1. Mesh discretization of the physical model (Model 1).

The structural model, or SOLID model, consisted of 4-node linear, displacement-based, solid elastic elements (PLANE42). The flow model, or PORO model, was made up of 4-node linear, temperature-based, thermal elements (PLANE55) with an option for non-linear steady-state fluid flow through a porous medium. Thus, the thermal parameters were interpreted as analogous fluid flow parameters.

The conduction heat transfer of the thermal elements is governed by Fourier's Law,

$$\bar{q} = -[D] \cdot \nabla T \tag{4.1}$$

where q ≡ the heat flux vector, $\nabla \equiv [\partial/\partial x \ \partial/\partial y \ \partial/\partial z]^T$, T ≡ temperature, and [D] ≡ the conductivity matrix. For the fluid flow option, the temperature is interpreted as pressure, the heat flux as velocity, and the conductivity matrix is

$$[D] = \begin{bmatrix} \dfrac{K_x^{\infty}\rho}{\mu + K_x^{\infty}E} & 0 & 0 \\ 0 & \dfrac{K_y^{\infty}\rho}{\mu + K_y^{\infty}E} & 0 \\ 0 & 0 & \dfrac{K_z^{\infty}\rho}{\mu + K_z^{\infty}E} \end{bmatrix} \tag{4.2}$$

where K^{∞}_{n}≡ absolute permeability of the porous medium in the n direction, ρ ≡ mass density of the fluid, μ ≡ viscosity of the fluid, $E \equiv \rho\beta S^{\alpha}$, β ≡ visco-inertial parameter of the fluid, S ≡ seepage velocity and α ≡ a given constant [2]. Thus, the fluid flow is essentially governed by Darcy's Law,

$$\bar{u} = -[D] \cdot \nabla P \tag{4.3}$$

In modeling the valve phenomenon it was critical that both material non-linearities and geometric non-linearities in the SOLID model be considered simultaneously, and this was possible through the use of the Updated Lagrange Method [3]. One of the most critical material non-linearities in modeling the valve phenomenon was that of the relationship between permeability and strain. It was not possible to define such a relationship directly in the model, making it necessary to take an iterative approach. The individual element permeabilities of the PORO model elements were adjusted corresponding to the individual element strains from the SOLID model according to the experimentally determined permeability-strain function. This process was repeated until the solution converged, as shown in Figure 4.2.2.

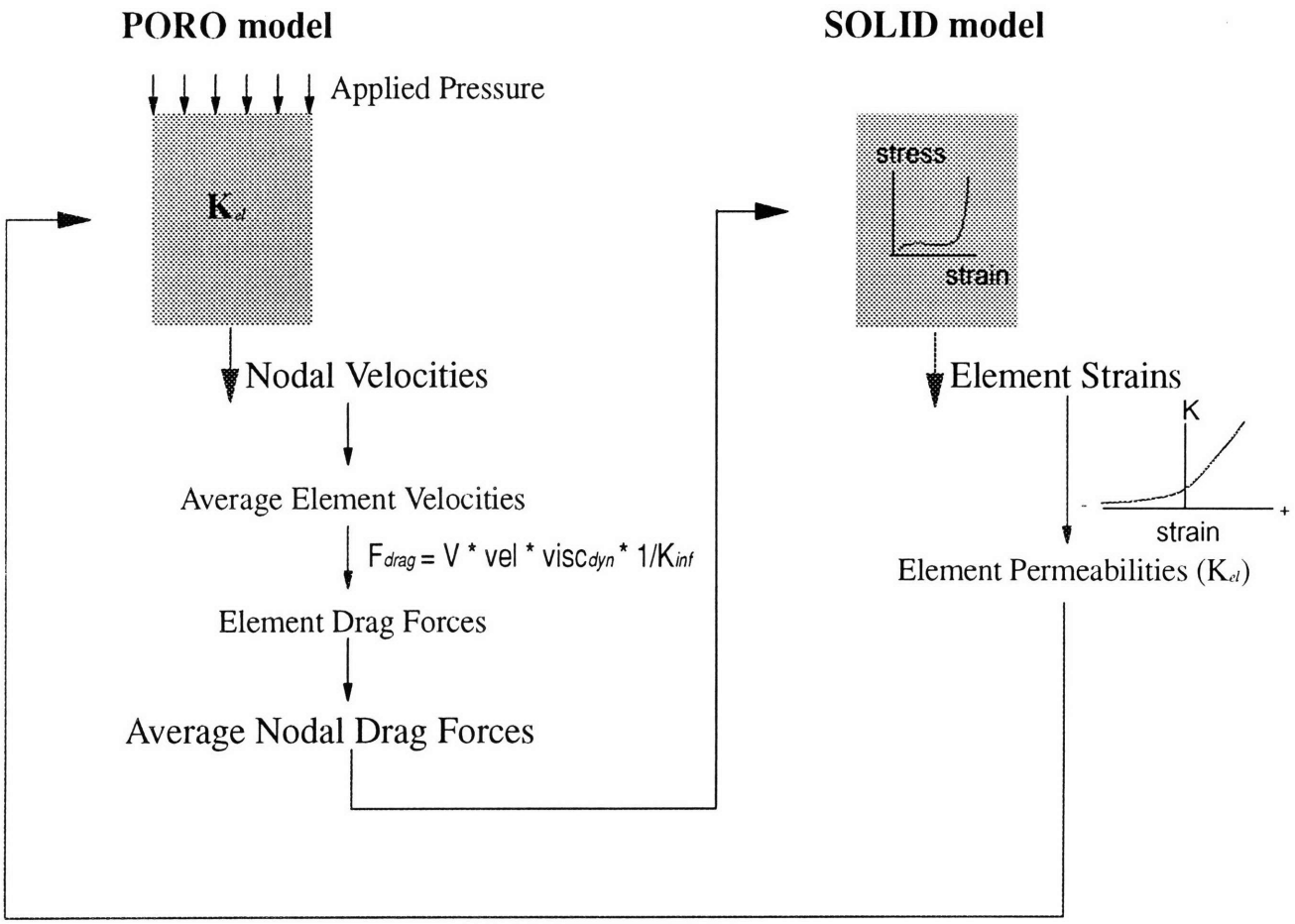

Figure 4.2.2 Schematic diagram of the iteration process.

4.2.1 MATERIAL PROPERTIES

- **Permeability vs. Strain**

Absolute permeability (K_∞) is a material property of a porous material which depends on the cellular solid parameters such as pore size and porosity but which is entirely independent of the solid geometry and properties of the permeating fluid, i.e. density and viscosity [14]. For example, one experimentally derived equation defining the absolute permeability of a material with pores of average diameter d is

$$K_\infty = a \cdot d^2 \cdot (1 - \rho^* / \rho_s)^{3/2} \qquad (4.4)$$

where a is a constant which normally takes the empirical value 0.4 and the term $(1 - \rho^* / \rho_s)^{3/2}$ describes the porosity [5]. However, there exists no clear definition of absolute permeability for "irregular" poroelastic materials such as soil or sand, since variables such as the interconnections between the pores, grain size distribution, shapes of the grains and degree of cementation are difficult to measure and make it difficult to calculate the permeability accurately [14].

The PORO finite element model required an input value of absolute permeability. For the "regular" poroelastic material used in the physical model (polyurethane) K_∞ could be calculated from the experimentally measured permeability values (see Chapter 3 Section 3.3) in the following way.

From Darcy's Law:

$$u = -\frac{K_\infty}{\upsilon} \cdot \frac{dp}{dx} \tag{4.5}$$

where u ≡ fluid velocity (m/s); dp/dx ≡ pressure gradient (Pa/m) and υ ≡ fluid dynamic viscosity (m^2/s), and from mass conservation:

$$u = \frac{Q}{A}. \tag{4.6}$$

The overall permeability, K, is known from:

$$K = \frac{Q}{\Delta P} \tag{4.7}$$

where Q ≡ measured volume flow into or out of they system (m^3/s); A ≡ the cross-sectional area of the foam (m^2); and ΔP ≡ applied pressure gradient (Pa).

Assuming a constant velocity through the solid (steady state conditions) and therefore a spatially constant pressure gradient such that dp/dx = ΔP / h where h ≡ total distance of fluid travel through the solid, substitution and rearrangement of Darcy's Law gives,

$$\boxed{K_\infty = K \cdot \frac{h}{A} \cdot \upsilon}. \tag{4.8}$$

From the above equations the absolute permeability could therefore be calculated directly from the experimental data (measured flow rate, applied pressure, solid geometry and fluid

dynamic viscosity) without knowing the pore size or porosity of the solid matrix. Furthermore, the absolute resistance ($R_\infty = 1/K_\infty$) could then be used to calculate the drag forces in Equation (4.12).

While the PORO model required the input of absolute permeabilities, the large strain analysis of the SOLID model required the stress-strain curve to be input in terms of true strain (ε_t). Therefore, the experimentally determined curve of the permeability (K) vs. axial engineering strain (ε_y) (see Chapter 3 Section 3.3) was converted to one of absolute permeability vs. true strain ($\varepsilon_t = \ln(1 + \varepsilon_y)$). A function defining this curve was then found using a commercially available data analysis and curve-fitting package (KaleidaGraph data analysis/graphics application, Abelbeck Software). The curve fit can be seen in Figure 4.2.3.a. This curve was then used to determine the individual element absolute permeabilities corresponding to the element strains output from the SOLID model. Although experimental values for tension were not available this curve was extrapolated into the tensile strain axis and the behavior was found to be a reasonable representation of that of poroelastic materials in tension [5]. The curve of absolute permeability vs. true strain used in the FE solution is shown in Figure 4.2.3.b.

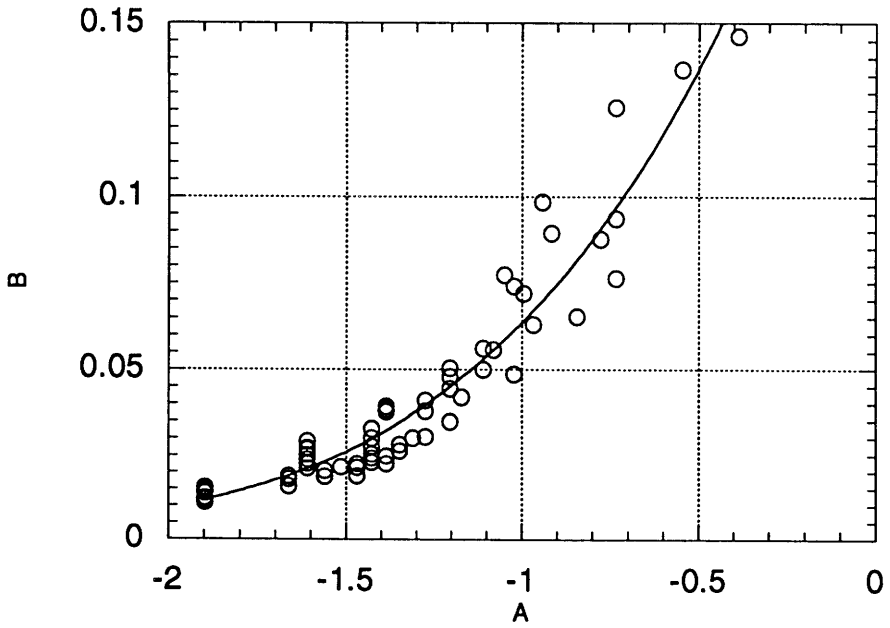

Figure 4.2.3 .a The function (solid line) fit to the physical model experimental data (circles) for permeability vs. strain. A = true strain; B = permeability.

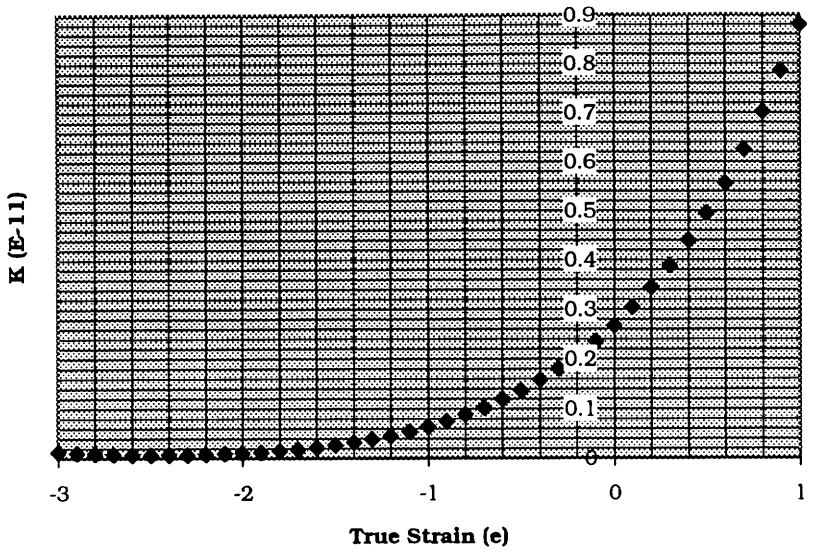

Figure 4.2.3.b Curve of 4.2.3.a extrapolated into the tensile strain axis and used in the finite element solution.

An initial, uniform, isotropic permeability was applied to the PORO model for the first step of the solution; the initial value used was that of the permeability of the foam at zero strain. Throughout the entire solution the permeability was assumed isotropic, since only the axial permeability change with strain of the physical model was found experimentally, and this relationship was also assumed in the radial direction. The measured viscosity of 0.7 kg/s·m and fluid density of 1263 kg/m^3 of the glycerin were also input into the PORO model.

- **Stress vs. Strain**

A piece-wise, non-linear, elastic stress-strain curve was input to the SOLID model according to the experimental data from the physical model as shown in Figure 4.2.4. The experimental curve was extrapolated beyond the maximum applied strain of 85% such that the stress approached infinity at 100% strain. This MELAS (multi-linear elastic) table could be used with a limited number of element types which eliminated the possibility of using viscoelastic elements, although such elements are recommended for more accurate solutions at large strains (>50%) [2]. It was also impossible to input an asymmetric stress-strain curve with the non-linear elastic MELAS table. Symmetry in tension and compression was therefore assumed.

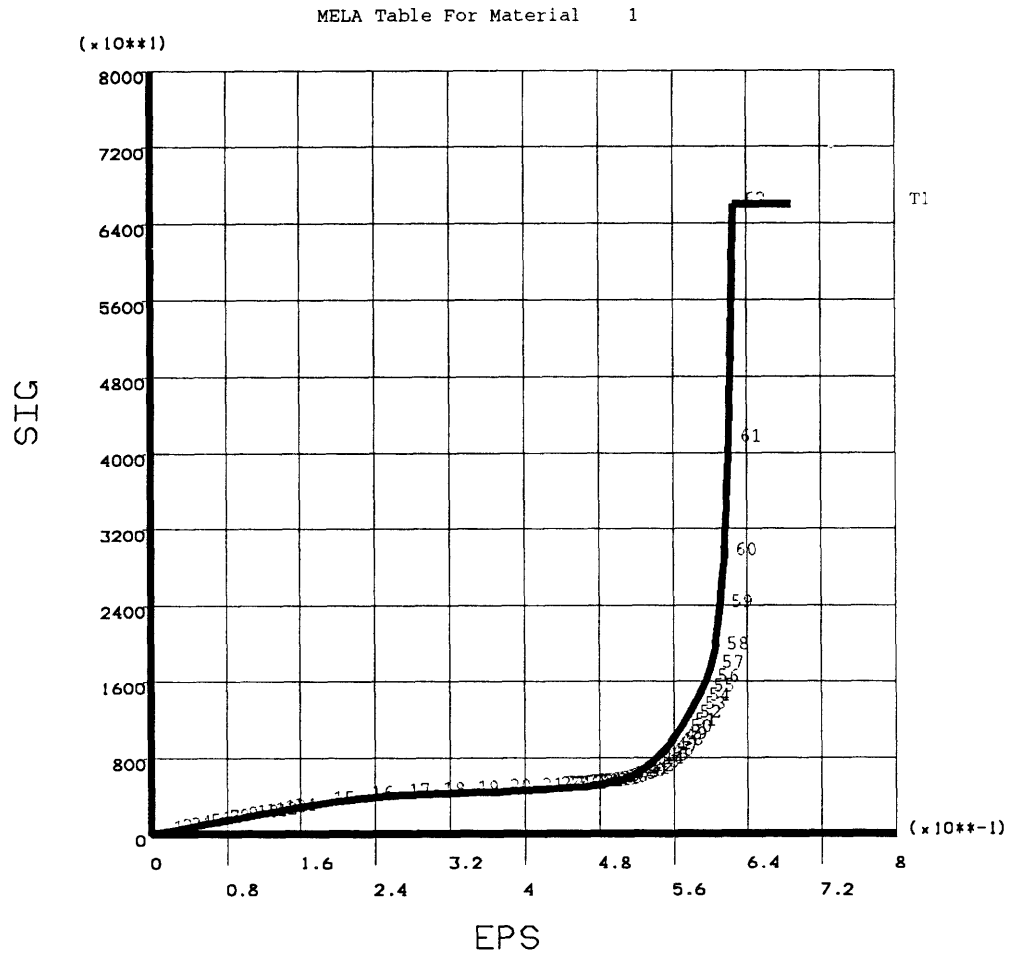

Figure 4.2.4 The non-linear stress-strain curve input into ANSYS in the form of this MELAS table (multi-linear elastic).

ANSYS defines an equivalent total strain measure (ε_e^t) computed from the total strain components (ε_n) (4.9):

$$\varepsilon_e^t = \frac{1}{\sqrt{2}(1+\nu)}\left[(\varepsilon_x - \varepsilon_y)^2 + (\varepsilon_y - \varepsilon_z)^2 + (\varepsilon_z - \varepsilon_x)^2 + \frac{3}{2}(\varepsilon_{xy})^2 + \frac{3}{2}(\varepsilon_{yz})^2 + \frac{3}{2}(\varepsilon_{zx})^2\right]^{\frac{1}{2}}$$

where $\nu \equiv$ Poisson's ratio. ε_e^t is used with the input stress-strain curve to find the equivalent value of stress σ_e. From these values, the linear component of strain can be computed:

$$\{\varepsilon_n^l\} = \frac{\sigma_e}{E\varepsilon_e^t}\{\varepsilon_n\} \qquad (4.10)$$

where E = stiffness and the non-linear component is therefore:

$$\left\{\varepsilon_n^{nl}\right\} = \left\{\varepsilon_n\right\} - \left\{\varepsilon_n^{l}\right\} \tag{4.11}$$

A Poisson's ratio of 0.3 and a density of 27 kg/m^3 were assumed according to the average material properties of polyurethane [5].

4.2.2 BOUNDARY CONDITIONS

- **PORO Model**

The boundary conditions for the PORO model are shown graphically in Figure 4.2.5. Fluid flow (HEAT) was not allowed through the outer "wall" or through the bottom of the foam except at the hole (linear arrows). For exudation flow constant pressure was applied across the top surface of the foam as an analogous temperature (TEMP) boundary condition at the nodes while zero pressure was similarly applied across the surface of the hole (triangular arrows). For imbibition flow constant pressure was applied across the surface of the hole while zero pressure was applied across the top of the foam. No boundary conditions were applied along the axis of symmetry.

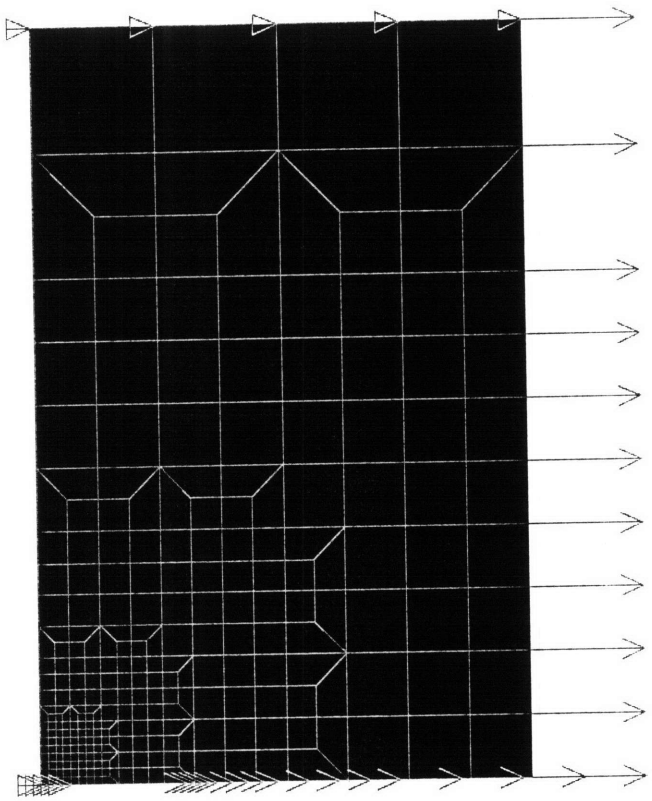

Figure 4.2.5 PORO model boundary conditions. The triangular arrows represent the pressure boundary conditions, while the linear arrows represent the flow boundary conditions (i.e. zero-flow).

• SOLID Model

The displacement boundary conditions for the SOLID model are shown by the triangular arrows in Figure 4.2.6. Radial displacement (UX) was set to zero along the peripheral vertical surface of the foam in order to model the confining behavior of the cylinder wall. This displacement could not be confined in a singular radial direction (i.e. in the positive radial direction only) which would be true to the physical model situation, without the use of contact elements. Therefore, the foam in the FE model was also restricted from bulging inward. Although this was not the case in the physical model, inward bulging was never observed by eye during the experiments and was therefore assumed negligible. Thus, the use of contact elements could be avoided, which were found to increase the solution time immensely. Radial displacement was also restricted along the axis of symmetry, as recommended in the ANSYS manual [2], in order to avoid artificial element distortion during the solution. Assuming perfect symmetry in the physical model geometry and in the applied

loads, radial displacement along the axis of symmetry could, of course, be realistically assumed to be zero. Radial and axial displacement (UX and UY) were restricted along the lower face of the foam except at the hole.

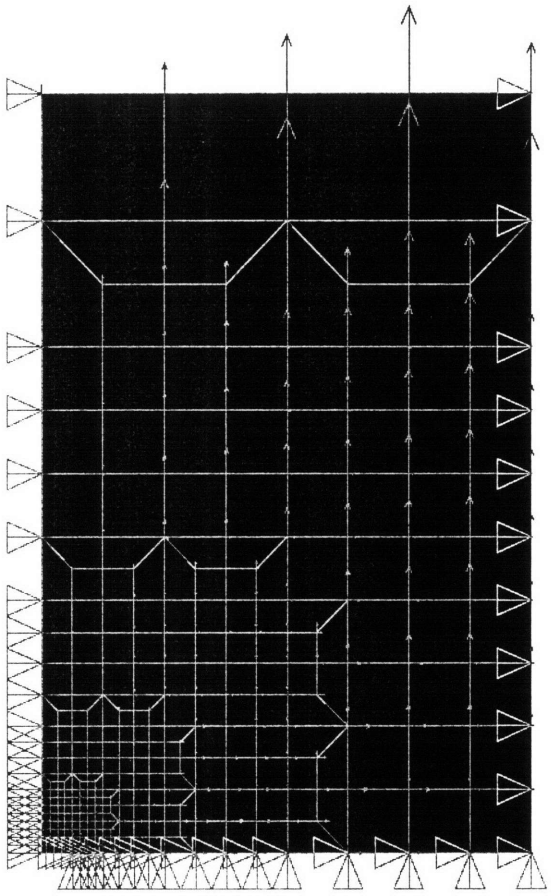

Figure 4.2.6 SOLID model boundary conditions. The triangular arrows represent the displacement boundary conditions (i.e. zero-displacement), while the linear arrows represent the applied nodal forces.

4.2.3 LOADING CONDITIONS

Pressures were applied to the PORO model as analogous temperature boundary conditions along the top surface and along the hole surface of the foam for exudation and imbibition respectively. Pressures were applied to simulate the experimental conditions of the physical model in a range of 0.0316 bar to 0.8416 bar. While in the physical model pressures were applied up to a maximum of 2.492 bar, severe element distortions at the edge of the hole for applied pressures beyond 0.8416 bar restricted solutions to the above range. All graphical results are presented at a representative applied pressure of 0.3916 bar only (approximate

median value of applied pressures). Any forces due to the friction of the foam on the wall of the glass cylinder were neglected.

Nodal drag forces derived from the PORO model velocity output (see following sub-section) were applied to the SOLID model as shown by the linear arrows in Figure 4.2.6.

4.2.4 SOLUTION METHOD

Nodal velocities were determined from the initial solution of the PORO model for a given applied pressure and initial uniform permeability (the permeability at zero applied strain). Code was written (see Appendix, Section A.2.3) to first convert the nodal velocities from the PORO model to nodal drag forces to be applied to the SOLID model. ANSYS macros were written (see Appendix, Section A.2.4) to output values of nodal velocities, element volumes and element node numbers from the PORO solution into data arrays. This data was input into further code to calculate the average element velocity from the nodal velocities. The drag force on the element was then calculated using the equation,

$$\boxed{F_d^{el} = u \cdot \forall \cdot \upsilon \cdot R_\infty} \qquad (4.12)$$

where $u \equiv$ average element velocity (m/s), $\forall \equiv$ element volume (m^3), $\upsilon \equiv$ fluid dynamic viscosity (m^2/s), and $R_\infty \equiv$ absolute resistance of the foam calculated using Equation 4.8.

Average nodal drag force vectors were calculated from the element drag forces output for the four surrounding elements of each node. These nodal forces were then applied to the SOLID model. The large strain, SOLID solution, element axial strains (ε_y) were output from ANSYS into data arrays and used to calculate the local element permeabilities (from the experimentally determined permeability-strain curve) to be applied to the PORO model (see macros and code in Appendix, Sections A.2.1 and A.2.2). The local element absolute permeabilities were then applied to the PORO model by assigning each element a unique material number with its corresponding permeability. Pressure was again applied, and the nodal velocities found from the PORO model solution were used to recalculate the drag forces on the SOLID model. This iterative process was continued until the SOLID model nodal strains converged to within at least 0.02% for consecutive iterations.

The volume flow (Q) through the hole for both imbibition and exudation was calculated at each iteration step and the final value was compared to that found experimentally. Q was calculated for each hole element from the average velocity of the two lower nodes and the

total cross-sectional area of the element, as shown in Figure 4.2.7. The elemental volume flows were then summed to give the total volume flow rate through the hole.

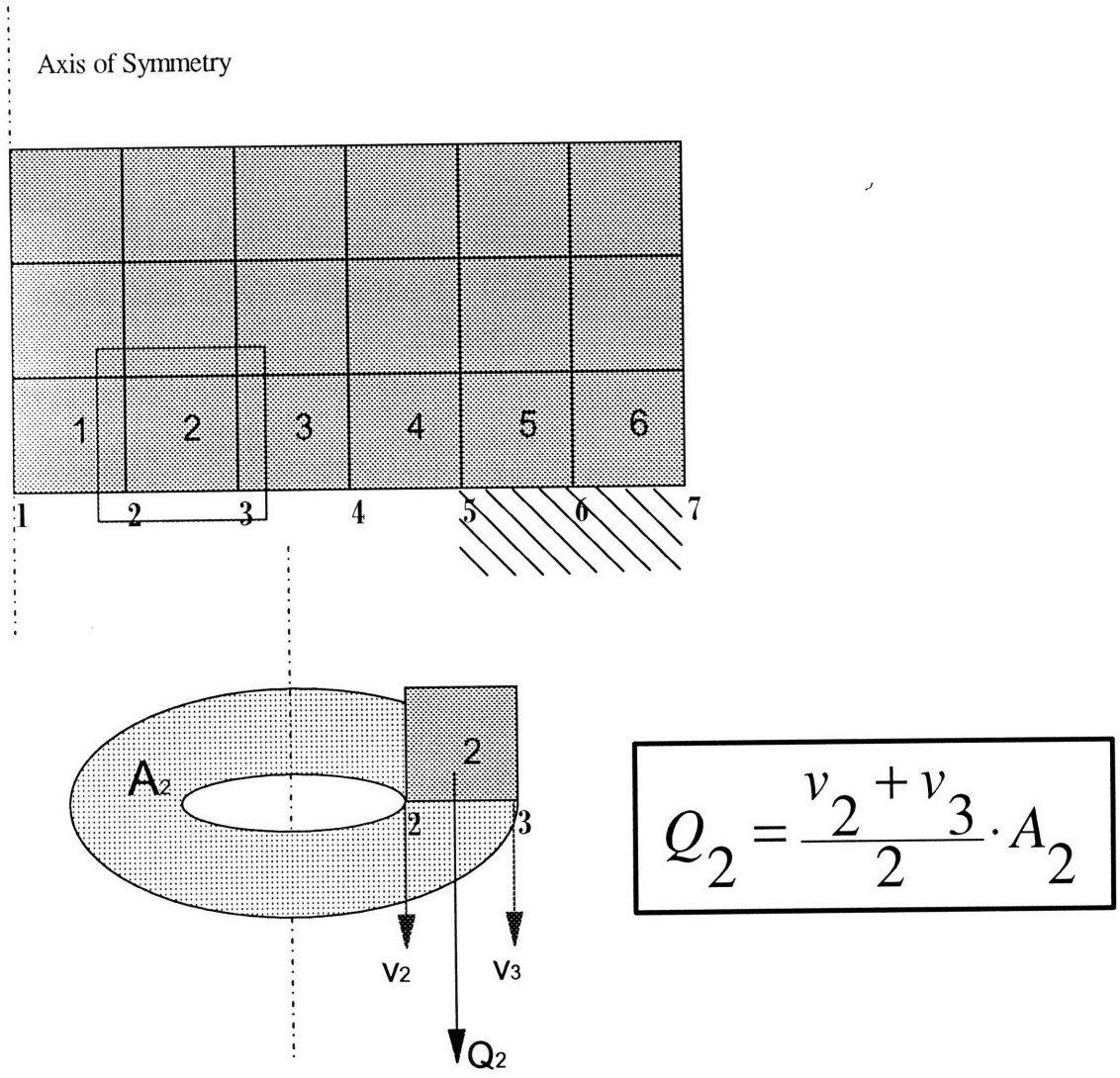

Figure 4.2.7 Schematic diagram demonstrating the method used to calculate the volume flow rate (Q) at the hole.

All solutions used a frontal solver with full Newton Raphson equilibrium iteration technique and with adaptive descent when necessary. Auto time-stepping was used for the SOLID model solution with the maximum number of substeps set anywhere from 100 to 1000 depending on the pressure applied, and the maximum number of equilibrium iterations set to 100. Predictor-Corrector was not used since it was not found to improve the convergence of the solution. Convergence tolerances were set in the SOLID model for both force and displacement due to the behavior of the non-linear stress-strain curve. The force tolerance

was set to 10% of an ANSYS calculated norm (SRSS norm) of the applied nodal forces and that of the displacement was set to 1%.

4.2.5 MESH CONVERGENCE STUDY

A mesh convergence study was performed to ensure adequate solution convergence and to determine the discretization error in the model. Three mesh refinements were performed, increasing the original number of elements from 256 with 4 elements across the hole (Model 1 as in Figure 4.2.1) to 580 with 8 elements across the hole (Model 2) and 1528 with 16 elements across the hole (Model 3). Model 2 incorporated a refinement of the mesh at the hole and throughout the entire model, while Model 3 incorporated a further refinement of the mesh at the hole only, as shown in Figures 4.2.8.a and 4.2.8.b. The converged solution flow rates were compared for the three models at two different applied pressures (0.0916 bar and 0.3916 bar).

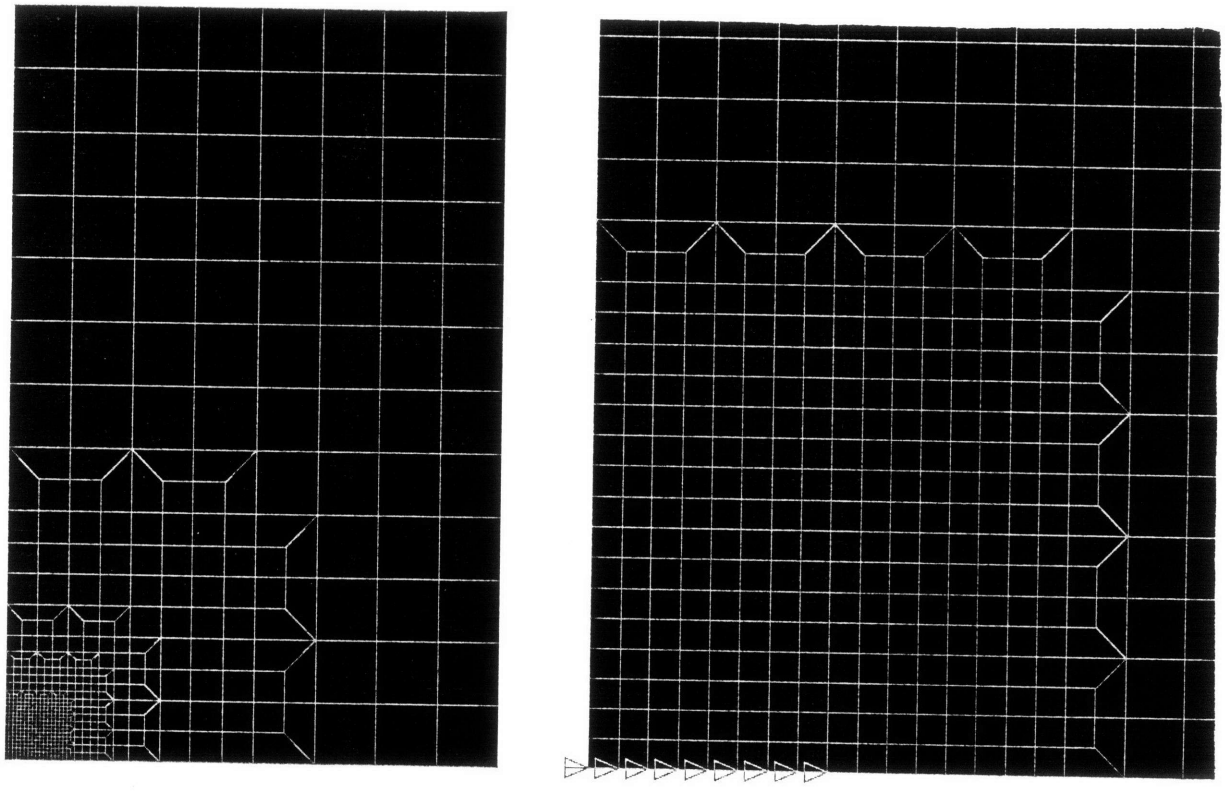

Figure 4.2.8.a Model 2 mesh discretization (580 elements total, 8 elements across the hole).

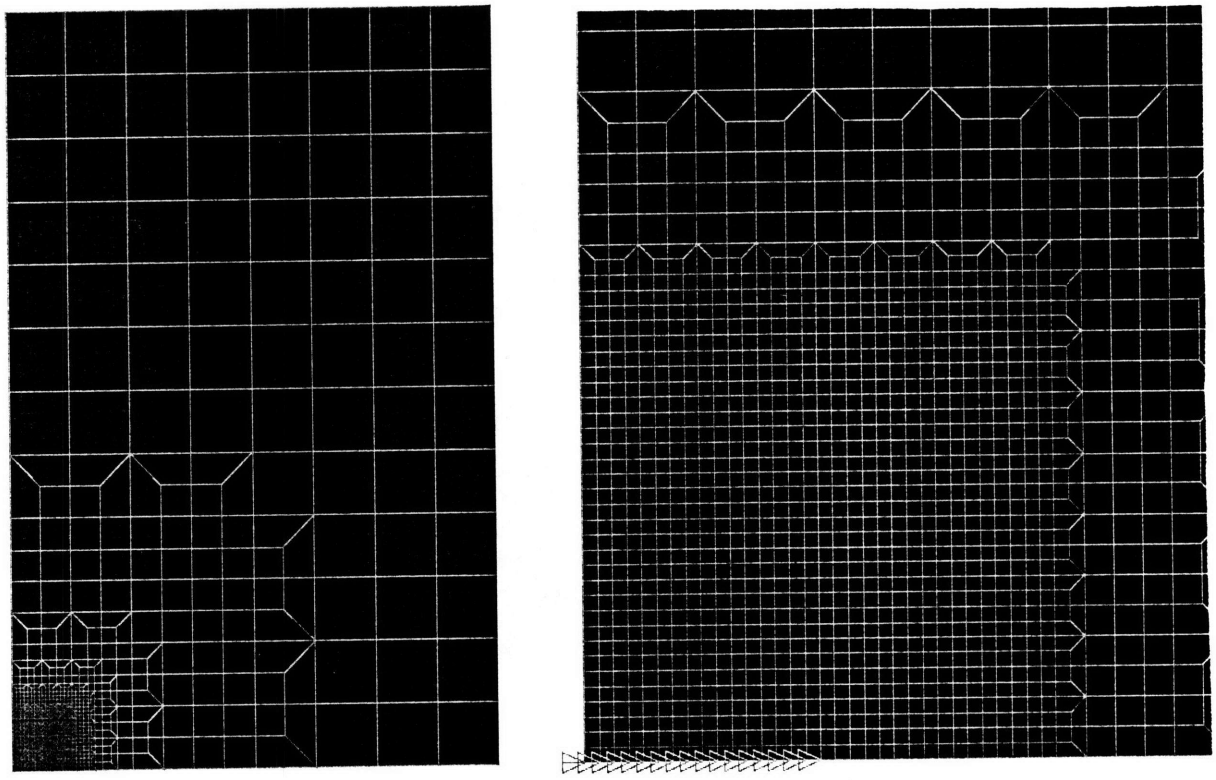

Figure 4.2.8.b Model 3 mesh discretization (1528 elements total, 16 elements across the hole).

4.2.6 SIMULATION OF ENDPLATE CALCIFICATION

Calcification of the cartilage endplate results in a deposit on the bony endplate which covers the constriction holes, thereby reducing their size and eventually reducing the total number of holes. This would result in a disturbance of the normal daily intradiscal fluid flow. Simulations were performed with the finite element model to determine the effects of a decrease in the constriction hole area as well as a decrease in the draining area (i.e. the cross-sectional area of the foam, since a decreased number of holes in the bony endplate would result in an increase in the cross-sectional draining area of each hole). These dimensions are shown for clarity in Figure 4.2.9. A comparison of the effect of a change in the size of the constriction hole and a change in the number of holes with respect to the hole area fraction of the draining area was also made.

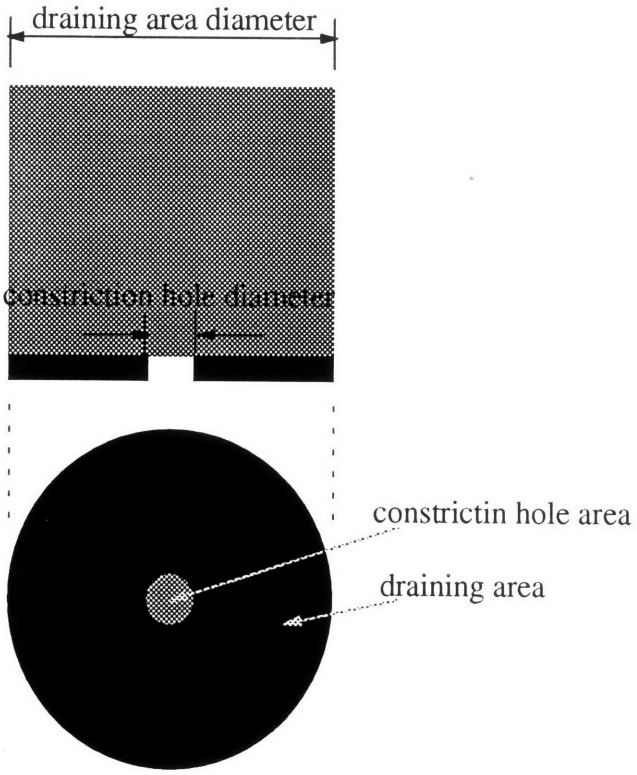

Figure 4.2.9 Schematic diagram indicating the "draining area diameter" and the "constriction hole diameter" of the physical model.

- **Change in Size of the Hole**

The diameter of the constriction hole was increased from 4 mm to 14 mm in 6 increments (4, 6, 8, 10, 12, and 14 mm corresponding to 2, 3, 4, 5, 6, and 7 elements in the axisymmetric model) by adjusting the boundary conditions at the hole, while the draining area diameter of the foam was kept constant at 128 mm. The effect on both the absolute exudation and imbibition resistances as well as the resistance ratio of exudation resistance to imbibition resistance were studied at an applied pressure of 0.3916 bar.

- **Change in Number of Holes**

The constriction hole diameter was kept constant at 8 mm while the draining area diameter of the foam was increased from 32 mm to 240 mm in six increments (32, 64, 96, 128, 176, and 240 mm). The finite element meshes of the two extremes (∅ 32 mm and ∅ 240 mm) are shown in Figure 4.2.10. The effect on the absolute resistances as well as on the resistance ratio were studied for two different applied pressures of 0.3916 bar and 0.8416 bar. The data was normalized by the relative number of holes for each draining area calculated with respect

to the fraction of constriction hole area to draining area in Model 1. That is, Model 1 was taken as having one hole, and the relative number of holes was calculated for all other draining areas in the following way:

Model 1 constriction hole area = $A_{1ch} = \pi \cdot 0.004^2$

Model 1 draining area = $A_{1drain} = \pi \cdot 0.064^2$

Fraction hole area to draining area = $A_{1ch} / A_{1drain} = 0.0039 \Rightarrow$ one hole

Relative number of holes = $f = (A_{1ch} / \pi \cdot r_{drain}^{\ 2}) / 0.0039$

The volume flow rate through the constriction hole found for each draining area was then multiplied by the relative number of holes, and this value was used to calculate the resistance to flow:

$$R = \frac{\Delta P}{Q \cdot f} \tag{4.14}$$

where Q is the flow rate through the hole calculated from the FE model as demonstrated in Figure 4.2.7, and $\Delta P \equiv$ applied pressure gradient.

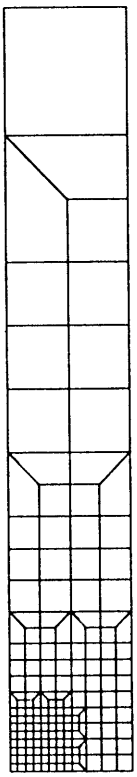

Figure 4.2.10.a Mesh discretization of the 32 mm (smallest) outside diameter model.

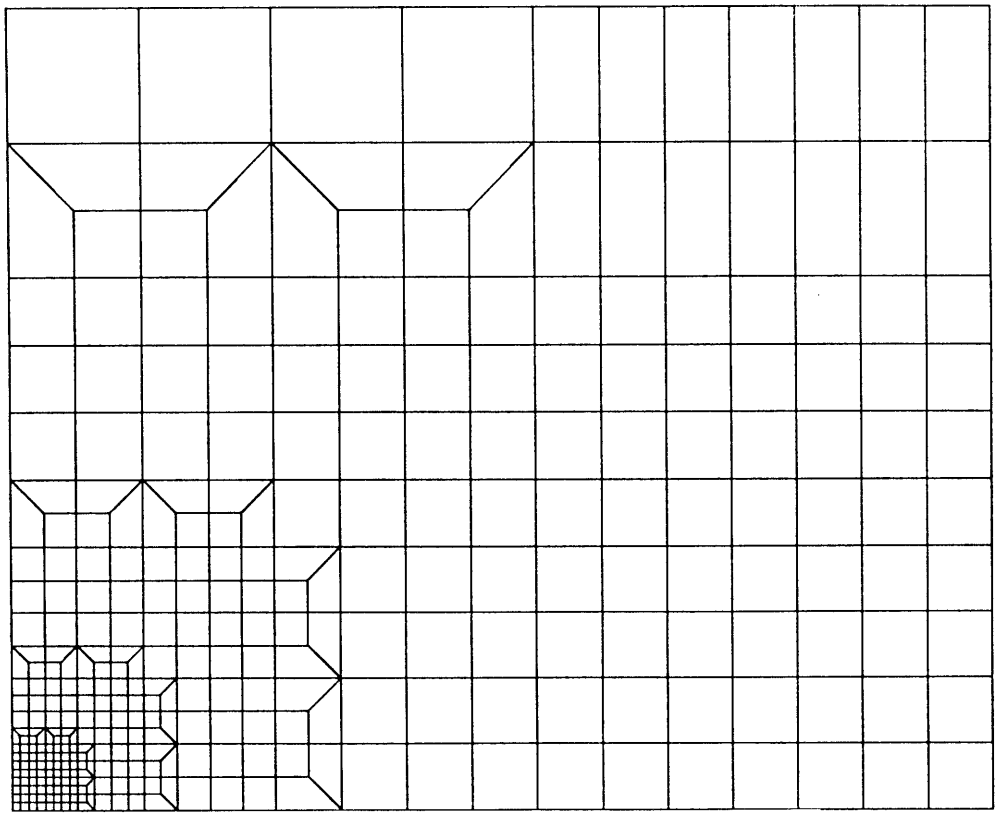

Figure 4.2.10.b Mesh discretization of the 240 mm (largest) outside diameter model.

4.3 RESULTS

4.3.1 ANSYS SOLUTION

The increase in solution time for the SOLID model rose with increasing applied pressures. This was due to a combination of the non-linear stress-strain curve, which resulted in high local strains, and the use of large strain analysis. The solution time was found to decrease considerably when either a linear stress-strain curve was used or large strain was turned off. Convergence problems were encountered at high applied pressures due to large strain analysis, since elements at the periphery of the hole underwent extreme deformations. An attempt at mesh refinement did not reduce the individual element distortions at the periphery. The replacement of highly distorted elements with triangular elements did improve convergence, but the model required adjustment through trial and error at each applied pressure and the procedure was abandoned. Removal of the sharp "corner" at the hole periphery by the addition of a small radius would be most likely to have solved the convergence problem. However, this would require the use of contact elements and would have significantly increased the solution time. It was therefore neglected at this stage, and for this reason solutions could not be found for the full range of pressures applied experimentally (up to 2.492 bar) but only up to 0.8416 bar.

4.3.2 SOLUTION CONVERGENCE

The solution was found to converge quite rapidly, with a maximum of approximately 12 iterations required to reach convergence for exudation flow. Greater element distortions during exudation flow as well as higher element strains at higher applied pressures always necessitated a greater number of iterations. Some examples of the convergence of the PORO model flow rate through the hole are shown graphically in Figures 4.3.1 and 4.3.2.

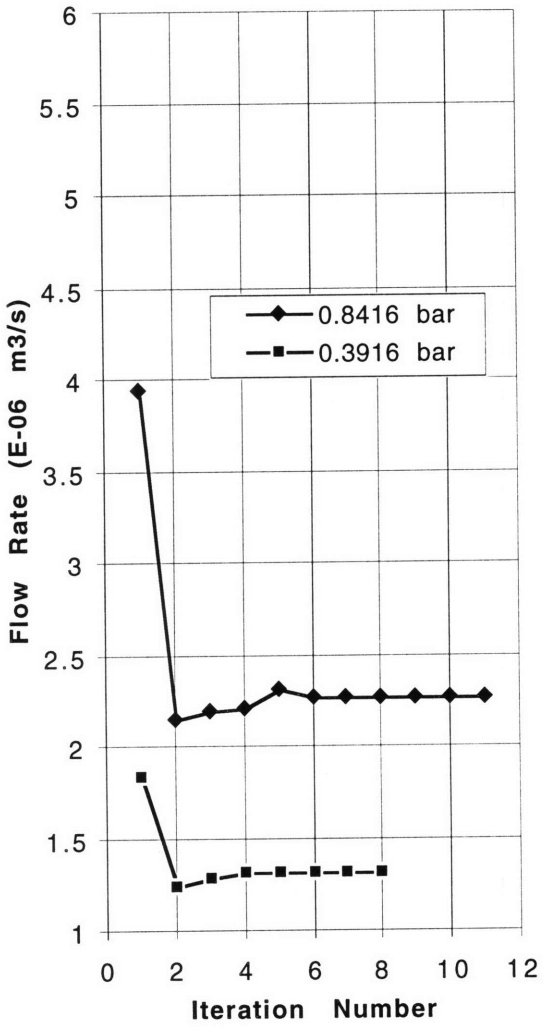

Figure 4.3.1 Iterations for exudation flow at 0.8416 bar and 0.3916 bar.

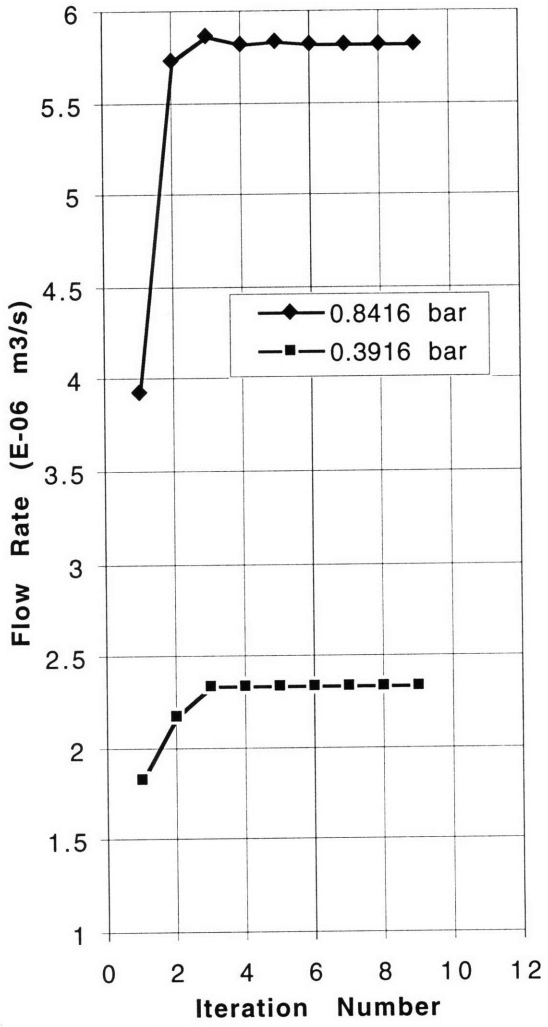

Figure 4.3.2 Iterations for imbibition flow at 0.8416 bar and 0.3916 bar.

4.3.3 MODEL VALIDATION

The final converged flow rate values at all applied pressures for imbibition and exudation are listed in the Appendix (Table A.1.2) along with the derived resistances (P / Q), and these can be compared to the experimental values also listed in the table. A comparative plot of the imbibition and exudation resistances vs. applied pressure for both the physical model (mean values with average standard deviation) and the finite element model is shown in Figures 4.3.3 and 4.3.4. The change in resistance of the finite element model with applied pressure, for both imbibition and exudation, was found to follow a very similar pattern to that of the physical model, however, the values did not lie within the standard deviation of the physical

model. A plot of the change in resistance ratio with applied pressure for both the physical model and the finite element model is shown in Figure 4.3.5.

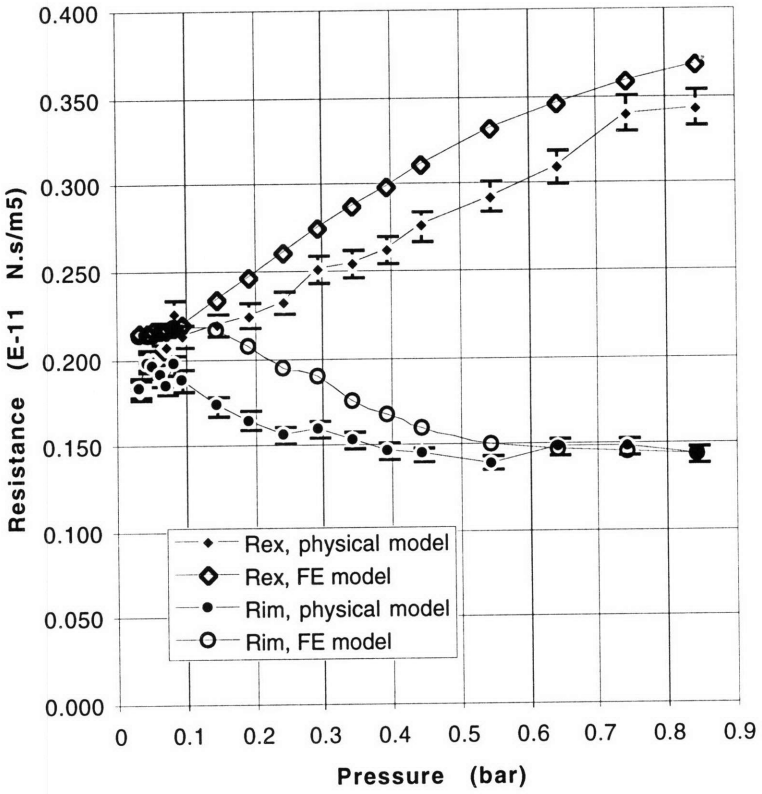

Figure 4.3.3 Exudation resistance (R_{ex}) and imbibition resistance (R_{im}) vs. applied pressure for the physical model and finite element model.

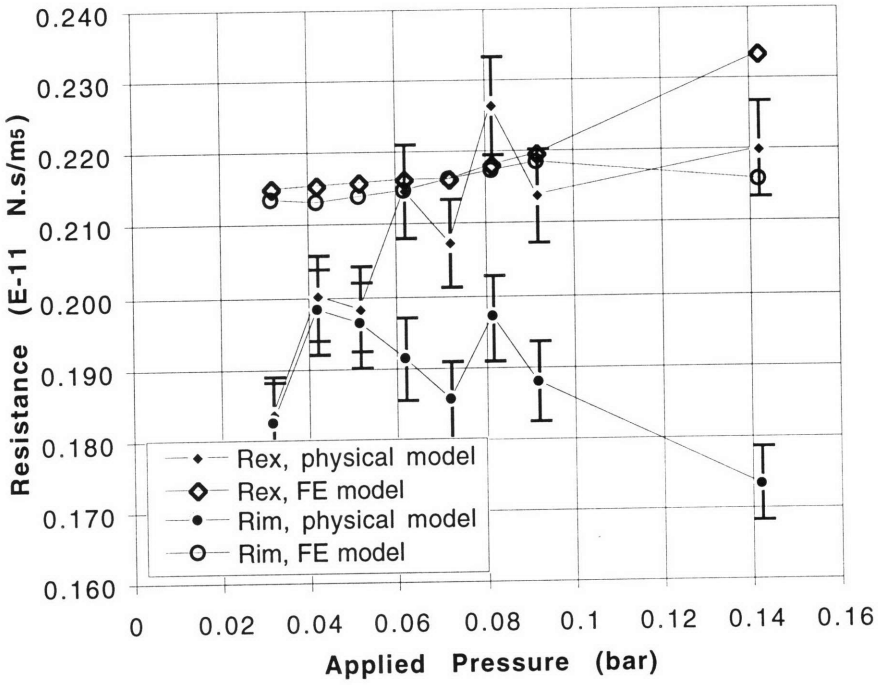

Figure 4.3.4 Exploded view of Figure 4.3.3 at low applied pressures.

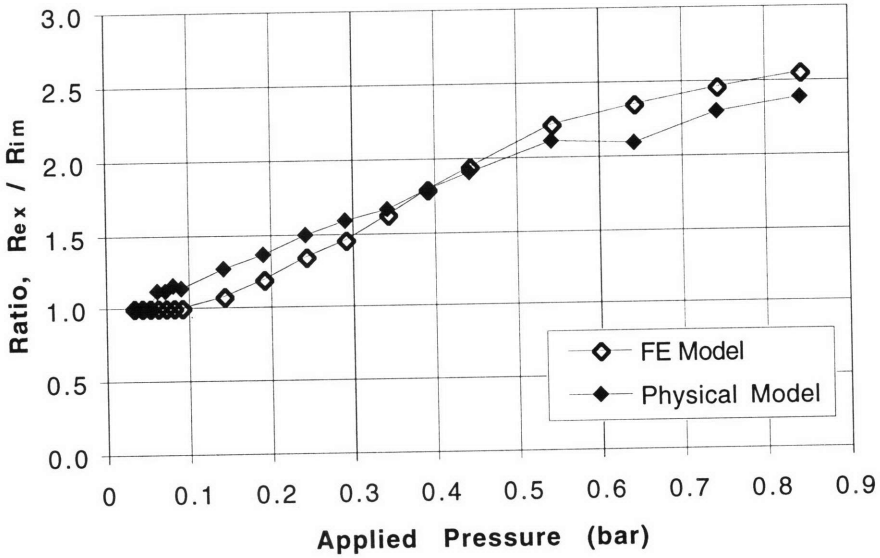

Figure 4.3.5 A comparison of the ratio of exudation resistance to imbibition resistance vs. applied pressure for the finite element model and experimental data of the physical model.

4.3.4 FLOW PATTERN AND CORRESPONDING STRAIN

The flow pattern of the PORO model and corresponding strain of the SOLID model (radial, axial, hoop and volumetric) for exudation and imbibition at an applied pressure of 0.3916 bar are shown in Figures 4.3.6 and 4.3.7 respectively. The areas of high velocity in the PORO model corresponded to areas of high strain in the SOLID model. The highest velocity for both imbibition and exudation was observed at the periphery of the hole. The velocities through the top half of the foam and around the outer circumferential "corner" were very low.

- **Exudation**

For exudation, the high peripheral velocity through the hole corresponded to the area of the highest axial compressive strain (EPTOY) and highest radial tensile strain (EPTOX) (plus a small compressive hoop strain), although the magnitude of the compressive strains clearly dominated, resulting in compressive volumetric strain at the periphery. The volume of matrix directly above the hole can be seen to be in axial tension which would act to expand the matrix and reduce the resistance to flow, however, the magnitude of the compressive hoop and radial strains in the same location approximately balance these tensile effects. The strains in the volume above the hole, combined with the high axial compressive strains observed at the periphery of the hole resulted in an overall compressive volumetric strain as shown in Figure 4.3.6.e, resulting in a high resistance to flow.

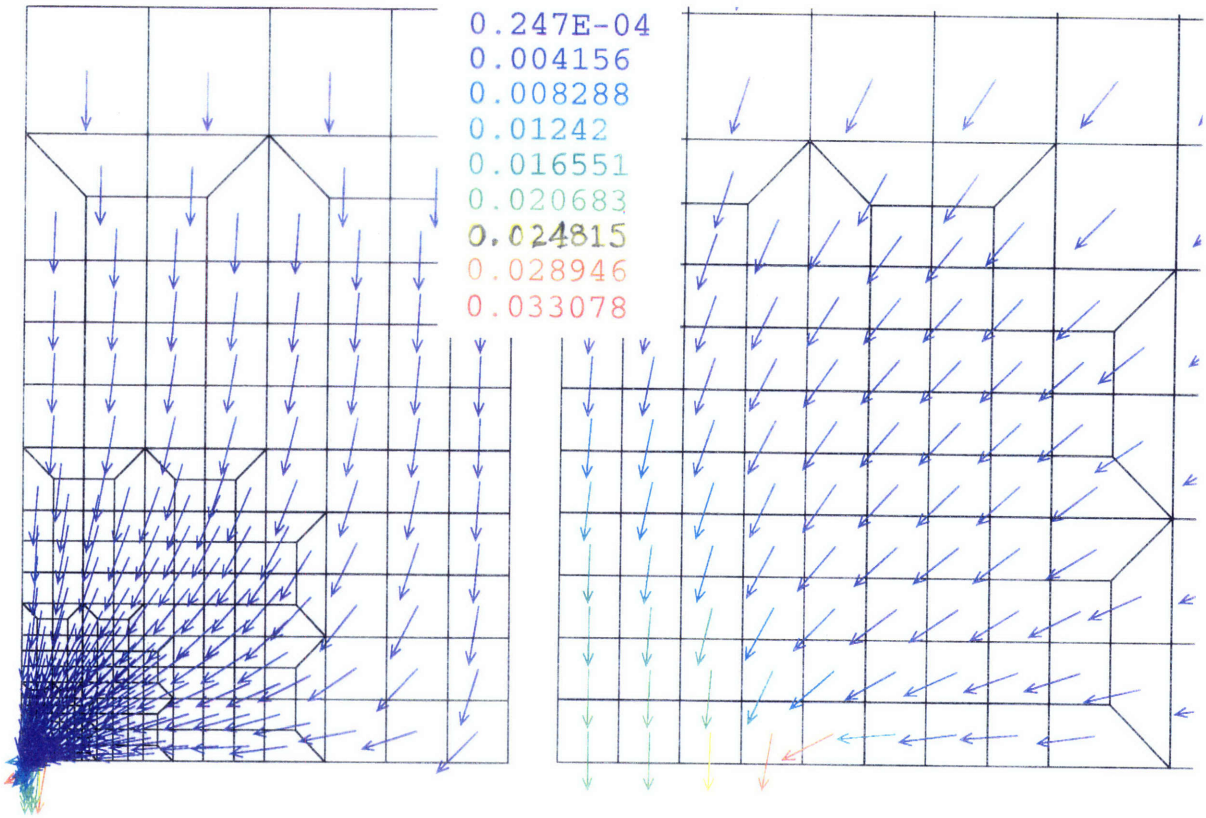

Figure 4.3.6. a) Exudation velocity (m/s); P = 0.3916 bar (full view and close-up at the hole).

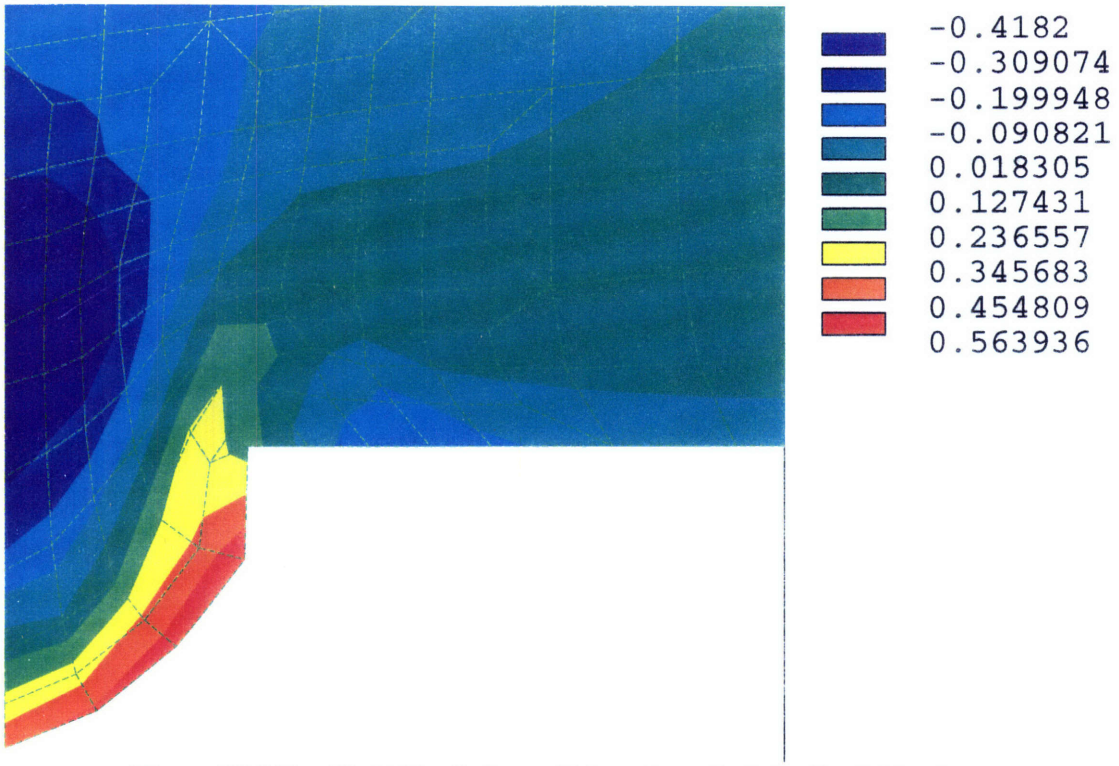

Figure 4.3.6 Cont'd. b) Exudation radial strain at the hole; P = 0.3916 bar.

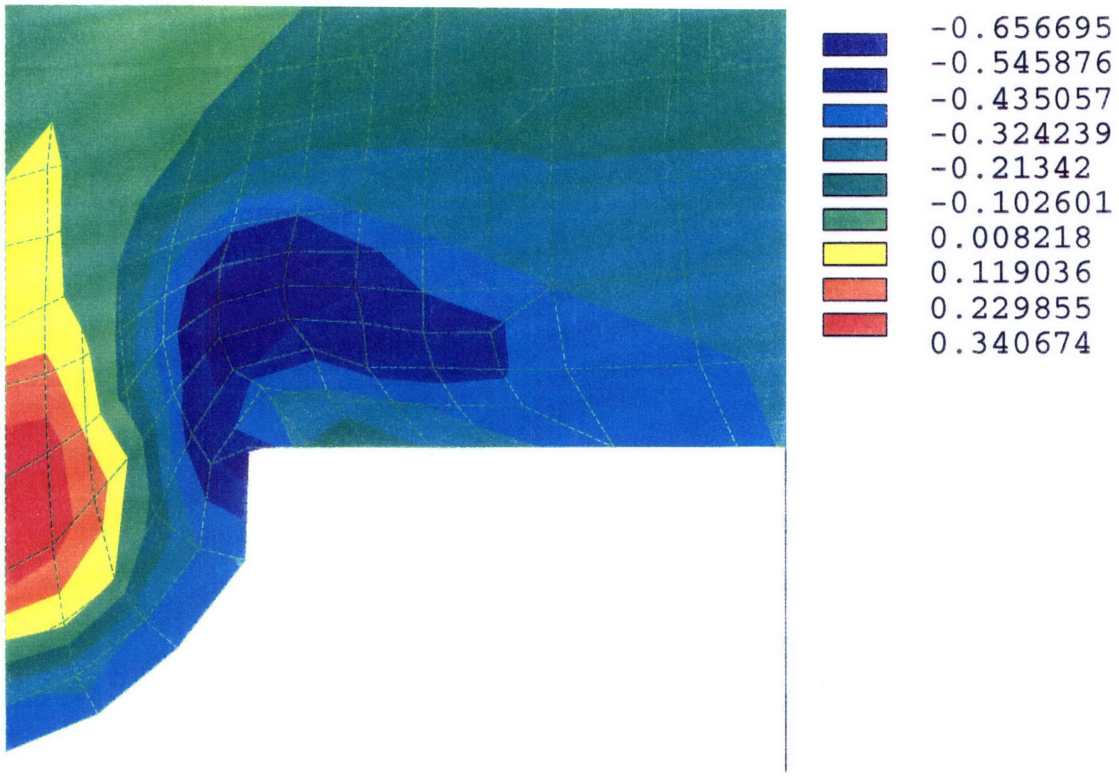

Figure 4.3.6 Cont'd. c) Exudation axial strain at the hole; P = 0.3916 bar.

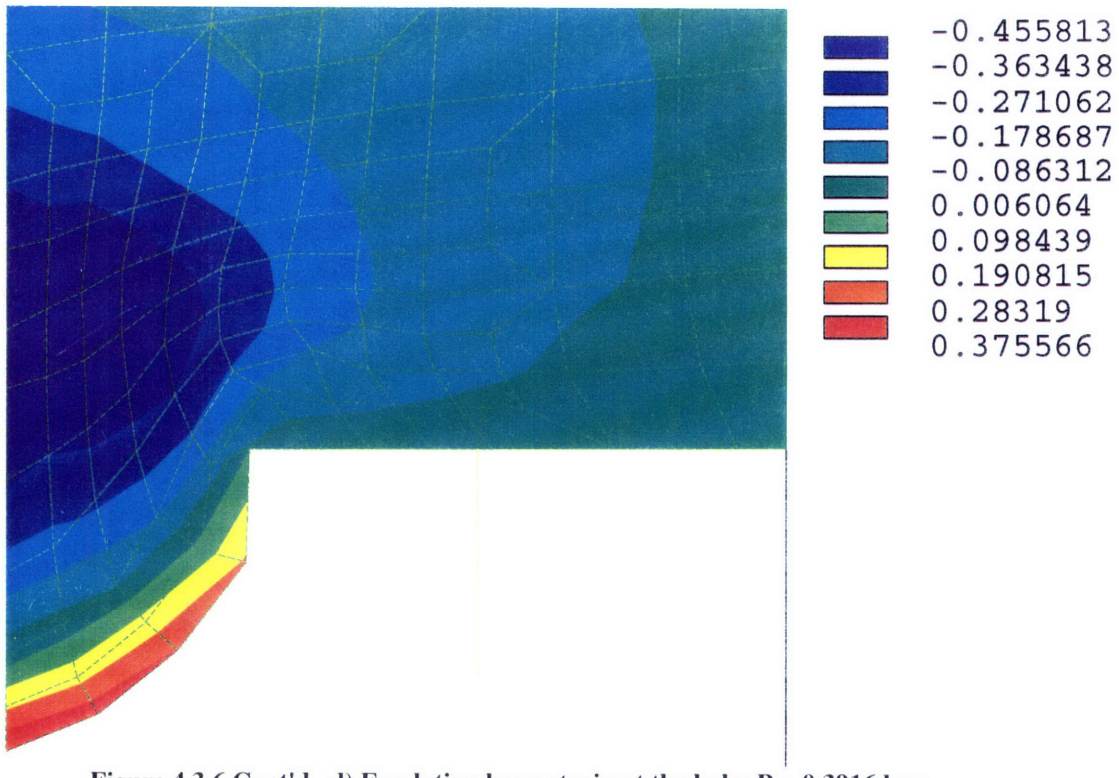

Figure 4.3.6 Cont'd. d) Exudation hoop strain at the hole; P = 0.3916 bar.

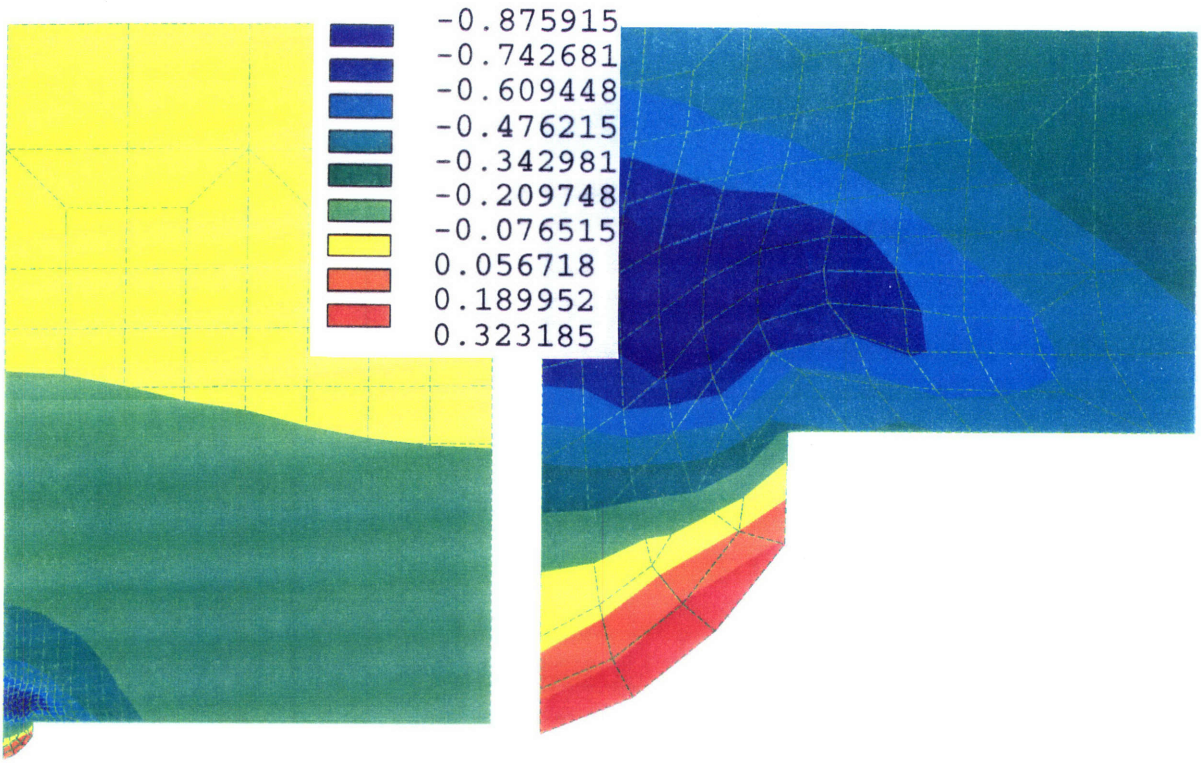

Figure 4.3.6 Cont'd. e) Exudation volumetric strain; P = 0.3916 bar (full view and close-up at the hole).

- **Imbibition**

The imbibition results are shown in Figure 4.3.7. In this case the high peripheral velocity resulted in a corresponding area of maximal axial tensile strain and maximal radial compressive strain, although in this case, the compressive radial strain was relatively small. Furthermore, one patch of high radial tensile strain was observed near the periphery of the hole which had no corresponding presence in the case of exudation and which added to the overall tension. The volume of matrix above the hole was in axial compression, but again, the tensile hoop and to a lesser extent the tensile radial strains acted to balance this compression. The strain above the hole together with the high peripheral axial tensile strain resulted in a tensile volumetric strain as shown in Figure 4.3.7.e, which acted to expand the matrix and decrease the resistance to flow.

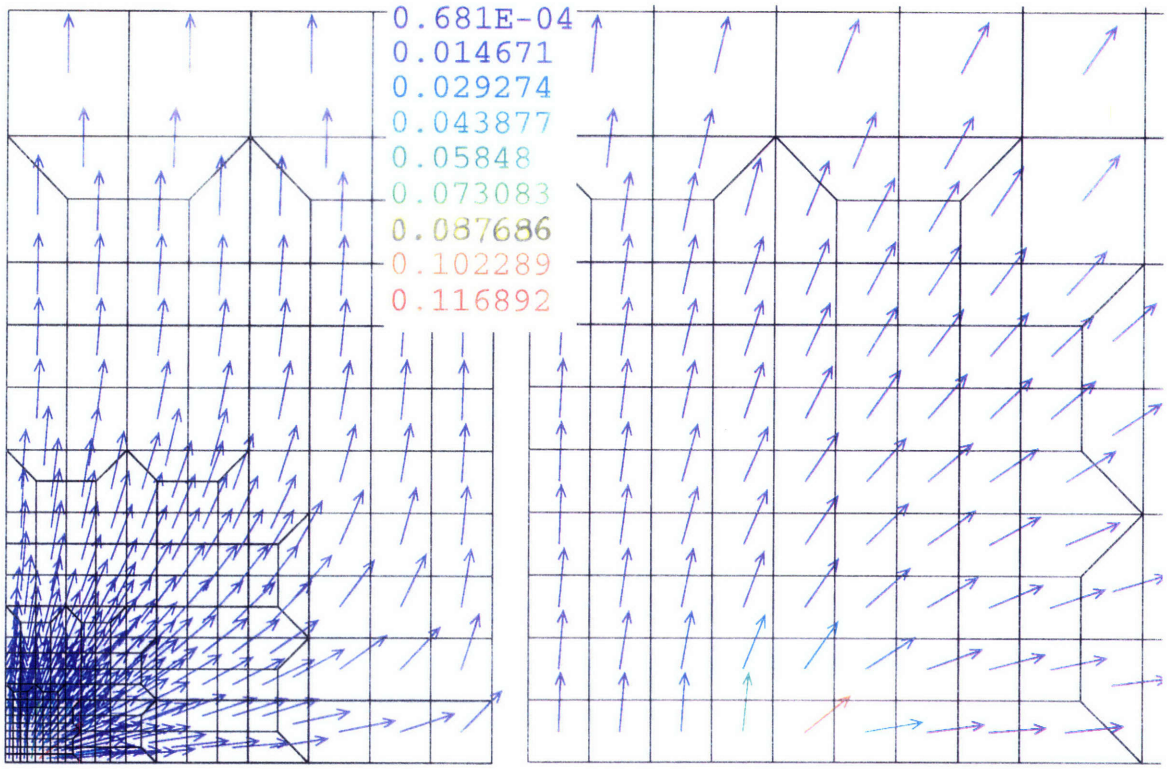

Figure 4.3.7. a) Imbibition velocity (m/s); P = 0.3916 bar (full view and close-up at the hole).

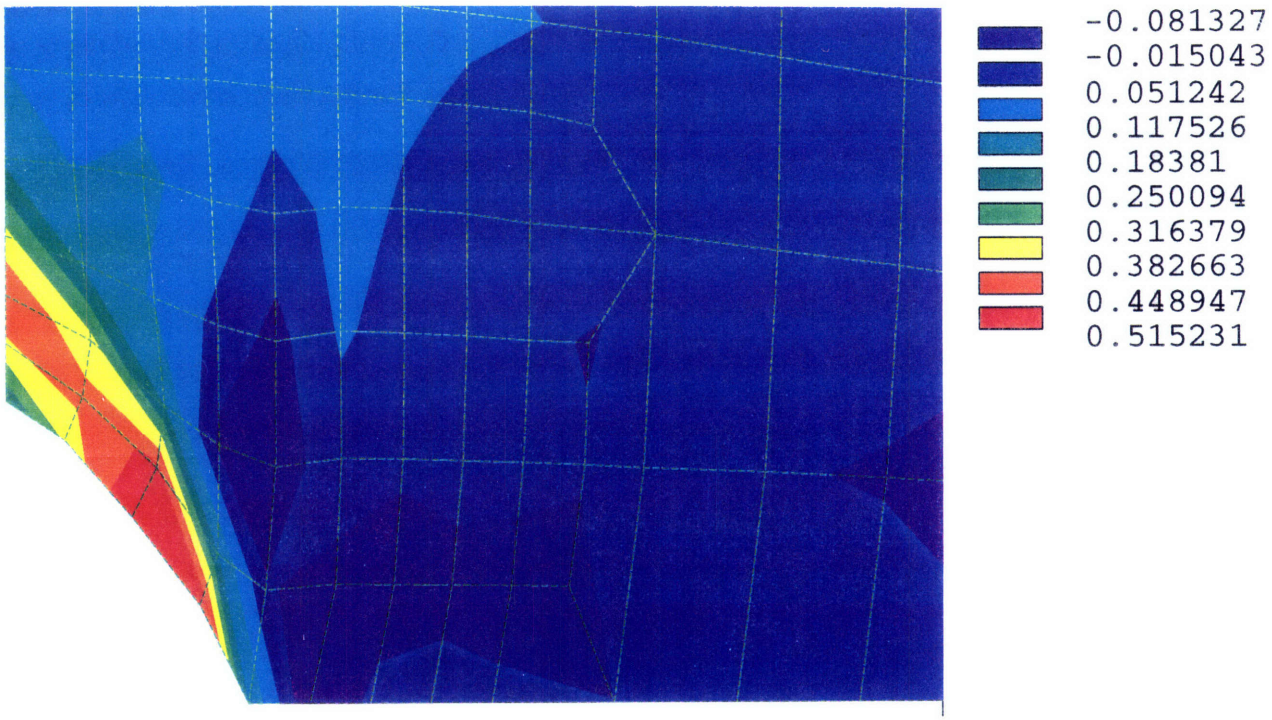

Figure 4.3.7 Cont'd. b) Imbibition radial strain at the hole; P = 0.3916 bar.

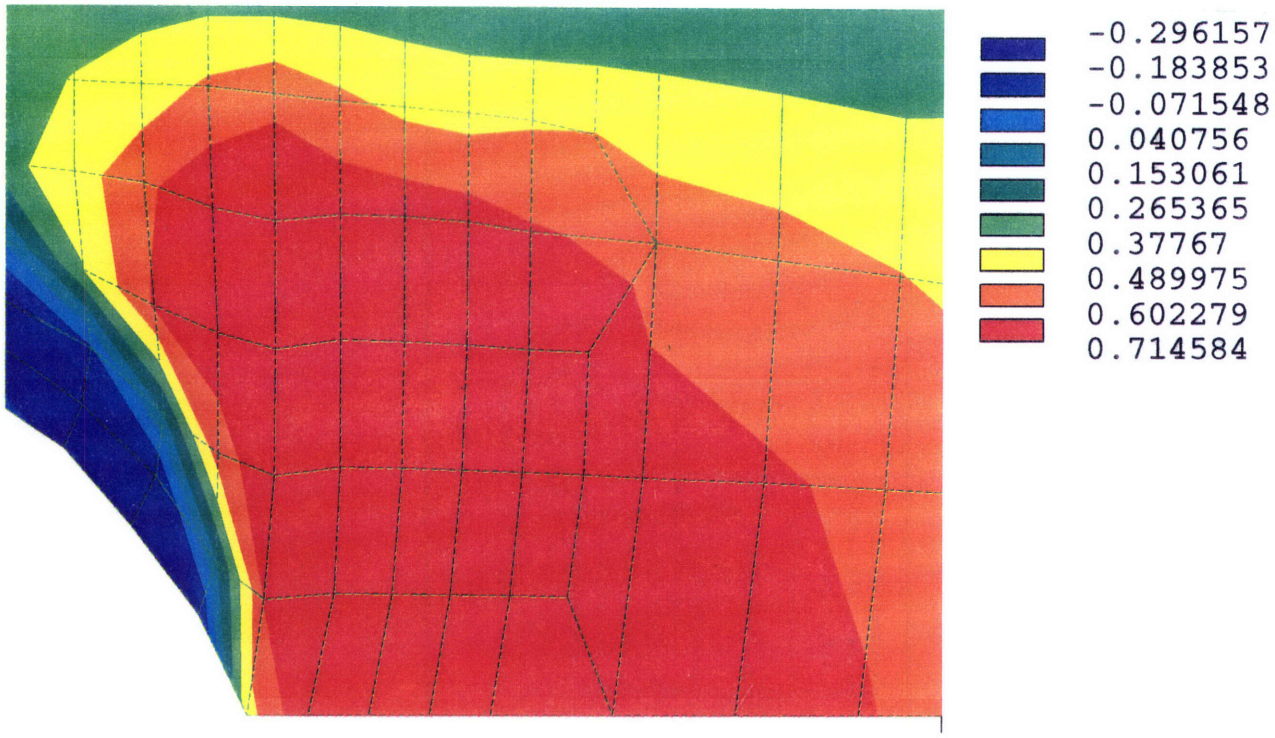

Figure 4.3.7 Cont'd. c) Imbibition axial strain at the hole; P = 0.3916 bar.

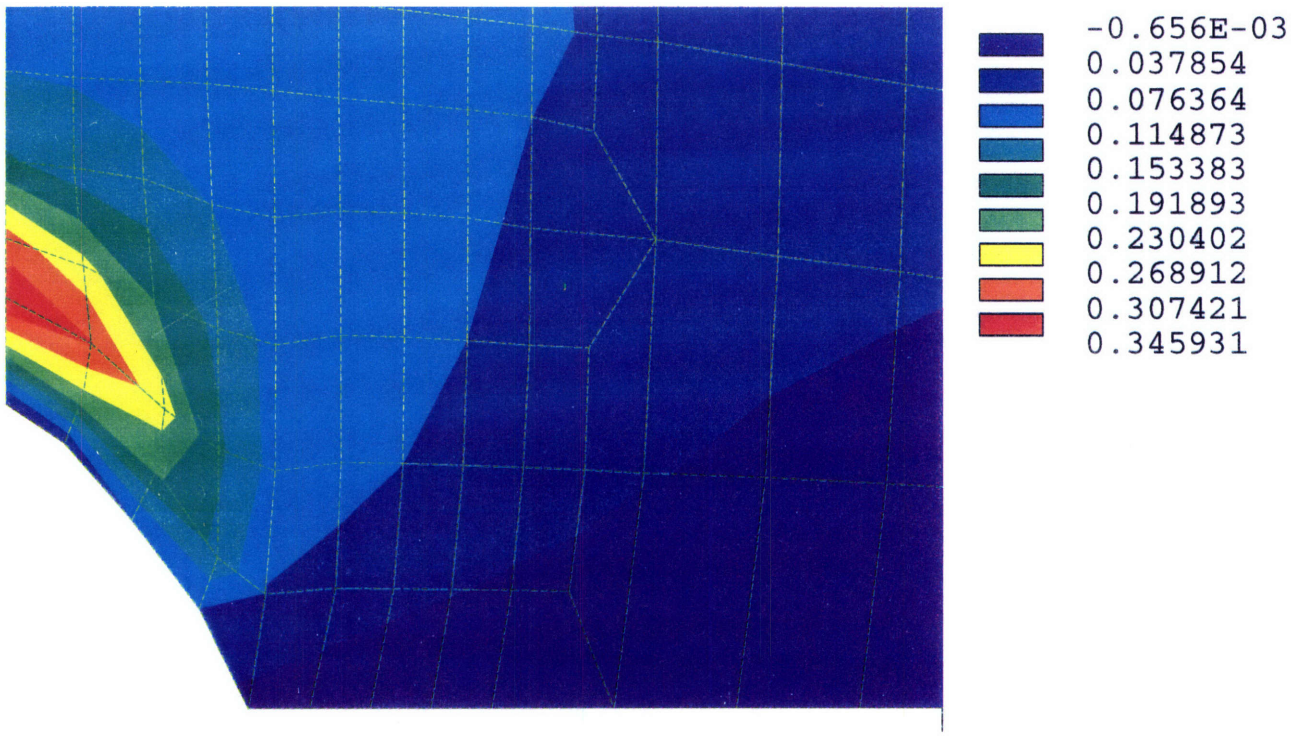

Figure 4.3.7 Cont'd. d) Imbibition hoop strain at the hole; P = 0.3916 bar.

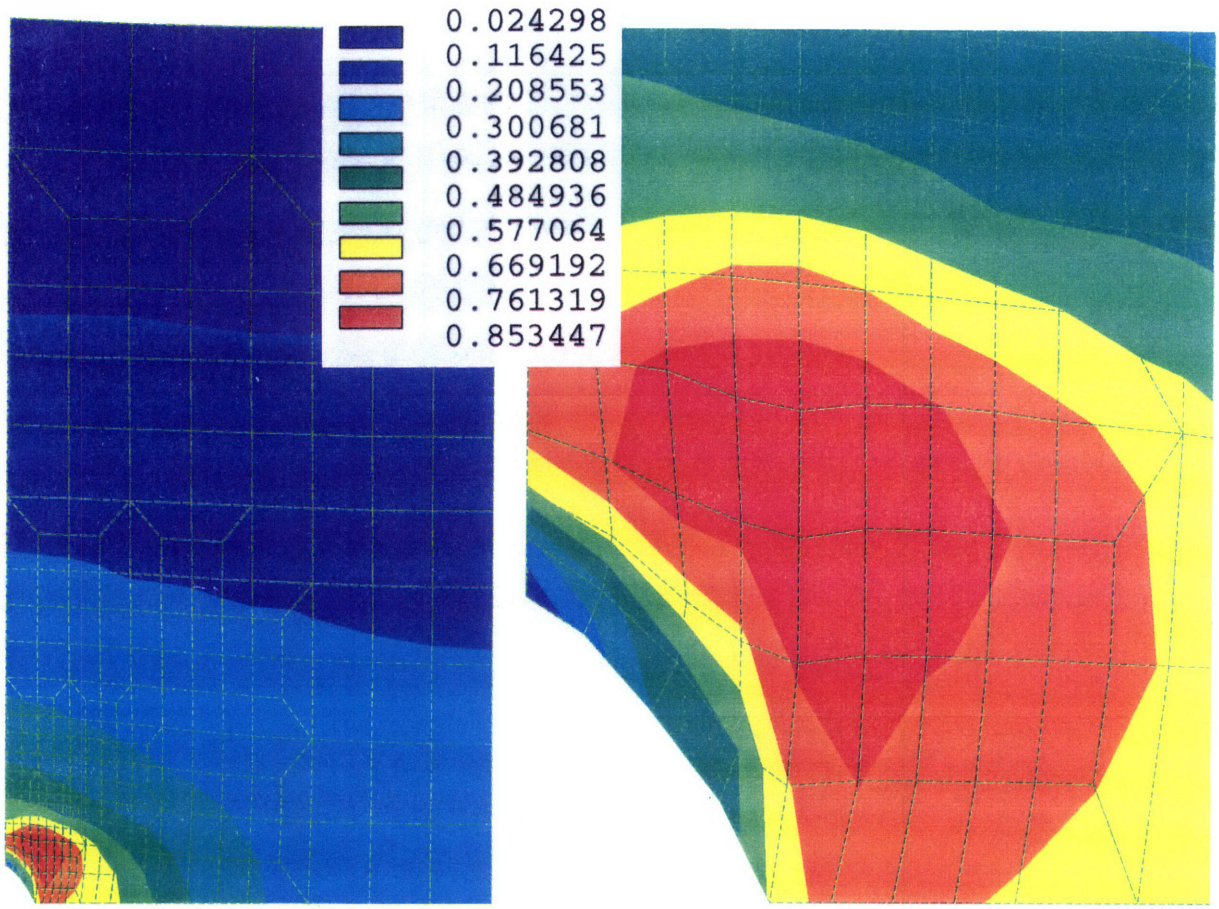

Figure 4.3.7 Cont'd. e) Imbibition volumetric strain; P = 0.3916 bar (full view and close-up at the hole).

4.3.5 PERMEABILITY VARIATION

The contour plot of derived element absolute permeability in the PORO model for the final iteration of exudation and imbibition at an applied pressure of 0.3916 bar are shown in Figures 4.3.8 and 4.3.9. The variation in magnitude of the permeability and applied nodal forces corresponded to the velocity and strain distributions as shown in Figures 4.3.6 and 4.3.7. High forces were observed at the periphery of the hole at high applied pressures, which resulted in extreme deformations of the elements. The exudation permeability was observed to be low through a large volume around the upper periphery of the constriction hole, but remained relatively high through the small volume directly above the hole. During imbibition, the lowest permeability was found across and just above the center of the hole. However, a high gradient toward the outside of the hole resulted in a very high permeability at the periphery. The permeability was also relatively high throughout the lower half of the foam (relative to the permeability at the center of the hole).

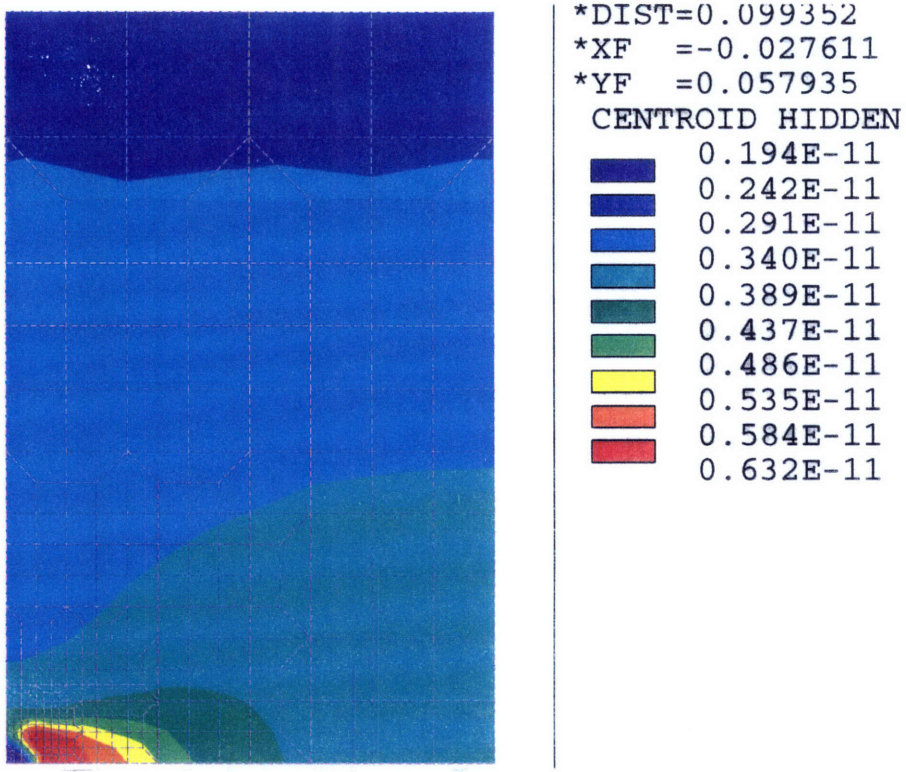

Figure 4.3.8 Exudation permeability contour ($m^5/kg \cdot s$) ; final iteration, P = 0.3916 bar.

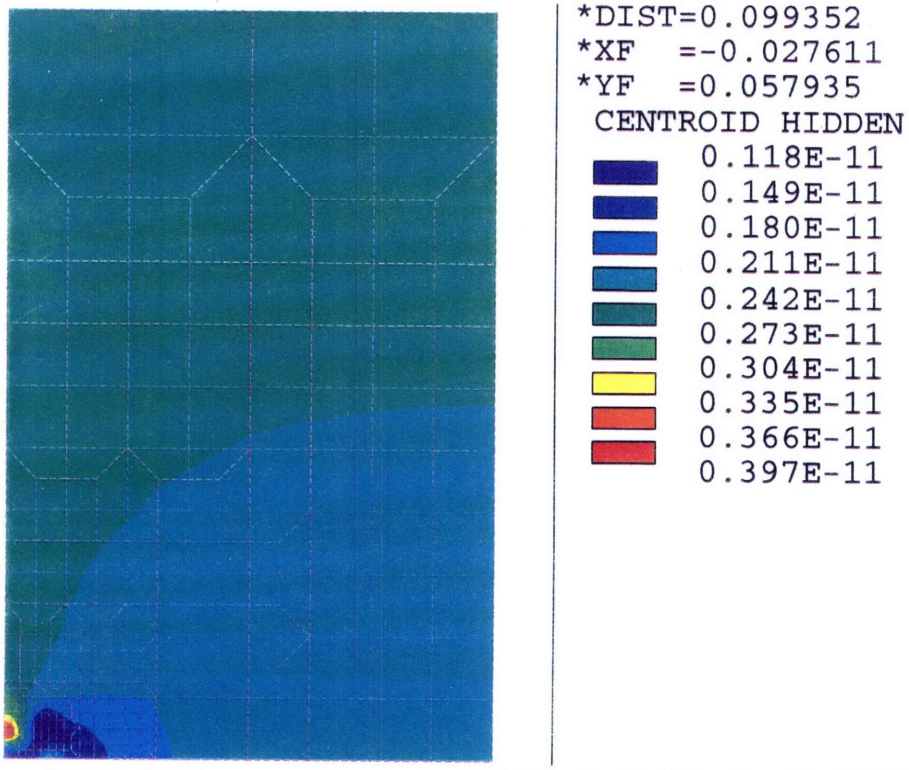

Figure 4.3.9 Imbibition permeability contour ($m^5/kg \cdot s$) ; final iteration, P = 0.3916 bar.

4.3.6 FLUID PRESSURE

Contour plots of the variation in pressure at the hole in the PORO model for exudation flow an imbibition flow are shown in Figures 4.3.10.a and 4.3.10.b at an applied pressure of 0.3916 bar.

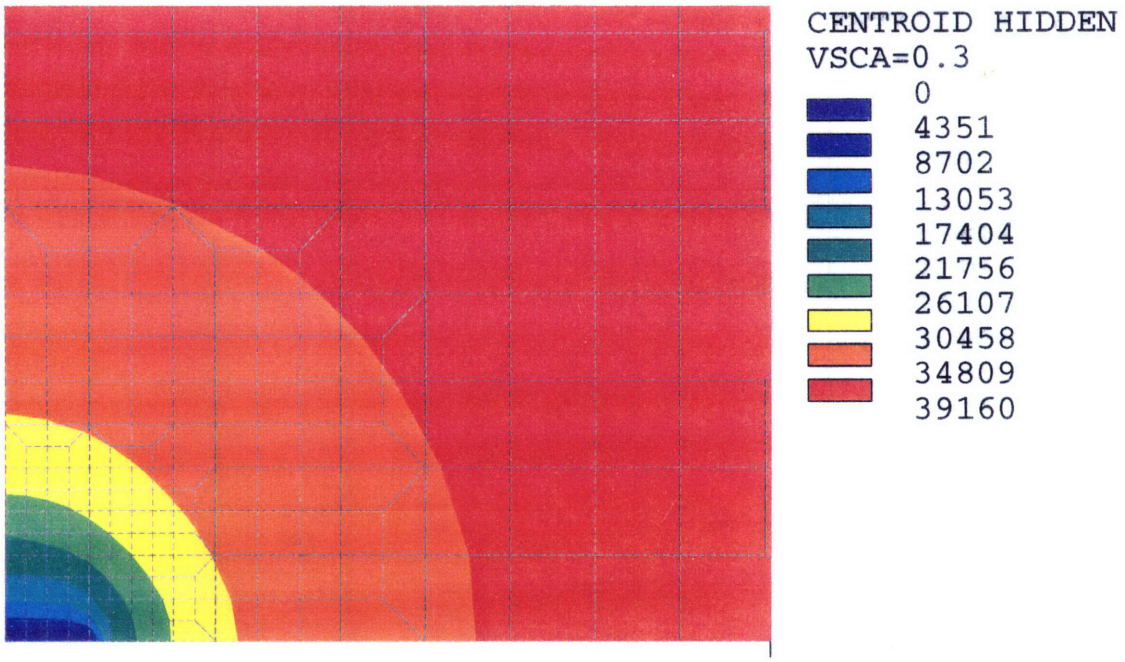

Figure 4.3.10.a Exudation pressure distribution at the hole; P = 0.3916 bar.

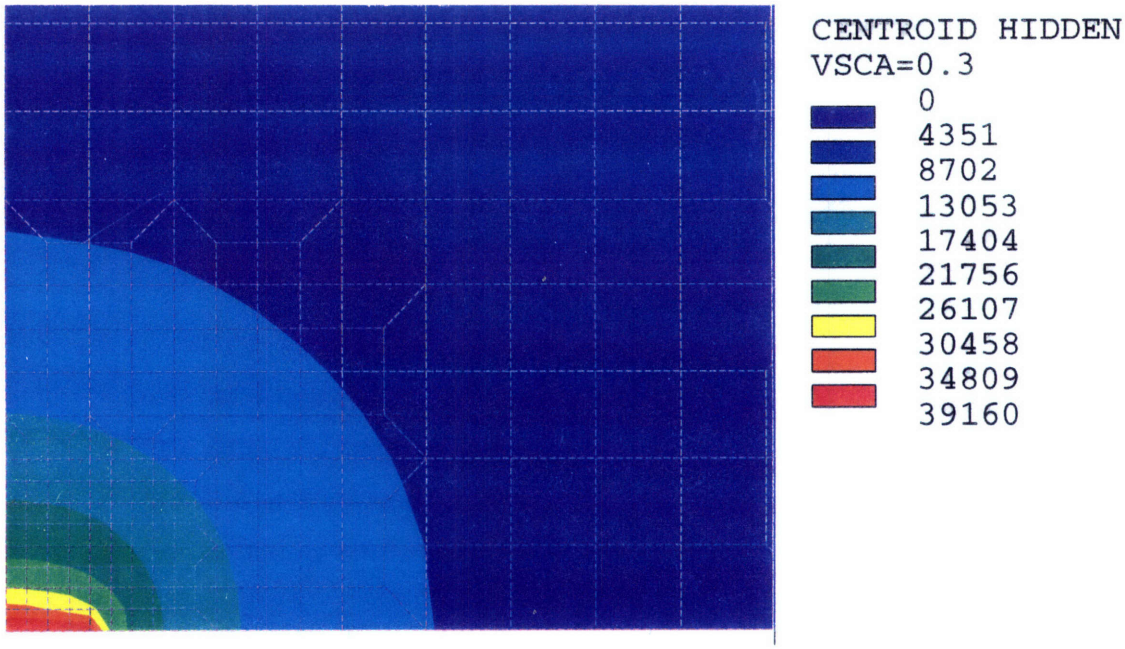

Figure 4.3.10.b Imbibition pressure distribution at the hole; P = 0.3916 bar.

4.3.7 MESH CONVERGENCE STUDY

The graphical solutions of the refined mesh models (Model 2 and Model 3) are not shown here for brevity; the solutions were similar to those shown in Figures 4.3.6 and 4.3.7, while the contours were somewhat smoother due to the finer meshes. The final numerical solutions of the flow rate of the three models are listed in Table 4.3.1. The "Difference" columns show the percentage change in the flow rate between consecutive models with respect to the previous model. For example, the "Q_{out} Difference" value for Model 2 at a pressure of 0.0916 bar was found from the calculation

$$\frac{Q_{out}|_{mod10} - Q_{out}|_{mod8}}{Q_{out}|_{mod8}} \tag{4.13}$$

$$= \frac{0.473 \times 10^{-6} - 0.417 \times 10^{-6}}{0.417 \times 10^{-6}} = 0.134.$$

The values in the table show decreasing Difference values as the number of elements increases.

Pressure (bar)	**Model**	Number of Elements	Q_{out} (m^3/s)	Q_{in} (m^3/s)	**Difference Q_{out} (%)**	**Difference Q_{in} (%)**
0.0916	**1**	256	0.417 E-06	0.419 E-06	—	—
	2	580	0.473 E-06	0.491 E-06	**13.4**	**17.2**
	3	1528	0.511 E-06	0.522 E-06	**8.0**	**12.4**
0.3916	**1**	256	1.30 E-06	2.33 E-06	—	—
	2	580	1.48 E-06	2.72 E-06	**13.8**	**16.7**
	3	1528	1.63 E-06	3.08 E-06	**10.1**	**13.2**

Table 4.3.1 Change in Flow Rate with Mesh Refinement

The refinement of the mesh did not appear to cause the solution to approach that of the physical experiment as was expected. Table 4.3.2 lists the "Difference" values, which in this case are those between the finite element model values and the experimental data. However, there did not appear to be any pattern in the Difference values with increased mesh refinement. Furthermore, only two refinements were performed at only two different pressures and it is therefore not possible to draw any conclusions about this trend for all pressures and further mesh refinements.

Pressure (bar)		Q_{out} (m^3/s)	Q_{in} (m^3/s)	**Difference Q_{out} (%)**	**Difference Q_{in} (%)**
0.0916	**Experiment**	0.428 E-06	0.487 E-06	—	—
	Model 1	0.417 E-06	0.419 E-06	**-2.6**	**-14.0**
	Model 2	0.473 E-06	0.491 E-06	**10.5**	**0.8**
	Model 3	0.511 E-06	0.552 E-06	**19.4**	**13.3**
0.3916	**Experiment**	1.49 E-06	2.66 E-06	—	—
	Model 1	1.30 E-06	2.33 E-06	**-12.8**	**-12.4**
	Model 2	1.48 E-06	2.72 E-06	**-0.67**	**2.3**
	Model 3	1.63 E-06	3.08 E-06	**7.37**	**15.8**

Table 4.3.2 Percent Difference in Flow Rate with respect to the Experimental Data

4.3.8 SIMULATION OF ENDPLATE CALCIFICATION

- **Change in the Size of the Hole**

As the radius of the constriction hole was increased from 2 mm to 7 mm at an applied pressure of 0.3916 bar both the absolute exudation resistance and the absolute imbibition resistance decreased, as shown in Figure 4.3.11. However, the ratio of exudation resistance to imbibition resistance increased slightly from 1.8 to 2.0.

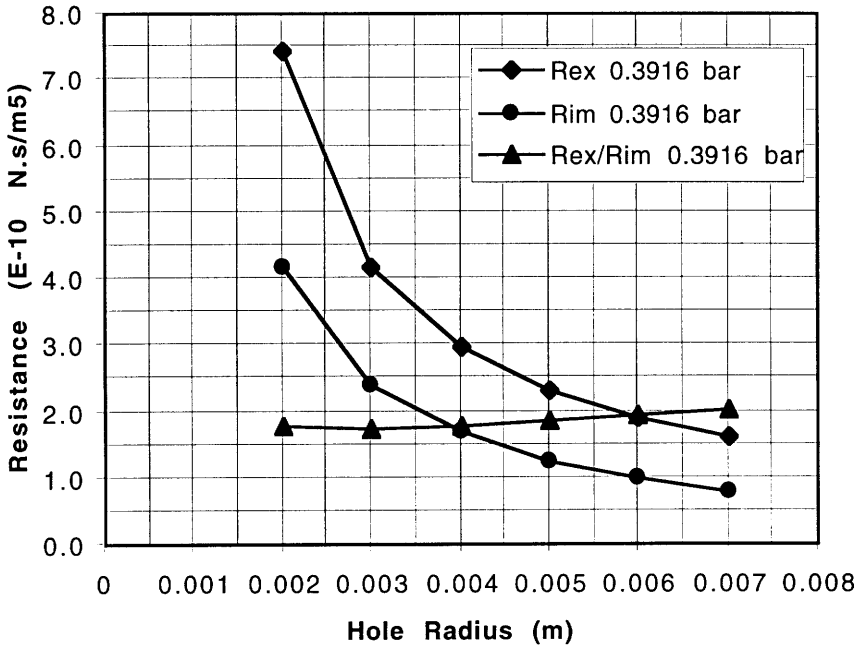

Figure 4.3.11 Change in resistance with increasing draining hole radius.

- **Change in the Number of Holes**

Figure 4.3.12 shows the change in the absolute resistances as well as in the resistance ratio with an increasing draining radius (r_{drain}) of the foam at two different applied pressures. The values of resistance were normalized according to the constriction hole area to draining area ratio of Model 1, as explained in Section 4.2.

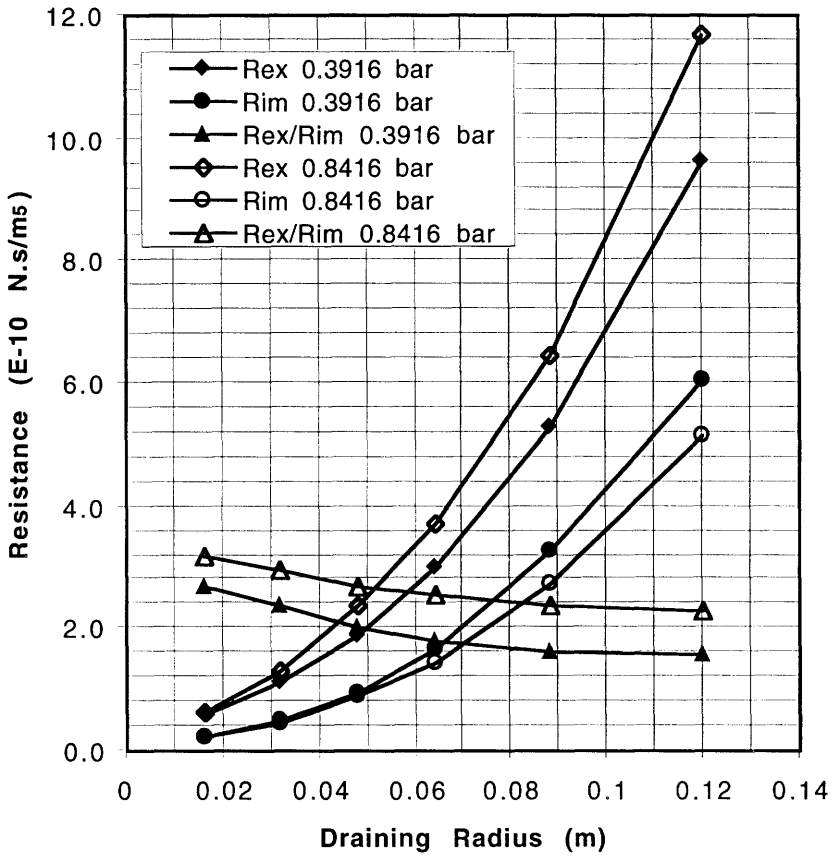

Figure 4.3.12 The effect of increasing the draining area on exudation resistance (R_{ex}), imbibition resistance (R_{im}) and the ratio of R_{ex} to R_{im} for flow through a constant 4 mm radius hole (finite element simulation).

The absolute resistances were found to increase with an increase in the draining area, while the resistance ratio was found to decrease slightly. The exudation resistance as well as the imbibition resistance at small draining radii were approximately the same for the two applied pressures. As the draining area was increased, however, the exudation resistance at an applied pressure of 0.8416 bar was found to be higher than that at 0.3916 bar, while the imbibition resistance at an applied pressure of 0.8416 bar was lower. In both cases the difference between the two increased with an increase in the draining area. The resistance ratio was higher for an applied pressure of 0.8416 bar for all draining radii.

The contour plots of volumetric strain at the hole for the two extreme draining radii of 16 mm and 120 mm are shown in Figures 4.3.13 and 4.3.14 respectively, for imbibition and exudation flow.

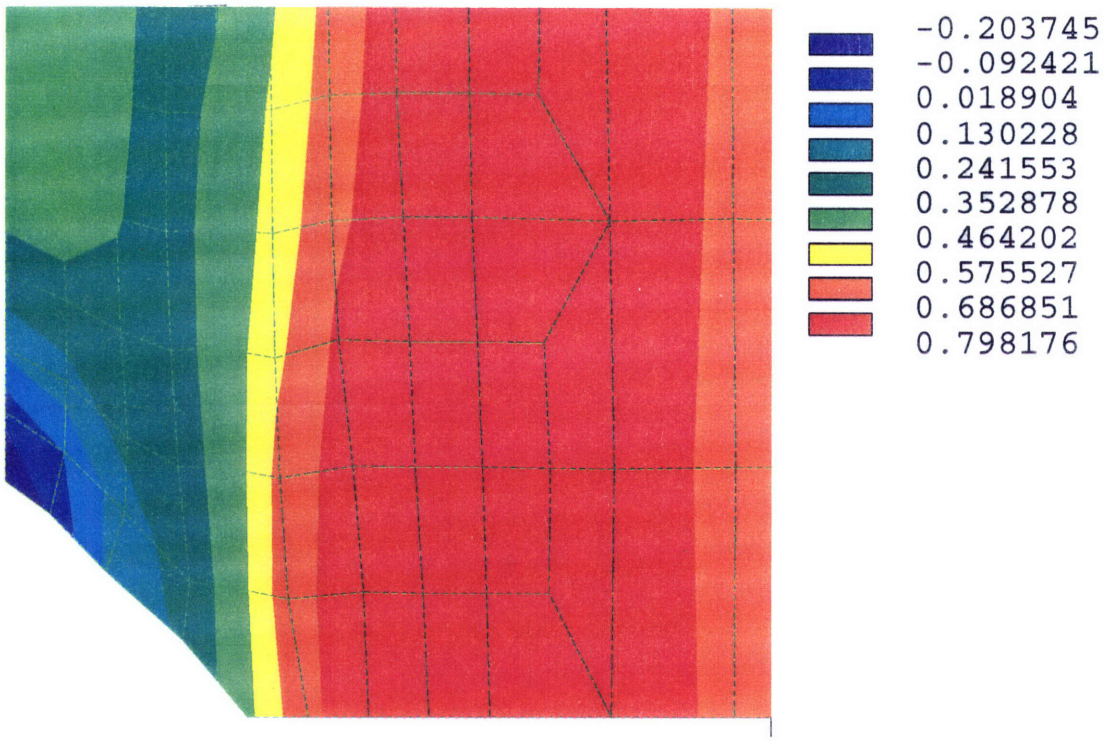

Figure 4.3.13.a Imbibition volumetric strain at the hole for a draining radius of 16 mm, P = 0.3916 bar.

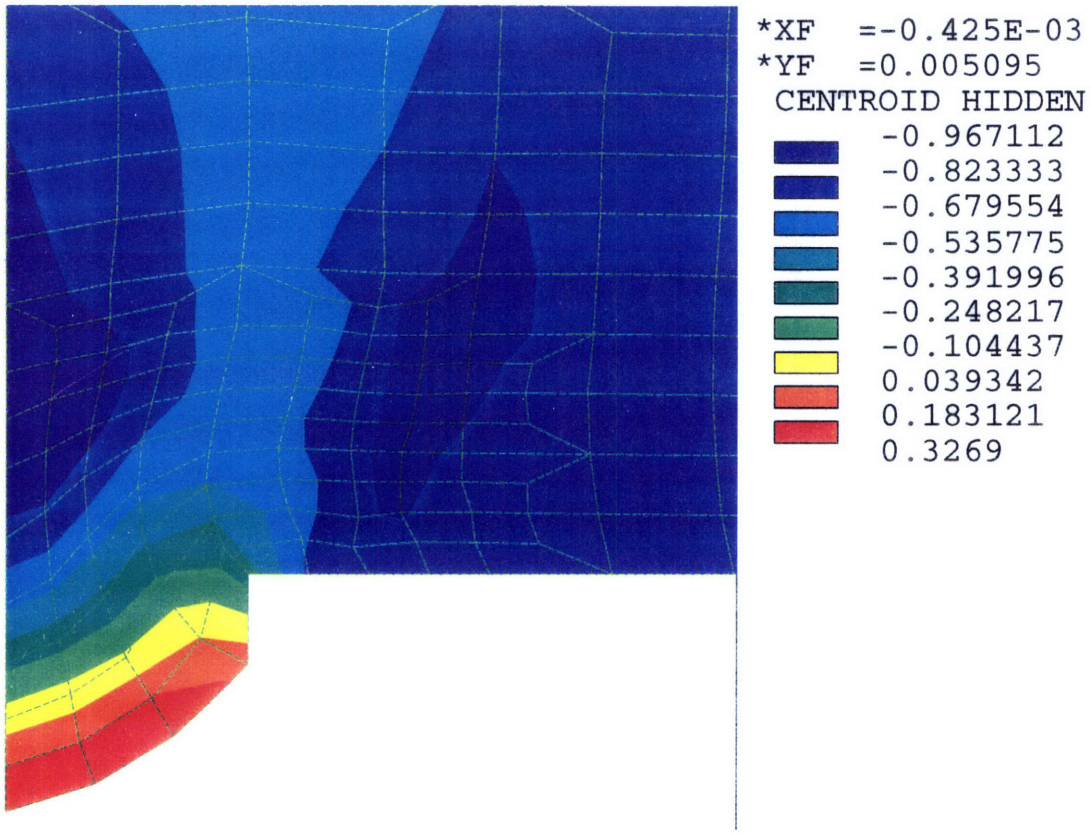

Figure 4.3.13.b Exudation volumetric strain at the hole for a draining radius of 16 mm, P = 0.3916 bar.

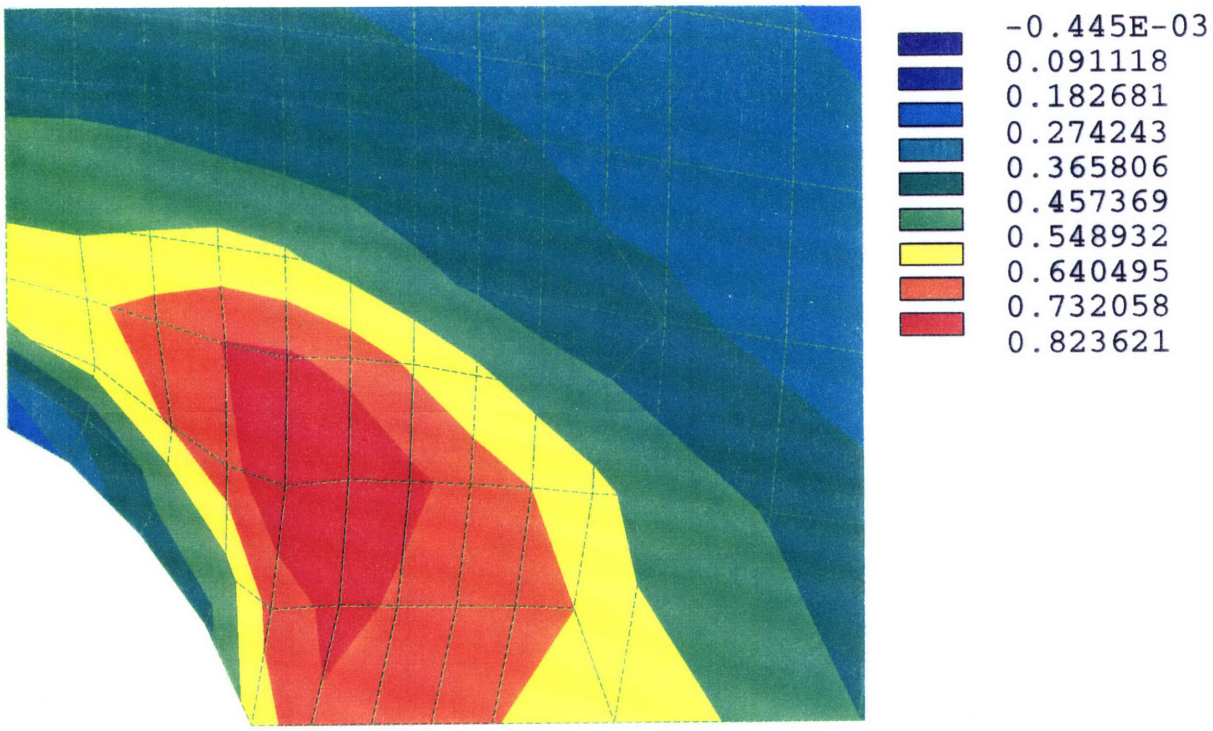

Figure 4.3.14.a Imbibition volumetric strain at the hole for a draining radius of 120 mm, P = 0.3916 bar.

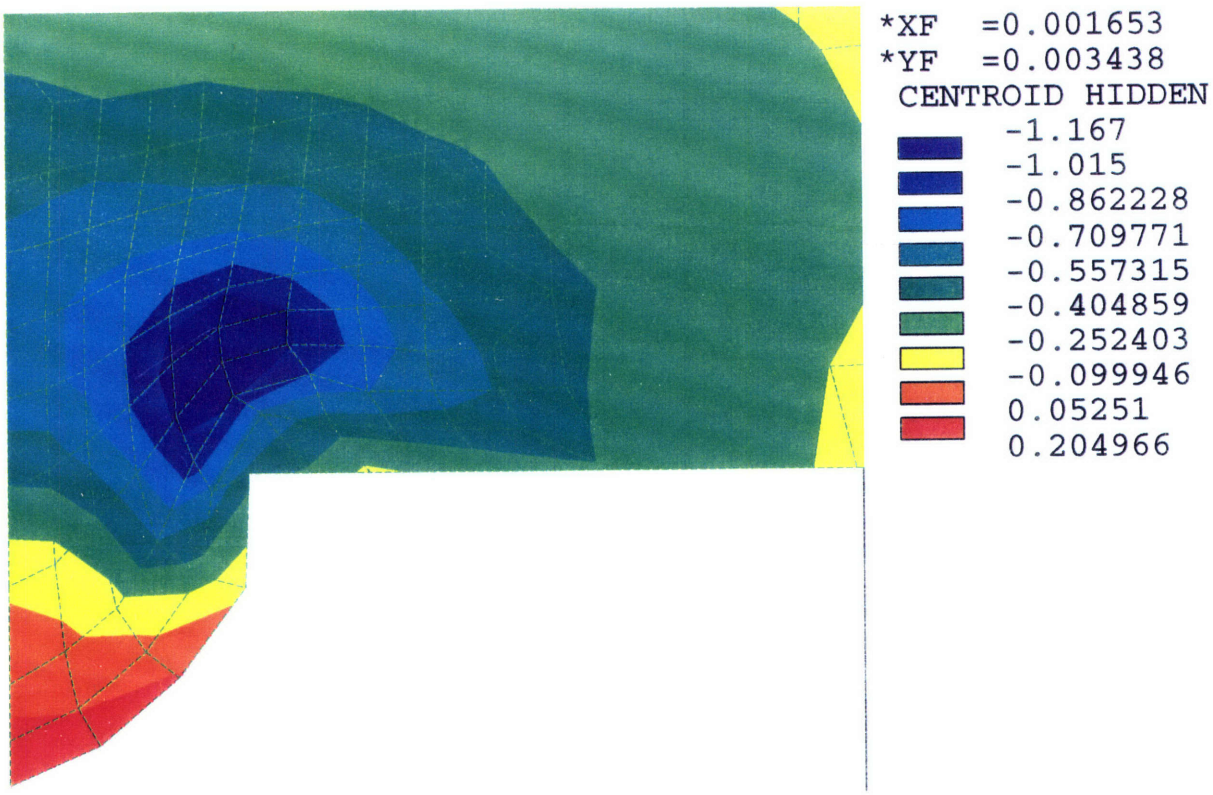

Figure 4.3.14.b Exudation volumetric strain at the hole for a draining radius of 120 mm, P = 0.3916 bar.

• **Comparison of the Effect of a Change in Hole Size and a Change in Number of Holes**

In order to directly compare the effects of a change in the hole size and a change in the total number of holes, both sets of data were plotted against the fraction of constriction hole area to foam draining area as shown in Figures 4.3.15 and 4.3.16. The behavior in each case was found to be the same; i.e. the percentage change in the absolute resistances and the resistance ratio, within error, depended only on the fraction of hole area to draining area. The data for the number of holes was normalized with respect to the hole area fraction of Model 1, thus, the absolute values of the imbibition and exudation resistances in each case are the same within error. However, regardless of the base value used for normalization, it is the percentage change in the absolute resistances and the resistance ratio which are of interest.

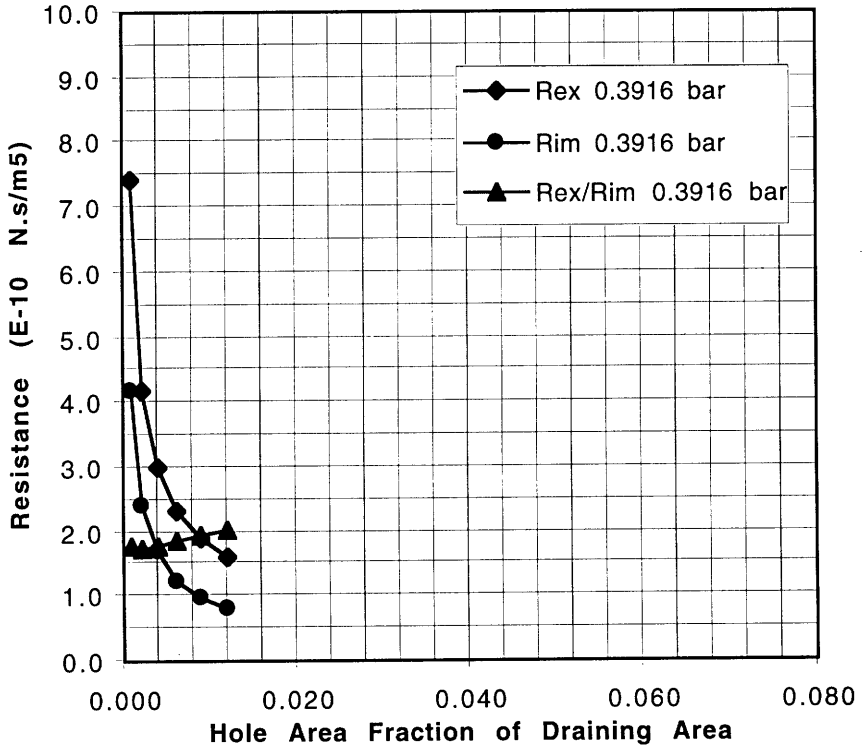

Figure 4.3.15 Change in exudation resistance, imbibition resistance and the resistance ratio with respect to the fraction of constriction hole area to draining area. Here the draining area was kept constant while the constriction hole area was increased. Scale was chosen for comparison with Figure 4.3.16.

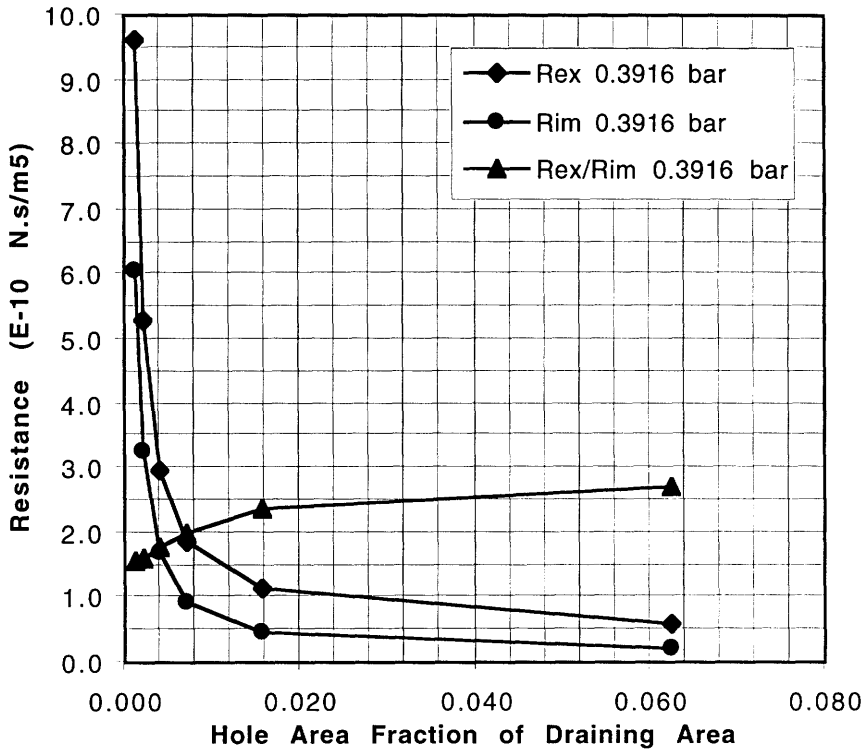

Figure 4.3.16 Change in exudation resistance, imbibition resistance and the resistance ratio with respect to the fraction of constriction hole area to draining area. Here the constriction hole area was kept constant while the draining area was decreased.

4.4 DISCUSSION

4.4.1 MODEL VALIDATION

The imbibition and exudation resistances calculated with finite element analysis were consistently greater than those measured experimentally, as shown in Figure 4.3.3. The FE offset is most likely due to transient effects in the physical model. The finite element solution models the steady state condition, and it is possible that in the physical model experiment, the flow, and therefore the strain, had not reached steady state at the time of measurement. This would account for a lower measured resistance in the case of exudation flow since the matrix would not have reached full compression. It could also be the cause of a lower resistance during imbibition, since some further local compression of the matrix at the hole periphery at steady state, as demonstrated with the FE model, could result in a decrease in resistance.

In the case of imbibition flow, the offset was reduced to approximately zero at high applied pressures. This suggests that transient effects for imbibition flow were minimal at high applied pressures, which was probably due to the high tensile strain in the matrix and resulting high stiffness, which would limit any further strain and resulting decrease in resistance. The offset also decreased to a lesser extent for exudation flow at high applied pressures, which would suggest that the transient effects in general were smaller at higher flow rates.

The direction-dependency of the resistance appeared to begin at a lower applied pressure in the physical model. That is, the exudation and imbibition resistance curves split at a lower applied pressure than in the finite element model. The less pronounced non-linear effects at low applied pressures in the finite element model could be due to some error introduced by the stress-strain curve at low strains. Certainly some of the overall offset in the curves was due to error in both the physical model measurements as well as inaccuracies in the finite element model solution.

The change in the ratio of R_{ex} to R_{im} of the FE model followed the behavior of the physical model closely as shown in Figure 4.3.5. At low applied pressures the FE model ratio was slightly lower than that of the physical model while at high applied pressures the FE ratio surpassed that of the physical model by a small amount. These results combined with those of the absolute resistance value offsets demonstrated in Figure 4.3.3 and 4.3.4 indicate that

any transient effects in the physical model (which probably resulted in the absolute resistance offsets) had little effect on the resistance ratio.

4.4.2 FLOW AND STRAIN DISTRIBUTION

The highest velocity and corresponding strain were found at the periphery of the hole, not in the volume of matrix directly above the hole as was expected (see Figures 4.3.6 and 4.3.7). In addition, during exudation a large volume of the matrix above the hole was actually in axial tension, and likewise during imbibition compressive axial strain was observed above the hole. This may be in part due to bulging of the foam through the hole during exudation, stretching the matrix above the hole. This effect may be more pronounced in the FE analysis as friction against the side wall of the hole was not modeled. Friction in the physical model could reduce the bulging, but because the contact between the foam and wall of the hole is likely to be minimal, the FE model probably represents the physical situation accurately. The strain distribution around the hole appears to be qualitatively realistic and despite these unexpected reverse strain conditions, exudation resulted in dominant compressive strain behavior and imbibition in dominant tensile strain behavior such that the hypothesized direction-dependent resistance was observed.

Quantitatively, the deformation of the foam at the hole (outward bulging during exudation and inward stretching during imbibition) appeared to be somewhat exaggerated, particularly at high applied pressures. The displacement results could not be validated since it was not possible to observe the deformations at the hole in the physical model during exudation or imbibition due to the model design (see Chapter 3). This observation could be attributed to the use of large strain analysis combined with the non-linear stress-strain curve for two reasons. First, the extreme strain at the periphery of the hole caused the elements to become highly distorted, inducing an error in subsequent load step calculations through the use of large strain analysis. Second, due to the nature of the stress-strain curve high strains were reached quickly during the initial load steps. A large strain increment in one substep may have caused the solution to underestimate the stiffness and overshoot the stress-strain curve, resulting in a higher strain and a possible accumulation of strain error with each substep.

4.4.3 PERMEABILITY DISTRIBUTION

Some unexpected results were also found for the corresponding permeability distribution. In particular, during exudation the maximum permeability was found in a small volume of the matrix above the hole, as shown in Figure 4.3.8, while during imbibition, the minimum

permeability was found at the center of the hole, as shown in Figure 4.3.9. These reverse effects were due to the local expansion and consolidation of the matrix above the hole as discussed previously. However, very low permeabilities were encountered in the region surrounding the hole during exudation, and a high permeability gradient was found at the periphery of the hole during imbibition resulting in maximum permeability at the hole circumference. Thus, despite the reverse effects, during exudation an overall decrease in permeability was observed, while during imbibition an overall increase in permeability was observed such that the hypothesized direction dependent effects were demonstrated.

4.4.4 SIMULATION OF CARTILAGE ENDPLATE CALCIFICATION

From the flow pattern observed at the hole it is clear that, in a model with multiple holes, this pattern would depend on the number and overall spatial distribution of the constriction holes. As shown schematically in Figure 4.4.1, a decrease in the number of holes results in an increase in the draining area of each hole.

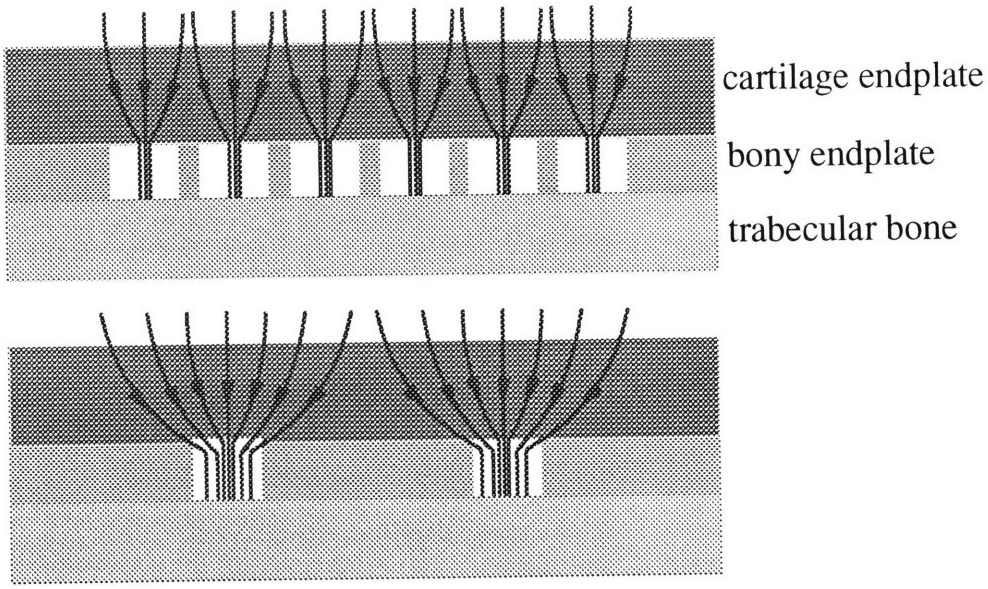

Figure 4.4.1 A decrease in the total number of holes results in an increase in the draining area of each hole.

The SEM images of the human bony endplates in Chapter 2 show how calcification of the cartilage endplate can result in a deposit on the surface of the bone which reduces the size of the constriction holes, and eventually the total number of holes, as some become completely covered while others remain partially or fully open. Thus, the effects of such decreases in the

size and number of the constriction holes in the physical model were simulated in order to gain some insight into the same effects *in vivo*, and to prove or disprove the hypotheses made about these effects from the results of the physical model, as discussed in Chapter 3.

In the first case, investigating the effects of a change in the size of the constriction hole, it was hypothesized that a decrease in the size of the hole would result in an increase in exudation resistance and an increase in imbibition resistance, but not to the same extent, thus leading to a higher resistance ratio. Furthermore, it was hypothesized that as the number of holes decreased, the direction-dependent effect would be stronger, resulting in an increase in the resistance ratio of exudation to imbibition. The results shown in Figure 4.3.11 confirmed that the exudation resistance did rise with an increase in draining area. However, the imbibition resistance also rose, and the ratio of exudation resistance to imbibition resistance actually decreased with increasing draining area.

Consideration of these results led to the second case in which the effects of a change in the total number of holes were investigated. Again, it was hypothesized that with an increase in the draining area (i.e. a decrease in the number of holes) the exudation resistance would rise, as well as the resistance ratio. Again, as shown in Figure 4.3.12, only one of these hypotheses proved to be true, as both resistances rose with an increase in the draining area while the resistance ratio fell. Furthermore, a comparison of the two cases (change in hole size and change in hole number) showed that the effects were, in fact, the same. That is, the change in the absolute resistances and the value of the resistance ratio depended only on the constriction hole area fraction of the draining area, as demonstrated by comparison of Figures 4.3.15 and 4.3.16.

The rise in the exudation resistance with a decrease in the hole area fraction can be explained by the higher resulting exudation velocities and corresponding higher drag forces at the hole, resulting in greater consolidation of the matrix. The rise in imbibition resistance with a decrease in hole area fraction can possibly be explained by the local compression at the hole. A decrease in the hole area fraction in both cases (decrease in hole size and increase in draining area) resulted in an increase in the imbibition velocity at the hole as expected, and thus in higher tension at the hole periphery and higher overall tensile strain throughout the foam. However, the increase in tensile strain at the hole periphery was very small, and the local *compressive* strain across the lower surface of the hole increased, as shown by comparison of Figures 4.3.13 and 4.3.14, which resulted in a dominant compressive effect and consequent rise in resistance.

As shown in Figure 4.3.12, while the exudation resistance was higher for a higher applied pressure (0.8416 bar compared to 0.3916 bar) the imbibition resistance was lower. This is in contrast to the effect of a decrease in the hole area fraction, in which the imbibition resistance increased. A comparison of the strain at the hole for applied pressures of 0.3916 bar and 0.8416 bar showed an increase in the local compressive strain across the lower surface of the hole for a higher applied pressure, as is the case for a decrease in the hole area fraction (Figures 4.3.13 compared to Figure 4.3.14). However, there is an approximate two-fold increase in the tensile strain at the hole periphery with an increase in applied pressure, which did not occur with a decrease in hole area fraction. This increase in tensile strain caused the decrease in imbibition resistance with an increase in the applied pressure.

The unexpected decrease in the resistance ratio with a decrease in the hole area fraction could be explained by the rise in imbibition resistance. R_{im} rose faster than R_{ex} with a decrease in the hole area fraction, and therefore the ratio fell. An explanation for the decrease in the resistance ratio with decreasing hole area fraction could be due to the resistance of the hole itself, without any effects of the porous solid. That is, the total resistance to the fluid flow is due to the constriction hole alone (R_h), plus that due to the porous solid layer (R_{ps}), and is given by:

$R_{ps} + R_h$,

and the ratio of exudation resistance to imbibition resistance is therefore given by:

$(R_{ps,ex} + R_h) / (R_{ps,im} + R_h)$

since R_h is the same in both directions.

As the hole area fraction of the total draining area decreases, R_h increases. Thus, $R_{ps,ex}$ and $R_{ps,im}$ would become negligible with respect to R_h, and the ratio would approach R_h / R_h, or one [personal communication with N. Bishop].

Hole closing could be caused in the body by the calcification of endplate cartilage which would cover the holes and reduce the size and eventually reduce the total number of constriction holes in the bony endplate (see Chapter 2). The balance between the values of absolute imbibition resistance and exudation resistance and the resistance ratio plays an important role in the maintenance of healthy disc mechanics. From the results of the cartilage endplate calcification simulation, it can be concluded that the most efficient valve, i.e. the valve with the highest resistance ratio, would be that with an ideal support with an

infinite number of holes, since as the draining area became smaller and smaller and approached the area of the constriction hole, the ratio increased. However, at the same time the absolute resistances in and out decreased. If the exudation resistance became too low the disc would lose all of its fluid under normal daily loads and would simply collapse.

As the number of holes decreased (i.e. the draining area increased) in the finite element model, the absolute exudation and imbibition resistances at a given applied pressure increased. This would result *in vivo* in a lower daily amplitude of the disc height cycle and would therefore disrupt the normal volume of fluid exchanged in the disc. Furthermore, as the number of holes decreased the ratio approached one which resulted in a more linear valve which would mean that all of the fluid lost during daily loading would not be recovered during rest and the disc would eventually dehydrate. This net loss of fluid over time could result in the solid structures of the disc (nuclear and annular tissue or the apophyseal joints) supporting the daily loads on the spine.

A specific balance between the absolute resistances and the resistance ratio is necessary to maintain normal spine mechanics and healthy disc hydration. Any disturbance of this balance could result in disruption of the normal daily fluid flow exchange in the disc which could hinder the nutrient exchange process. Furthermore, excessive fluid loss from the disc may result in abnormally high loading of the solid structures of the disc. These effects could lead to various spinal disorders such as disc rupture, degeneration or dehydration. If this problem could be diagnosed in a patient with back pain (possibly using nuclear magnetic resonance imaging to determine the diurnal fluctuations in fluid content; the subject of a future study) surgical intervention could be performed to open up new holes through the calcified layer of cartilage and in the bony endplate. This procedure would allow the fluid to flow through new channels, thus returning the disc to its normal diurnal mechanical cycle.

4.5 SOURCES OF ERROR

While the values of exudation and imbibition resistance of the FE model at most pressures did not lie within the standard deviation of the experimental values, the resistance variation with applied pressure followed that of the experimental data extremely well. Some of the difference between the values can be attributed to various finite element modeling errors. First, the use of a curve-fit function to the experimental permeability vs. strain curve and its extrapolation into the tensile axis probably resulted in some inaccuracy. The experimental data itself contained some amount of human error and the process of curve fitting was an approximation to the available data. Second, the mesh refinement study showed that the mesh of Model 1 contained a considerable amount of discretization error, but in order to have a reasonable solution processing time at high applied pressures this courser mesh was used. Furthermore, it was necessary to set a rather coarse force convergence tolerance (10%) in order to ensure solution convergence within a reasonable time period.

Specific assumptions were made in the finite element model in order to either simplify the solution, or because of certain limitations of the ANSYS software, and are described in the following sections.

- **Permeability of a Poroelastic Solid**

The absolute permeability of a porous solid as discussed previously and described by Equation 4.8 depends on the cellular parameters of the material, and for a "regular" porous solid such as polyurethane foam the permeability depends particularly on the average pore size and porosity of the matrix [5]. When attempting to define the relationship between absolute permeability and strain on the matrix, it is difficult to separate these parameters into directional components. For a given cylindrical porous solid, axial compressive strain will result not only in a decrease in the axial permeability, but also in a decrease in the radial permeability due to collapse of the pores which causes increased shear on the fluid, as shown in Figure 4.5.1. Furthermore, such compressive axial strain may result in local tensile radial strains. However, these tensile strains would also result in a decrease in permeability, as shown in Figure 4.5.1. Thus, one must consider the dependence of absolute permeability on the volumetric strain of the matrix, since a compressive volumetric strain would result in an overall decrease in pore size, and a tensile volumetric strain in an overall increase.

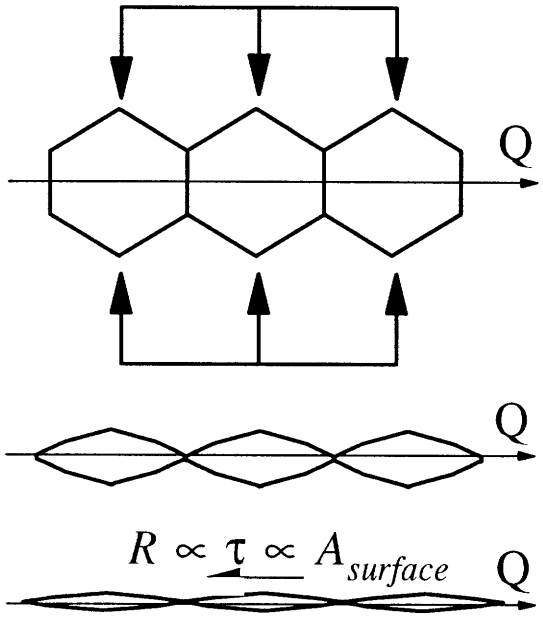

Figure 4.5.1 Axial compressive strain will result not only in a decrease in the axial permeability, but also in a decrease in the radial permeability due to collapse of the pores, which causes an increase in the shear stress on the fluid.

The experimental permeability test for the physical model determined the axial permeability vs. the confined axial compression of the foam. However, because the strain was axially confined, the overall axial strain measured was equal to the overall volumetric strain. Furthermore, assuming a "regular" poroelastic material, the change in radial permeability with volumetric strain should be the same as the change in axial permeability measured (i.e. isotropic permeability can be assumed). Thus, the experimentally determined curve can be taken as one of volumetric strain vs. axial and radial permeability.

In the finite element model, an initial attempt was made to determine the absolute permeability of the elements in the PORO model according to the derived volumetric strain of the SOLID model. However, it was found that solution convergence between the PORO and SOLID models was extremely slow and incomplete within the iterations attempted. A second attempt used the axial strain alone to determine permeability (i.e. the axial strain was taken as volumetric strain thus neglecting the radial and hoop components) and this resulted in much faster and more complete convergence. A comparison was then made at three different applied pressures between the flow rate solutions using volumetric strain and those using axial strain alone, and while the volumetric strain solutions in some cases did match the experimental results more closely, the difference between the solutions was found to be only 3% on average. Therefore the axial strain alone from the SOLID model was used to

determine both axial permeability and radial permeability in the PORO model, and this approximation combined with the curve fitting of the K_{∞} vs. ε curve probably contributed to the overall solution error.

- **Element Type**

The use of elastic elements in the SOLID model, as opposed to viscoelastic or hyperelastic elements which are more accurate at large strains (>50%) [2], was necessary in order to allow specific definition of the experimentally determined stress-strain curve. The viscoelastic and hyperelastic elements both utilize pre-defined functions with user-defined parameters to describe the stress-strain behavior. These functions were not appropriate for polyurethane. Some inaccuracy was therefore introduced into the model since strains greater than 50% were often encountered in the proximity of the constriction hole.

The use of poroelastic elements as opposed to splitting the model into one of flow and one of structure would be likely to have resulted in a more accurate final solution since with the paired model error is introduced in both the PORO and the SOLID model. However, the poroelastic elements now available with ANSYS version 5.2 do not allow a strain-dependent permeability function to be defined. Therefore, it would still have been necessary to perform an iterative solution in which the element permeabilities were adjusted according to the strain until convergence was attained.

- **Symmetric Stress-Strain Curve**

The stress-strain curve of a poroelastic material is asymmetric. The tensile stress-strain behavior of the physical model material was not tested, however, the tensile properties of a foam can be deduced from its compressive properties. The initial small-strain linear elastic modulus of a foam is the same as that in compression [5] and is provided by cell edge bending. At strains of more than a few percent the tensile stiffness of the foam begins to rise steeply. The plateau which exists in the compressive stress-strain curve due to cell wall buckling is not possible in tension, since at low strain the walls begin to rotate inwards, become aligned and begin to stretch as shown in Figure 4.5.2. The initial stiffness is dominated by the behavior of the inward bending of the cell walls, but once these walls are aligned the stiffness rises further as they are stretched axially.

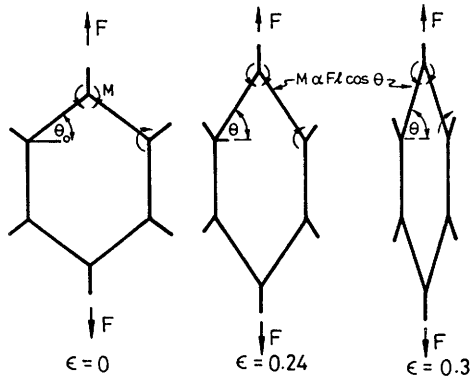

Figure 4.5.2 Alignment of the cell edges during tensile loading (from Gibson and Ashby [5]). At low strain the cell walls of the foam rotate inwards, then become aligned and begin to stretch.

It was not possible in ANSYS, using the multi-linear elastic stress-strain curve option, to define an asymmetric stress-strain curve. By assuming a symmetric curve and using that of compression, the tensile strains in the matrix were higher than they would have been experimentally due to the plateau which exists only in the compressive stress-strain curve. This probably resulted in a lower flow resistance during exudation as well as during imbibition and therefore would not have affected the overall direction-dependent effects, but did contribute to the error in the experimental data and could possibly have contributed to the offset observed in Figure 4.3.3.

- **Mesh Convergence Study**

The Difference values listed in Table 4.3.1 give an indication of how close the model mesh is to that of an "ideal" solution (infinite number of elements) and therefore also allow an approximation of the discretization error of the model. The difference value is the percentage change in the flow rate between consecutive models (increasing mesh refinement) with respect to the previous model. The Difference values listed decreased with an increasing number of elements, but did not converge within the span of the refinement demonstrated here, which indicates that the solutions to Model 1 contained a considerable amount of discretization error. However, since these values were in fact decreasing, this indicated that the mesh of Model 1 was at least approaching that of the ideal solution.

While a finer mesh than that of Model 1 would have resulted in more accurate solutions, increasing the number of elements was found to increase the solution time of the SOLID model considerably. The inclusion of non-linear effects, both geometric and material, was critical to demonstrate the valve phenomenon. Therefore, within given time constraints the

addition of non-linear effects was given priority over the use of a finer mesh, and in spite of the discretization error, Model 1 was found to demonstrate the valve phenomenon well and could also be validated against the experimental results of the physical model.

4.6 CONCLUSION

A paired thermal / structural finite element model was constructed to demonstrate the valve phenomenon provided by flow through a poroelastic solid with strain-dependent stiffness and permeability, and an underlying constriction hole. This FE model was validated against the experimental results of the physical model presented in Chapter 3. It proved to be an accurate model with respect to the absolute values of exudation and imbibition resistance as well as the ratio of exudation resistance to imbibition resistance at various applied pressures.

Previous studies of the diurnal load-flow behavior have demonstrated a clear need for a valve mechanism in the intervertebral disc in order to maintain healthy spine mechanics and disc hydration and nutrition. Current theories which describe the possible valve mechanisms in the disc do not account for the necessary magnitude of the direction-dependence of resistance to flow. There exist structures in the disc, i.e. those of the cartilage endplate and underlying holes in the bony endplate, which could provide the necessary valve phenomenon. The physical model and the finite element model have demonstrated how the combined effect of flow through the cartilage, as represented by a poroelastic solid, and through the underlying constriction holes in the bony endplate, could supply adequate direction-dependent effects.

Using the finite element model it was possible to demonstrate the effect of a reduction in the total number of underlying holes which is hypothesized to be one cause of back pain and other spinal disorders. As the cartilage endplate calcifies the holes in the bony endplate become covered and eventually the total number is reduced as shown with SEM in Chapter 2. The effect of this was investigated with the FE model and was found to result in a disruption of the normal daily disc height fluctuation amplitude and therefore the volume of fluid exchanged. Direction-dependent effects were also diminished. These changes could lead to various common disc pathologies such as disc degeneration due to a lack of bulk flow, nutrient exchange or disc dehydration due to the reduced valve effect.

While no *in vitro* or *in vivo* experiments have yet been performed to prove that this phenomenon exists in the body, the physical model and finite element model have clearly demonstrated the possibility for such a valve in the intervertebral disc. The aim of future studies will be to prove the existence of this valve *in vivo.* In addition, a comprehensive, three-dimensional finite element model of the *in vivo* situation will be constructed based on

the current validated model. This FE model will allow a demonstration of the effects of valve pathologies as well as those of possible surgical interventions.

Few finite element studies concerning the mechanical behavior of the spinal motion segment have incorporated fluid flow into the model. Those that have considered fluid flow have not addressed the issue of the necessary valve phenomenon nor have they investigated in any detail the structures which may provide this valve, although some have included osmotic swelling effects. Most studies have assumed the extension behavior of the flow in the disc to be simply the reverse of the behavior under compression. In many studies the permeability of the cartilage is assumed constant and/or the stress-strain curves of the disc tissues are assumed linear. Thus, a future FE study specifically focusing on flow into and out of the disc through the cartilage endplate and the resulting valve phenomenon will provide new insight into the behavior of the healthy, as well as the diseased intervertebral disc.

References

[1] Adams, M.A. and W.C. Hutton. The Effect of Posture on the Fluid Content of Lumbar Intervertebral Discs. *Spine,* **8**(6):p.665-71, 1983.

[2] ANSYS. ANSYS User's Manual. *Swanson Analysis Systems, Inc.* **1-4**(Revision 5.0) 1992.

[3] Bathe, K. Finite Element Procedures in Engineering Analysis. New Jersey, Prentice-Hall Inc. 1982,

[4] Belytschko, T., R.F. Kulak, A.B. Schultz, *et al.,* Finite Element Stress Analysis of an Intervertebral Disc. *J Biomech,* **7**:p.277-85, 1974.

[5] Gibson, L.J. and M.F. Ashby. Cellular Solids; Structure and Properties. New York, Pergamon Press, 1988,

[6] Goel, V.K., W. Kong, J.S. Han, *et al.,* A Combined Finite Element and Optimization Investigation of Lumbar Spine Mechanics With and Without Muscles. *Spine,* **18**(11):p.1531 1993.

[7] Hakim, N.S. and A.I. King. A Three Dimensional Finite Element Dynamic Response Analysis of a Vertebra with Experimental Verification. *J Biomech,* **12**:p.277-92, 1979.

[8] Kulak, R.F., T.B. Belytschko, A.B. Schultz, *et al.,* Nonlinear Behavior of the Human Intervertebral Disc Under Axial Load. *J Biomech,* **9**:p.377-86, 1976.

[9] Laible, J.P., D.S. Pflaster, M.H. Krag, *et al.,* A Poroelastic-Swelling Finite Element Model with Application to the Intervertebral Disc. *Spine,* **18**(5):p.659-70, 1993.

[10] Maroudas, A. Tissue Nutrition and Viability. In *Mechanisms of Fluid Transport in Cartilaginous Tissues.* Ch.3, A.R. Hargens, New York, Springer-Verlag, 1986, p.47-71.

[11] Matyjewski, M. A Poroelastic Model of the Intervertebral Disc. *15th Congress of Int Soc of Biomechanics,* :p.606-7, 1995.

[12] McNally, D.S. and M. Adams. Internal Intervertebral Disc Mechanics as Revealed by Stress Profilometry. *Spine,* **17**(1):p.66-73, 1992.

[13] Mizrahi, J., M.J. Silva, T.M. Keaveny, *et al.,* Finite-Element Stress Analaysis of the Normal and Osteoporotic Lumbar Vertebral Body. *Spine,* **18**(14):p.2088-96, 1993.

[14] Muskat, M. and R.D. Wyckoff. The Flow of Homogeneous Fluids Through Porous Media. In *Darcy's Law and the Measurement of the Permeability of Porous Media.* Ch.2, N/ANew York, Mc Graw-Hill Book Co. 1937, p.55-120.

[15] Nachemson, A. Lumbar Intradiscal Pressure; Experimental studies on post-mortem material. Copenhagen, Acta Orthop Scand Supplement, 1960,

[16] Nachemson, A. and G. Elfstroem. Intravital Dynamic Pressure Measurements in Lumbar Discs. Stockholm, The Almqvist and Wiksell Periodical Co. 1970, p.14.

[17] Shirazi-Adl, A. Finite-Element Simulation of Changes in the Fluid Content of Human Lumbar Disc; Mechanical and Clinical Implications. *Spine,* **17**(2):p.206-12, 1992.

[18] Shirazi-Adl, A. and M. Parnianpour. Nonlinear Response Analysis of the Human Ligamentous Lumbar Spine in Compression; On Mechanisms Affecting the Postural Stability. *Spine,* **18**(1):p.147-58, 1993.

[19] Simon, B.R. and M.A. Gaballa. Computer Methods in Bioengineering. In *Poroelastic Finite Element Models for the Spinal Motion Segment Including Ionic Swelling.* R.L. Spilker and B.R. Simon, New York, Publication of the ASME, 1988, p.93-9.

[20] Simon, B.R., J.S.S. Wu, M.W. Carlton, *et al.,* Structural Models for Human Spinal Motion Segments Based on a Poroelastic View of the Intervertebral Disc. *J Biomech Eng,* **107**:p.327-34, 1985.

[21] Simon, B.R., J.S.S. Wu, M.W. Carlton, *et al.,* Poroelastic Dynamic Structural Models of Rhesus Spinal Motion Segments. *Spine,* **10**(6):p.494-507, 1985.

[22] Spilker, R.L., D.M. Daugirda and A.B. Schultz. Mechanical Response of a Simple Finite Element Model of the Intervertebral Disc Under Complex Loading. *J Biomech,* **17**(2):p.103-12, 1984.

[23] Urban, J.P.G. Factors Influencing the Fluid Content of Intervertebral Discs. *Adv Microcirc,* **13**:p.160-70, 1987.

[24] Urban, J.P.G. and J.F. McMullin. Swelling Pressure of the Lumbar Intervertebral Discs: Influence of Age, Spinal Level, Composition and Degeneration. *Spine,* **13**(2):p.179-87, 1988.

CHAPTER
FIVE

CONCLUSION

5.1 REVIEW

Current literature concerning *in vivo* pressures in the intervertebral disc during daily loading indicate the necessary (and until now, unrecognized) existence of a valve mechanism (direction-dependent resistance) to control fluid flow into and out of the disc. Without such a mechanism, the disc would dehydrate or collapse. One theory proposes a physiological valve provided by the hydration-dependent permeability measured for the nucleus and annulus [9]. However, as discussed in Chapter 1, while the relationship between permeability and water content of the disc is non-linear [1], it does not provide the necessary direction-dependent effect.

It was therefore hypothesized that a mechanical valve may be provided by the interaction of flow through the cartilage endplates and holes in the underlying bony endplates. The presence of these "constriction" holes in the bony endplate was demonstrated in Chapter 2 in both sheep and human vertebrae. These holes have also been observed in many disc vascularity and nutrition studies since they provide seats for the vascular buds where the exchange of nutrients takes place [2,4-6,8]. The hypothesis is that as fluid flows out of the

disc under load the flow is constricted through these holes, the resulting velocity is high, and the fluid drag forces compress the matrix resulting in high resistance. As fluid flows back in during rest the cartilage matrix expands and the resistance is lower.

A physical model of flow through a poroelastic solid and one underlying constriction hole clearly demonstrated the direction-dependent resistance effect or "valve phenomenon". A finite element model of the physical model was constructed and validated against the experimental data. Once validated it was then used to demonstrate the effects of an increase or decrease in the number of underlying holes on the imbibition and exudation resistances as well as their ratio. This effect was of interest since calcification of the cartilage endplate and blockage of the holes is one possible valve pathology in the disc. If the cartilage endplate begins to mineralize the holes will be covered resulting in a decreased total number of holes. It is hypothesized that this would disrupt the normal daily fluid flow possibly resulting in disc degeneration or dehydration and abnormal stress on the solid structures of the disc.

5.2 CONCLUSION

The physical model demonstrated clearly the direction-dependent resistance provided by flow through a poroelastic solid and an underlying constriction hole. The results illustrated the efficiency that such a mechanical valve would provide *in vivo* in limiting the amount of fluid lost during loading, controlling the total fluid volume exchanged over the course of a day, providing a pressure-dependent resistance such that even under extreme loads the disc can maintain normal hydration, and most importantly allowing complete recovery of disc hydration during rest.

The finite element model results well validated by the experimental results of the physical model. This model will be modified in future to represent the *in vivo* situation and will allow investigation into the effects of a decrease or increase in the number of constriction holes *in vivo* as well as other possible valve pathologies, and the effects of surgical intervention. The FE model allowed a demonstration of the effects of a decrease in the size and a decrease in the total number of constriction holes in the physical model. Both a decrease in hole size and the total number of holes had the same effects: an increase in both the absolute exudation resistance and imbibition resistance, and a decrease in the ratio of the two. Similar effects can be expected in the *in vivo* model.

There exists a clear need for a valve mechanism in the intervertebral disc in order to maintain healthy disc hydration and mechanical function. While the presence of the proposed mechanical valve was not proven to exist in the body, the structures which could provide such a valve were suggested and have been studied to some extent in the literature. Future experiments will be performed in order to prove the existence of the valve mechanism in the disc, to study the structures which could provide this valve *in vivo,* to investigate the effects of valve pathologies and surgical intervention, and to determine a means of clinical diagnosis of such pathologies.

5.3 FUTURE WORK

5.3.1 SPINE PLUG FLUID FLOW TEST

In order to demonstrate the valve phenomenon in the intervertebral disc an *in vitro* experiment will be designed to determine the resistance ratio in both sheep and human disc plugs cut from spine segments. These plugs will be cut from the center of the disc and will consist of a thin layer of the vertebral bone, the cartilage endplate and some amount of nuclear tissue. Fluid will be pumped through these plugs in both directions (from bone to tissue and tissue to bone) in a sealed glass column at a set flow rate and the pressure will be measured. The pressure can then be compared for the two flow directions at the same flow rate and the direction-dependent resistance can be demonstrated.

5.3.2 FLOW PATH STAINING

Much speculation continues over the dominant flow path in the intervertebral disc. The valve hypothesis assumes that this flow path is predominantly through the cartilage endplates and into the vertebral bodies. An *in vitro* experiment will be designed to stain the path of flow in the intervertebral disc during creep loading cycles. Spinal segments will be allowed to swell in a fluorescent stain solution and will be subsequently loaded in creep. Various numbers of swelling-creep loading cycles will be applied to the segments. When the loading cycle is complete the segment will be cryofixed, freeze substituted, embedded, sliced and analyzed using light microscopy.

Initial experiments will be performed as described in Section 5.3.1 to actively pump fluorescent stain through the disc plugs. This will allow some preliminary investigation of the fluid flow through the bony endplate holes under an applied pressure.

5.2.3 LONG TERM CREEP TESTS

Many studies have focused on *in vitro* creep loading of spine segments. However, few have performed long-term creep tests to demonstrate the behavior of the segment over a daily loading period. The intradiscal pressure changes during such long term creep tests would give an indication of the role which fluid flow and disc fluid content play during daily loading. That is, if the pressure is found to drop over the course of a day's loading, the load would then be transferred to the solid structures of the disc. Otherwise, the fluid would support the entire load.

A valve pathology such as hole blockage would disrupt the normal daily fluid flow in the disc and would result in abnormal loading of the solid structures of the disc. Thus, *in vitro* creep experiments with intradiscal pressure measurement will be performed on both sheep and human spine segments in order to correlate creep response and valve pathologies. After performing a creep test the bony endplate of the vertebrae will be studied using scanning electron microscopy in order to determine the number, size and distribution of constriction holes. The cartilage endplate will also be examined for any signs of degeneration or dehydration. The same experiment will be performed after both blocking the endplate route and opening up more holes in the endplate in order to demonstrate the effects of hole blockage as well as an excessive number of holes and the effects of surgical intervention (opening up new holes).

5.3.4 MAGNETIC RESONANCE IMAGING

In order to consider a clinical treatment for valve pathologies some method of diagnosis should be defined. If the holes in the bony endplate were to close there would be a disruption of the normal daily fluid flow in the disc. Thus, by monitoring the disc fluid content of a patient with back pain over the course of a day (measure water content at various intervals throughout the day) it should be possible to determine whether or not the flow path has been disrupted. Hickey *et al.* [3] have measured relative degrees of disc hydration in living subjects and experimental specimens using magnetic resonance imaging, and Panagiatacopoulos *et al.* [7] have investigated the relationship between disc water content and the mechanical properties of the disc using nuclear magnetic resonance imaging (NMR) to measure the cross-sectional water distribution.

NMR should also allow the measurement of disc fluid content *in vitro* in spinal motion segments subjected to various loads and of varying degrees of disc degeneration. Such an

experiment would provide vital information about the dependence of fluid content and fluid flow behavior under load on the number and distribution of constriction holes in the bony endplate. Furthermore sequential images of the disc of a spinal motion segment subjected to compressive loading could be taken in order to trace the flow path or simply to determine the final location of the fluid in the disc and thus indirectly determine the path of flow.

5.3.5 FINITE ELEMENT MODEL

The finite element model presented in Chapter 4 will be modified to represent the *in vivo* situation. Material properties of the disc tissues measured experimentally or obtained from the literature will be incorporated including non-linear stress-strain and permeability-strain curves. An initial model of the endplate and underlying cortical bone alone will first be constructed and tested. This model can then be further modified to represent the entire spinal motion segment. Variations in the size and number of constriction holes will be studied to model the effects of hole blockage and surgical intervention.

5.3.6 *IN VIVO* DIURNAL PRESSURE FLUCTUATION MEASUREMENT

An alternate or additional means of valve pathology diagnosis could be obtained by monitoring the diurnal fluctuations in intradiscal pressure in patients complaining of back pain. If the endplate holes closed up, it would be impossible for the fluid to escape from the disc. Thus, the pressure drop which occurs as fluid escapes and the load is transferred to the solid structures would not be observed. Instead, the pressure would remain approximately constant (under the same load) at a maximum value throughout the course of the day. An experiment will be designed to monitor the change in intradiscal pressure *in vivo* in both healthy subjects and patients with back pain. Pressure will be measured at set times during the day under the same load (patient standing or sitting, with or without weights).

References

[1] Adams, M.A. and W.C. Hutton. The Effect of Posture on the Fluid Content of Lumbar Intervertebral Discs. *Spine,* **8**(6):p.665-71, 1983.

[2] Crock, H.V. and M. Goldwasser. Anatomic Studies of the Circulation in the Region of the Vertebral End-Plate in Adult Greyhound Dogs. *Spine,* **9**(7):p.702-6, 1984.

[3] Hickey, D.S., R.M. Aspden, D.W.L. Hukins, *et al.,* Analysis of Magnetic Resonance Images from Normal and Degenerate Lumbar Intervertebral Discs. *Spine,* **11**(7):p.702-8, 1986.

[4] Holm, S., A. Maroudas, J.P.G. Urban, *et al.,* Nutrition of the Intervertebral Disc: Solute Transport and Metabolism. *Conn Tiss Res,* **8**:p.101-19, 1981.

[5] Maroudas, A., R. Stockwell, A. Nachemson, *et al.,* Factors involved in the nutrition of the human lumbar intervertebral disc: cellularity and diffusion of glucose *in vitro. J. Anat.,* **120**(1):p.113-30, 1975.

[6] Oki, S., Y. Matsuda, T. Itoh, *et al.,* Scanning Electron Microscopic Observations of the Vascular Structure of Vertebral End-Plates in Rabbits. *J Orthop Res,* **12**:p.447-9, 1994.

[7] Panagiotacopulos, N.D., M.H. Pope, M.H. Krag, *et al.,* Water Content in Human Intervertebral Discs: Part I. Measurement by NMR Imaging. *submitted to Spine,* 1984.

[8] Urban, J.P.G., S. Holm, A. Maroudas, *et al.,* Nutrition of the Intervertebral Disc, An *In Vivo* Study of Solute Transport. *Clin Orthop and Rel Res,* **129**:p.101-14, 1977.

[9] Urban, J.P.G. and J.F. McMullin. Swelling Pressure of the Lumbar Intervertebral Discs: Influence of Age, Spinal Level, Composition and Degeneration. *Spine,* **13**(2):p.179-87, 1988.

APPENDIX

A.1 DATA CHARTS

Table A.1. 1 Physical model raw data; three subsequent measurements of time for 77 mL of glycerin to flow in or out at each applied pressure.

Pressure	Time for 77mL (s), Flow **IN**			Time for 77mL (s), Flow **OUT**		
(bar)	1	2	3	1	2	3
0.03160	389.1	444.8	521.9	431.5	405.0	521.0
0.04160	396.4	334.9	---	411.3	342.6	---
0.05160	277.6	308.8	261.4	326.8	324.3	281.5
0.06160	251.1	228.0	---	259.0	277.6	---
0.07160	219.8	204.6	178.6	241.6	222.9	208.0
0.08160	193.4	179.2	---	220.9	207.4	---
0.09160	173.9	155.4	146.9	186.3	183.7	170.1
0.14160	101.8	94.0	88.3	126.0	121.5	112.7
0.19160	70.7	65.4	63.4	93.4	90.8	87.0
0.24160	53.6	48.6	47.1	76.0	76.1	70.8
0.29160	41.6	44.3	40.8	64.8	69.0	65.0
0.34160	34.1	35.6	34.3	4.9	5.2	5.1
0.34160	28.7	27.9	30.2	52.7	51.5	51.2

Pressure	Time for 77mL (s), Flow **IN**			Time for 77mL (s), Flow **OUT**		
(bar)	1	2	3	1	2	3
0.39160	25.2	24.3	26.3	47.4	48.8	47.9
0.44160	20.1	19.0	20.4	41.4	41.8	41.6
0.54160	17.8	17.7	18.0	35.7	38.1	37.7
0.64160	15.6	15.2	15.5	36.2	34.4	35.7
0.74160	12.6	13.7	13.3	31.1	31.3	31.8
0.84160	11.4	12.1	12.1	29.0	29.9	30.3
0.94160	10.5	10.9	11.1	27.7	27.8	29.3
1.0416	9.3	9.9	9.9	26.9	27.8	29.1
1.1416	8.8	8.9	9.3	25.2	25.8	27.5
1.2416	7.8	8.2	8.3	24.6	25.7	25.8
1.3416	7.1	7.6	7.7	23.8	24.9	25.0
1.4416	6.7	7.1	7.0	23.1	24.2	25.0
1.5416	6.3	6.8	6.6	22.3	24.2	24.3
1.6416	6.0	6.2	6.1	23.0	23.6	23.4
1.7416	5.8	5.6	5.7	22.4	22.7	23.0
1.8416	5.3	5.3	5.3	22.3	21.9	23.3
1.9416	4.9	5.2	5.1	21.5	21.5	22.0
2.0416	4.6	5.0	4.9	21.1	21.4	22.1
2.1416	4.3	4.7	4.6	21.0	21.3	21.3
2.2416	4.2	4.5	4.4	20.5	21.0	21.3
2.3416	3.9	4.1	4.1	19.4	20.5	20.9
2.4416	3.7	4.1	3.8	19.9	20.5	20.4

Table A.1.2 Finite element model results and corresponding experimental results of the physical model constriction flow test (mean value at each applied pressure).

Pressure	Data From	Flow Rate (E06 m^3/s)		Resistance (P/Q) (E-09 $N.s/m^5$)	
(Pa)		OUT	IN	OUT	IN
3160	Physical Model Mean	0.172	0.173	0.184	0.183
	Finite Element Model	0.147	0.148	0.215	0.214
4160	Physical Model Mean	0.208	0.210	0.200	0.198
	Finite Element Model	0.193	0.195	0.216	0.213
5160		0.260	0.263	0.198	0.196
		0.234	0.241	0.216	0.214
6160		0.287	0.322	0.215	0.191
		0.285	0.287	0.216	0.215
7160		0.331	0.331	0.208	0.185
		0.345	0.386	0.216	0.216
8160		0.360	0.414	0.227	0.197
		0.374	0.375	0.218	0.218
9160		0.428	0.487	0.214	0.188
		0.417	0.419	0.220	0.219
14160		0.643	0.816	0.220	0.174
		0.606	0.656	0.234	0.216
19160		0.852	1.16	0.225	0.165
		0.774	0.927	0.247	0.207
24160		1.04	1.55	0.232	0.156
		0.925	1.24	0.261	0.195

Pressure	Data From	Flow Rate (E06 m^3/s)		Resistance (P/Q) (E-09 $N.s/m^5$)	
(Pa)		OUT	IN	OUT	IN
29160		1.16	1.83	0.251	0.159
		1.06	1.54	0.275	0.189
34160		1.34	2.22	0.255	0.154
		1.19	1.94	0.287	0.176
39160		1.49	2.66	0.263	0.147
		1.31	2.34	0.299	0.167
44160		1.60	3.05	0.276	0.145
		1.42	2.76	0.311	0.160
54160		1.85	3.88	0.293	0.140
		1.63	3.60	0.332	0.150
64160		2.07	4.32	0.310	0.149
		1.85	3.07	0.347	0.147
74160		2.18	4.99	0.340	0.149
		2.07	5.10	0.358	0.145
84160		2.45	5.84	0.344	0.144
		2.28	5.83	0.369	0.144

A.2 COMPUTER PROGRAMS AND ANSYS MACROS

A.2.1 STRAIN TO PERMEABILITY CONVERSION PROGRAM (STRN2PERM.C)

```
/*

This program takes values of element axial strain from output files generated in an ANSYS
structural model and converts them to element permeabilities (K)according to an
experimentally determined K vs. strain curve.

These permeabilities are then output to a command file (strn2per.mac) to be applied to a
corresponding thermal flow model.  This program was in part a modification of a program
written by Keita Ito which converts volumetric strain to heat source values.

written by: Dana Ayotte, 20.10.95

*/

#include <stdio.h>

#include <string.h>

#include <math.h>


#define NLONG   20

#define NSHORT 10

#define ELNUM   272

#define NNUM    301

#define STRING   20

#define VISC     0.7

#define PI       3.14159

#define DENS     1263.0


/* function to calculate element permeability from element strains */

float perm(double Ev)

{
```

```
 float abs_K;
 abs_K = (1.53 * exp(Ev-1.40) + 1.51 - 1.62 * exp(.0218 * Ev)) * 1.0E-11;
 return abs_K;
}

double exp(double);

main()
{
 float K[ELNUM] = {0};
 float el_nod_num[ELNUM][4];

 char   ystrn_string[NLONG] = " ";

 float el_xperm, el_yperm;

 double ystrn;
 double perm_sum, avg_K;

 int      i, el_num, mat_num;

 FILE *ystrn_infile, *fopen();
 FILE *macro_outfile, *fopen();
 FILE *perm_outfile, *fopen();

/* open input/output files */
if((macro_outfile = fopen("/public/people/dana/ansys/strn2per.mac", "w")) == NULL)
```

```
   printf("vel2drg.mac could not be opened.\n");
if((perm_outfile = fopen("/public/people/dana/ansys/perm.dat", "w")) == NULL)
   printf("perm.dat could not be opened.\n");
if((ystrn_infile = fopen("/public/people/dana/ansys/ystrn.dat", "r")) == NULL)
   printf("ystrn.dat could not be opened.\n");

/*************************************************************** **/
/*  Calculate element permeability using the experimentally determined   */
/*  permeability vs. strain curve and axial strain (function: perm)      */
/*  and fill permeability array with isotropic K                         */
/*************************************************************** **/
 for(i=0;i<ELNUM;++i){

   /* read in TRUE y strain string */
   fgets(ystrn_string, STRING, ystrn_infile);

   /* assign to variables */
   sscanf(ystrn_string, "%lf", &ystrn);

   /* calculate x, y and z direction K with true ystrain only */
    K[i] = perm(ystrn);
 }

/*************************************************************/
/*  Create ANSYS command file.                                   */
/*  --> mp and emodif commands are used to apply absolute x and y  */
```

```
/*        permeabilities to each element.                                    */
/*************************************************************************/

 perm_sum = 0;

 for(i=0; i<ELNUM; ++i){

  el_num = (i+1);

  mat_num = el_num;

  el_xperm = K[i];

  el_yperm = K[i];

  fprintf(macro_outfile, "mp,kxx,%i,%.4e\n", mat_num, el_xperm);

  fprintf(macro_outfile, "mp,kyy,%i,%.4e\n", mat_num, el_yperm);

  fprintf(macro_outfile, "mp,visc,%i,%3.2f\n", mat_num, VISC);

  fprintf(macro_outfile, "mp,dens,%i,%5.0f\n", mat_num, DENS);

  fprintf(macro_outfile, "emodif,%i,mat,%i\n", el_num, mat_num);

  fprintf(perm_outfile, "%.4e  %.4e\n", el_xperm, el_yperm);

  perm_sum += K[i];

  }


 avg_K = perm_sum / ELNUM;

 printf(">> average permeability = %.8e\n", avg_K);


 fclose(ystrn_infile);

 fclose(macro_outfile);

 fclose(perm_outfile);


}
```

A.2.2 SAMPLE OF STRN2PERM.MAC ANSYS MACRO (CREATED BY STRN2PERM.C)

```
mp,kxx,1,1.8451e-12
mp,kyy,1,1.8451e-12
mp,visc,1,0.70
mp,dens,1, 1263
emodif,1,mat,1
mp,kxx,2,1.9187e-12
mp,kyy,2,1.9187e-12
mp,visc,2,0.70
mp,dens,2, 1263
emodif,2,mat,2
mp,kxx,3,1.9920e-12
mp,kyy,3,1.9920e-12
mp,visc,3,0.70
mp,dens,3, 1263
emodif,3,mat,3
mp,kxx,4,3.3284e-12
mp,kyy,4,3.3284e-12
mp,visc,4,0.70
mp,dens,4, 1263
emodif,4,mat,4
```

A.2.3 VELOCITY TO DRAG FORCES CONVERSION PROGRAM (VEL2DRG.C)

```
/*

This program takes values of element velocity from output files generated in an ANSYS
thermal flow model and converts them to nodal drag forces.

These drag forces are then output to a command file vel2drg.mac to be applied to a
corresponding structural model.  This program was in part a modification of a program
written by Keita Ito which converts volumetric strain to heat source values.

written by: Dana Ayotte, 20.10.95

*/

#include <stdio.h>

#include <string.h>

#include <math.h>


#define NLONG      40

#define NSHORT     12

#define ELNUM      272

#define NNUM       301

#define STRING     16

#define VISC       0.7

#define DENS       1263.0

#define PI         3.14159

#define PERM       2.67e-12      /* permeability at zero strain */


main()

{

 float  el_vel[ELNUM][2] = {0};

 float  el_nod_num[ELNUM][4] = {0};
```

```
float el_perm[ELNUM] = {0};
float  nod_drg[NNUM][2] = {0};

char  xvel_string[NLONG] = " ";
char  yvel_string[NLONG] = " ";
char  n1_string[NSHORT] = " ";
char n2_string[NSHORT] = " ";
char  n3_string[NSHORT] = " ";
char n4_string[NSHORT] = " ";
char  vol_data[NLONG] = " ";
char lastQ_string[NLONG] = " ";
char perm_string[60] = " ";

float  el_vol, el_drg_x, el_drg_y, R;
float  xvel, yvel, xdrg, ydrg, xdrgsum, ydrgsum;
float  n1, n2, n3, n4;
float lastQ, deltaQ, K;
float Q_hole;

int    i, j, m, node_num, row, r;
int    init_el, el_row;

FILE *vol_infile, *fopen();
FILE *xvel_infile, *fopen();
FILE *yvel_infile, *fopen();
FILE *nd1_infile, *fopen();
FILE *nd2_infile, *fopen();
```

```
FILE *nd3_infile, *fopen();
FILE *nd4_infile, *fopen();
FILE *Q_infile, *fopen();
FILE *perm_infile, *fopen();
FILE *Q_outfile, *fopen();
FILE *out_file, *fopen();

/* open input/output files */
if((out_file = fopen("/public/people/dana/ansys/vel2drg.mac", "w")) == NULL)
  printf("vel2drg.mac could not be opened.\n");
if((Q_outfile = fopen("/public/people/dana/ansys/Qout.dat", "a")) == NULL)
  printf("Qout.dat could not be opened.\n");
if((perm_infile = fopen("/public/people/dana/ansys/perm.dat", "r")) == NULL)
  printf("perm.dat could not be opened.\n");
if((vol_infile = fopen("/public/people/dana/ansys/vol.dat", "r")) == NULL)
  printf("vol.dat could not be opened.\n");
if((xvel_infile = fopen("/public/people/dana/ansys/xvel.dat", "r")) == NULL)
  printf("xvel.dat could not be opened.\n");
if((yvel_infile = fopen("/public/people/dana/ansys/yvel.dat", "r")) == NULL)
  printf("yvel.dat could not be opened.\n");
if((nd1_infile = fopen("/public/people/dana/ansys/el_nd1.dat", "r")) == NULL)
  printf("el_nd1.dat could not be opened.\n");
if((nd2_infile = fopen("/public/people/dana/ansys/el_nd2.dat", "r")) == NULL)
  printf("el_nd2.dat could not be opened.\n");
if((nd3_infile = fopen("/public/people/dana/ansys/el_nd3.dat", "r")) == NULL)
  printf("el_nd3.dat could not be opened.\n");
if((nd4_infile = fopen("/public/people/dana/ansys/el_nd4.dat", "r")) == NULL)
```

```
  printf("el_nd4.dat could not be opened.\n");
 if((Q_infile = fopen("/public/people/dana/ansys/Qin.dat", "r")) == NULL)
  printf("Qin.dat could not be opened.\n");

/* FILL element velocity array */
 for(i=0;i<ELNUM;++i){
  fgets(xvel_string, STRING, xvel_infile);
  fgets(yvel_string, STRING, yvel_infile);
  sscanf(xvel_string, "%f", &xvel);
  sscanf(yvel_string, "%f", &yvel);
  el_vel[i][0] = xvel;
  el_vel[i][1] = yvel;
 }

/* FILL element node numbers array */
 for(i=0;i<ELNUM;++i){
  fgets(n1_string, NSHORT, nd1_infile);
  fgets(n2_string, NSHORT, nd2_infile);
  fgets(n3_string, NSHORT, nd3_infile);
  fgets(n4_string, NSHORT, nd4_infile);
  sscanf(n1_string, "%f", &n1);
  sscanf(n2_string, "%f", &n2);
  sscanf(n3_string, "%f", &n3);
  sscanf(n4_string, "%f", &n4);
  el_nod_num[i][0] = n1;
  el_nod_num[i][1] = n2;
  el_nod_num[i][2] = n3;
```

```
  el_nod_num[i][3] = n4;
 }

/* FILL element permeability array */
 for(i=0;i<ELNUM;++i){
  fgets(perm_string, NLONG, perm_infile);
  sscanf(perm_string, "%e %e", &K, &K);   /* Kx and Ky are the same */
  el_perm[i] = K;
 }

/*************************************************************************/
/*  Calculate the volume flow rate through the hole for various models   */
/*************************************************************************/

/* for PORO0 no hole model - flow through bottom */
/*
 Q_hole = 0;
 R = 0.001;
 init_el = 1;
 el_row = init_el - 1;
 for(r=1;r<9;++r){
  Q_hole += (el_vel[el_row][1]) * PI * ( ((r*R) * (r*R)) - (((r-1)*R) * ((r-1)*R)) );
  ++el_row;
 }
 Q_hole += (el_vel[88][1]) * PI * (.000036);
 Q_hole += (el_vel[99][1]) * PI * (.000044);
 Q_hole += (el_vel[112][1]) * PI * (.000052);
```

```
 Q_hole += (el_vel[127][1]) * PI * (.00006);
 Q_hole += (el_vel[152][1]) * PI * (.000144);
 Q_hole += (el_vel[163][1]) * PI * (.000176);
 Q_hole += (el_vel[176][1]) * PI * (.000208);
 Q_hole += (el_vel[191][1]) * PI * (.00024);
 Q_hole += (el_vel[216][1]) * PI * (.000576);
 Q_hole += (el_vel[227][1]) * PI * (.000704);
 Q_hole += (el_vel[240][1]) * PI * (.000832);
 Q_hole += (el_vel[255][1]) * PI * (.00096);
*/
```

/* (els 1-2) for PORO8 2-element hole model*/

```
/*
 Q_hole = 0;
 R = 0.001;
 init_el = 1;
 el_row = init_el - 1;
 for(r=1;r<3;++r){
  Q_hole += (el_vel[el_row][1]) * PI * ( ((r*R) * (r*R)) - (((r-1)*R) * ((r-1)*R)) );
  ++el_row;
 }
*/
```

/* (els 1-4) for PORO8 model */

```
 Q_hole = 0;
 R = 0.001;
 init_el = 1;
```

```
 el_row = init_el - 1;
 for(r=1;r<5;++r){
  Q_hole += (el_vel[el_row][1]) * PI * ( ((r*R) * (r*R)) - (((r-1)*R) * ((r-1)*R)) );
  ++el_row;
 }
```

/* (els 1-1) for PORO8 model */

```
/*
 Q_hole = 0;
 R = 0.001;
 init_el = 1;
 el_row = init_el - 1;
 for(r=1;r<2;++r){
  Q_hole += (el_vel[el_row][1]) * PI * ( ((r*R) * (r*R)) - (((r-1)*R) * ((r-1)*R)) );
  ++el_row;
 }
*/
```

/* (els 160-167) for PORO9 model */

```
/*
 Q_hole = 0;
 R = 0.0005;
 init_el = 160;
 el_row = init_el - 1;
 for(r=1;r<9;++r){
  Q_hole += (el_vel[el_row][1]) * PI * ( ((r*R) * (r*R)) - (((r-1)*R) * ((r-1)*R)) );
  ++el_row;
```

```
 }
*/

/* (els 144-151) for PORO10 model */
/*
 Q_hole = 0;
 R = 0.0005;
 init_el = 144;
 el_row = init_el - 1;
 for(r=1;r<9;++r){
  Q_hole += (el_vel[el_row][1]) * PI * ( ((r*R) * (r*R)) - (((r-1)*R) * ((r-1)*R)) );
  ++el_row;
 }
*/

/* (els 236-251) for PORO11 model */
/*
 Q_hole = 0;
 R = 0.00025;
 init_el = 236;
 el_row = init_el - 1;
 for(r=1;r<17;++r){
  Q_hole += (el_vel[el_row][1]) * PI * ( ((r*R) * (r*R)) - (((r-1)*R) * ((r-1)*R)) );
  ++el_row;
 }
*/
```

```
/* (els 236 - 239) for PORO11 variable hole size model */
/*
  Q_hole = 0;
  R = 0.00025;
  init_el = 236;
  el_row = init_el - 1;
  for(r=1;r<5;++r){
    Q_hole += (el_vel[el_row][1]) * PI * ( ((r*R) * (r*R)) - (((r-1)*R) * ((r-1)*R)) );
    ++el_row;
  }
*/

/*********************************************************************/
/*  -calculate difference between last Q and current Q (measure of convergence)  */
/* -read last Q from Qin and store all Q's in Qout                    */
/*********************************************************************/
  fprintf(Q_outfile, "%.4e\n", Q_hole);
  fgets(lastQ_string, STRING, Q_infile);
  Q_outfile = fopen("/public/people/dana/ansys/Qin.dat", "w");
  fprintf(Q_outfile, "%.4e\n", Q_hole);
  sscanf(lastQ_string, "%e", &lastQ);
  deltaQ = (lastQ - Q_hole);
  printf("current Q through hole = %.4e\n", Q_hole);
  printf("previous Q = %.4e\n", lastQ);
  printf("difference = %.4e\n\n", deltaQ);

/*********************************************************************/
```

```
/* Calculate element drag forces and resulting average nodal drag forces */
/*********************************************************************/
 for(i=0;i<ELNUM;++i){
  fgets(vol_data, NLONG, vol_infile);
  sscanf(vol_data, "%f", &el_vol);

  /* >>>>>> FOR FIRST RUN WITH CONSTANT PERMEABILITY <<<<<< */
/*
  el_drg_x = el_vel[i][0] * (1 / PERM) * VISC * el_vol * (1 / DENS);
  el_drg_y = el_vel[i][1] * (1 / PERM) * VISC * el_vol * (1 / DENS);
*/
  /* >>>>>>>>>>>>>>>> FOR ALL SUBSEQUENT RUNS <<<<<<<<<<<<<<<< */
  el_drg_x = el_vel[i][0] * (1 / el_perm[i]) * VISC * el_vol * (1 / DENS);
  el_drg_y = el_vel[i][1] * (1 / el_perm[i]) * VISC * el_vol * (1 / DENS);

/*********************************************************************/
/* Fill the nodal drag arrays (x and y) with the average drag force at each node, */
/* calculated from the average of the surrounding elements */
/*********************************************************************/
for(j=0;j<4;++j){
    row = (el_nod_num[i][j]);          /* There will be nothing in the */
    nod_drg[row][0] += (el_drg_x / 4);  /* first row of nod_drg array. */
    nod_drg[row][1] += (el_drg_y / 4);
   }
  }

/* create ANSYS command file to apply the nodal drag forces */
```

```
xdrgsum = 0;
ydrgsum = 0;
for(i=1; i<(NNUM+1); ++i){
  node_num = i;
  xdrg = (nod_drg[i][0]);
  ydrg = (nod_drg[i][1]);
  xdrgsum += xdrg;
  ydrgsum += ydrg;
  fprintf(out_file, "f,%i,FX,%.4e\n", node_num, xdrg);
  fprintf(out_file, "f,%i,FY,%.4e\n", node_num, ydrg);
}

printf(">>> TOTAL X DRAG = %.4e\n", xdrgsum);
printf(">>> TOTAL Y DRAG = %.4e\n", ydrgsum);

fclose(vol_infile);
fclose(xvel_infile);
fclose(yvel_infile);
fclose(nd1_infile);
fclose(nd2_infile);
fclose(nd3_infile);
fclose(nd4_infile);
fclose(perm_infile);
fclose(Q_infile);
fclose(Q_outfile);
fclose(out_file);
```

}

A.2.4 SAMPLE OF VEL2DRG.MAC ANSYS MACRO FILE (CREATED BY VEL2DRG.C)

f,1,FX,1.6986e-04

f,1,FY,5.4057e-03

f,2,FX,1.5958e-03

f,2,FY,2.3559e-02

f,3,FX,4.0763e-03

f,3,FY,5.3435e-02

f,4,FX,9.4108e-03

f,4,FY,9.5196e-02

f,5,FX,6.6732e-02

f,5,FY,1.0547e-01

f,6,FX,9.4498e-02

f,6,FY,5.0640e-02

f,7,FX,6.1374e-02

f,7,FY,8.1422e-03

f,8,FX,4.9876e-02

f,8,FY,4.4114e-03

f,9,FX,5.2651e-02

f,9,FY,4.0439e-03

f,10,FX,5.6769e-04

f,10,FY,9.9314e-03

f,11,FX,4.2130e-03

f,11,FY,4.1203e-02

A.2.5 ANSYS MACROS TO FILL DATA ARRAYS

A.2.5.1 Element Nodal Data

```
*dim,el_nd1,array,1529,1
*cfopen,el_nd1,dat
*vget,el_nd1(1),elem,1,node,1
*vwrite,el_nd1(1)
(3f10.0)
*cfclos

*dim,el_nd2,array,1529,1
*cfopen,el_nd2,dat
*vget,el_nd2(1),elem,1,node,2
*vwrite,el_nd2(1)
(3f10.0)
*cfclos

*dim,el_nd3,array,1529,1
*cfopen,el_nd3,dat
*vget,el_nd3(1),elem,1,node,3
*vwrite,el_nd3(1)
(3f10.0)
*cfclos

*dim,el_nd4,array,1529,1
*cfopen,el_nd4,dat
*vget,el_nd4(1),elem,1,node,4
```

*vwrite,el_nd4(1)

(3f10.0)

*cfclos

A.2.5.2 Element Strain Data

*dim,x_strn,array,1529,1

*cfopen,xstrn,dat

*vget,x_strn(1),elem,1,etab,EPTOX

*vwrite,x_strn(1)

(E10.3)

*cfclos

*dim,y_strn,array,1529,1

*cfopen,ystrn,dat

*vget,y_strn(1),elem,1,etab,EPTOY

*vwrite,y_strn(1)

(E10.3)

*cfclos

*dim,z_strn,array,1529,1

*cfopen,zstrn,dat

*vget,z_strn(1),elem,1,etab,EPTOZ

*vwrite,z_strn(1)

(E10.3)

*cfclos

A.2.5.3 Element Velocity Data

```
*dim,el_vel_x,array,1529,1
*cfopen,xvel,dat
*vget,el_vel_x(1),elem,1,etab,TFX
*vwrite,el_vel_x(1)
(E13.5)
*cfclos

*dim,el_vel_y,array,1529,1
*cfopen,yvel,dat
*vget,el_vel_y(1),elem,1,etab,TFY
*vwrite,el_vel_y(1)
(E13.5)
*cfclos
```

A.2.5.4 Element Volume Data

```
*cfopen,vol,dat
*dim,el_vol,array,1529,1
*vget,el_vol(1),elem,1,etab,VOLU
*vwrite,el_vol(1)
(E10.3)
*cfclos
```